

Census of Ly α Emission from ~ 600 Galaxies at $z = 5 - 14$: Evolution of the Ly α Luminosity Function and a Late Sharp Cosmic Reionization

YUTA KAGEURA ^{1,2} MASAMI OUCHI ^{3,1,4,5} MINAMI NAKANE ^{1,2} HIROYA UMEDA ^{1,2} YUICHI HARIKANE ¹,
SHINTARO YOSHIURA ³ KIMHIKO NAKAJIMA ³ HIDENOBU YAJIMA ⁶ AND TRAN THI THAI ³

¹*Institute for Cosmic Ray Research, The University of Tokyo, 5-1-5 Kashiwanoha, Kashiwa, Chiba 277-8582, Japan*

²*Department of Physics, Graduate School of Science, The University of Tokyo, 7-3-1 Hongo, Bunkyo, Tokyo 113-0033, Japan*

³*National Astronomical Observatory of Japan, 2-21-1 Osawa, Mitaka, Tokyo 181-8588, Japan*

⁴*Department of Astronomical Science, SOKENDAI (The Graduate University for Advanced Studies), Osawa 2-21-1, Mitaka, Tokyo, 181-8588, Japan*

⁵*Kavli Institute for the Physics and Mathematics of the Universe (WPI), University of Tokyo, Kashiwa, Chiba 277-8583, Japan*

⁶*Center for Computational Sciences, University of Tsukuba, Ten-nodai, 1-1-1 Tsukuba, Ibaraki 305-8577, Japan*

ABSTRACT

We present the statistical properties of Ly α emission in 586 galaxies at $z = 4.5 - 14.2$, observed by multiple JWST/NIRSpec spectroscopy projects, including JADES, GLASS, CEERS, and GO/DDT programs. We obtain Ly α equivalent width (EW), Ly α escape fraction, and ionizing photon production efficiency measurements or upper limits for these galaxies, and confirm that the Ly α emitting galaxy fraction decreases towards higher redshifts. We derive Ly α luminosity functions from $z \sim 5$ to $z \sim 10 - 14$ with the observed Ly α EW distributions and galaxy UV luminosity functions, and find a ~ 3 dex decrease in number density at $L_{\text{Ly}\alpha} = 10^{42} - 10^{43} \text{ erg s}^{-1}$ over the redshift range. We obtain the neutral hydrogen fractions of $x_{\text{H I}} = 0.17^{+0.23}_{-0.16}$, $0.63^{+0.18}_{-0.28}$, $0.79^{+0.13}_{-0.21}$, and $0.88^{+0.11}_{-0.13}$ at $z \sim 6, 7, 8 - 9$, and $10 - 14$, respectively, via comparisons of the reionization models developed by semi-numerical simulations with 21cmFAST explaining the observations of Ly α , UV continuum, and Planck electron optical depth. The high $x_{\text{H I}}$ values over $z \sim 7 - 14$ suggest a late and sharp reionization, with the primary reionization process occurring at $z \sim 6 - 7$. Such a late and sharp reionization is not easily explained by either a clumpy inter-galactic medium or sources of reionization in a classical faint-galaxy or a bright-galaxy/AGN scenario, unless a very high escape fraction or AGN duty cycle is assumed at $z \sim 6 - 7$.

Keywords: Galaxy evolution (594), High-redshift galaxies (734), Lyman-alpha galaxies (978), Reionization (1383)

1. INTRODUCTION

Cosmic reionization marks the last major phase transition in cosmic history. During the Epoch of Reionization (EoR), neutral hydrogen in the intergalactic medium (IGM), formed at Recombination, was ionized by ultraviolet (UV) photons emitted by the first sources. However, the exact progression of reionization with redshift (i.e., the reionization history) remains debated. Understanding this history is crucial, as it provides insights into the primary sources driving reionization.

To investigate the reionization history, the redshift evolution of the neutral hydrogen fraction $x_{\text{H I}}$ has been estimated through various methods. Gunn-Peterson troughs of quasar spectra (Gunn & Peterson 1965) have shown that reionization is largely completed (i.e., $x_{\text{H I}} \sim 0$) by $z \sim 6$ (e.g., Becker et al. 2001; Fan et al. 2006). Recent advanced analyses of Ly α forests and Ly $\alpha + \beta$ dark fraction or gaps, and state-of-the-art simulations have suggested that neutral hydrogen persists as late as $z \sim 5.3$ (e.g., Kulkarni et al. 2019; Bosman et al. 2022; Spina et al. 2024; Zhu et al. 2024). At $z \sim 6 - 7$, $x_{\text{H I}}$ has been investigated using various techniques, including Ly α damping wing absorption measurements in gamma-ray burst (GRB) and quasar (QSO) spectra

(e.g., Totani et al. 2006, 2014; Wang et al. 2020; Yang et al. 2020; Āurovčřková et al. 2024; Fausey et al. 2024), Ly α equivalent width (EW) distributions (e.g., Mason et al. 2018; Hoag et al. 2019; Bolan et al. 2022), Ly α luminosity functions (e.g., Ouchi et al. 2010; Konno et al. 2014; Thai et al. 2023; Umeda et al. 2024b), and clustering analyses of Ly α emitters (LAEs; e.g., Sobacchi & Mesinger 2015; Ouchi et al. 2018; Umeda et al. 2024b). The optical depth of the cosmic microwave background (CMB; Planck Collaboration et al. 2020) also provides critical constraints on the reionization history.

The launch of the James Webb Space Telescope (JWST) has enabled investigations of the reionization history at even higher redshifts, $z \sim 8\text{--}13$, through measurements of Ly α damping wing absorption in Lyman-break galaxies (LBGs; e.g., Curtis-Lake et al. 2023; Hsiao et al. 2024; Umeda et al. 2024a) and Ly α EW distributions (e.g., Nakane et al. 2024; Tang et al. 2024a; Jones et al. 2024). While the numerous constraints on $x_{\text{H I}}$, including measurements at high redshifts, have been obtained, many suffer from low accuracy due to limited sample sizes, or exhibit inconsistencies across the studies. Thus, it is crucial to investigate the reionization history comprehensively, from its onset (i.e., high redshifts) to the end (i.e., low redshifts), using a consistent methodology and large statistical sample. Among various methods, the Ly α EW distribution is a powerful probe of the reionization history. Although Nakane et al. (2024), Tang et al. (2024a), and Jones et al. (2024) explore this approach, their galaxy sample sizes are limited ($\sim 50\text{--}200$ galaxies) and the full JWST dataset spanning $z \sim 5$ to $z \sim 14$ is not utilized to constrain the reionization history.

In this study, we present the statistical properties of Ly α emission in 586 galaxies at $z = 4.5\text{--}14.2$ observed with JWST/NIRSpec. Using the Ly α EW distribution at $z \sim 5$ as a baseline, we investigate the evolution of EW distributions to estimate $x_{\text{H I}}$ at $z \sim 6\text{--}14$. The resulting $x_{\text{H I}}$ values provide insights into the reionization history and the primary ionizing sources. This paper is organized as follows. Section 2 describes the JWST/NIRSpec spectroscopic data and our sample selection. Section 3 presents the measurements of Ly α equivalent widths, Ly α escape fractions, and Ly α luminosity functions. In Section 4, we describe the models of EW distributions derived from semi-numerical simulations. Section 5 details the estimated $x_{\text{H I}}$ values. The implications for the reionization history and ionizing sources are discussed in Section 6. Section 7 summarizes our findings. Throughout this paper, we adopt the Planck cosmological parameters from the TT, TE, EE+lowE+lensing+BAO results (Planck Collaboration

et al. 2020): $\Omega_m = 0.31$, $\Omega_\Lambda = 0.69$, $\Omega_b = 0.049$, $h = 0.68$, $Y_p = 0.24$, and $\tau = 0.0561 \pm 0.0071$. All magnitudes are in the AB system (Oke & Gunn 1983).

2. DATA AND SAMPLE

We use JWST/NIRSpec micro-shutter assembly (MSA) spectra obtained from the following public observations: the JWST Advanced Deep Extragalactic Survey (JADES; GTO 1180/1181, GTO 1210/1286, and GO 3215, led by PIs D. Eisenstein, N. Lützgendorf, and D. Eisenstein & R. Maiolino, respectively; Bunker et al. 2023; Eisenstein et al. 2023a,b; D’Eugenio et al. 2024), the GLASS JWST Early Release Science Program (ERS 1324, PI: T. Treu; Treu et al. 2022), the Cosmic Evolution Early Release Science (CEERS; ERS 1345, PI: S. Finkelstein; Arrabal Haro et al. 2023a; Finkelstein et al. 2023), GO 1433 (PI: D. Coe; Hsiao et al. 2024) and DDT 2750 (PI: P. Arrabal Haro; Arrabal Haro et al. 2023b). All JADES programs, except GO 3215, observed the targets with the prism ($R \sim 100$) that covered $0.6\text{--}5.3\ \mu\text{m}$ and three medium resolution ($R \sim 1000$) grating/filter pairs of G140M/F070LP, G235M/F170LP, and G395M/F290LP that covered $0.7\text{--}1.3\ \mu\text{m}$, $1.7\text{--}3.1\ \mu\text{m}$, and $2.9\text{--}5.1\ \mu\text{m}$, respectively. These JADES programs, GTO 1180, 1181, 1210, and 1286, took the MSA spectra at the positions of 9, 9, 1, and 1 pointings, respectively. The exposure times per pointing were 1.1–27.8 hours for the prism and 0.9–6.9 hours for each grating. The JADES GO 3215 program did not use G235M/F170LP, and observed the targets at one pointing position with the prism, G140M/F070LP, and G395/F290LP whose exposure times were 46.7, 11.7, and 46.7 hours, respectively. The GLASS data were taken at one pointing position with high resolution ($R \sim 2700$) grating/filter pairs of G140H/F100LP ($1.0\text{--}1.8\ \mu\text{m}$), G235H/F170LP ($1.7\text{--}3.1\ \mu\text{m}$), and G395M/F290LP ($2.9\text{--}5.1\ \mu\text{m}$). For each grating/filter pair, the exposure time was 4.9 hours. The CEERS observed the targets at eight and six pointing positions with the prism and three medium resolution grating/filter pairs, respectively, which are G140M/F100LP ($1.0\text{--}1.8\ \mu\text{m}$), G235M/F170LP, and G395M/F290LP. For each prism or grating per one pointing, the exposure time was 0.9–1.7 hours. The GO 1433 and DDT 2750 programs took the prism data with integration times of 3.7 and 5.1 hours, respectively.

The JADES team has reduced the spectroscopic data using the pipeline developed by the ESA NIRSpec SOT and GTO NIRSpec teams, making it publicly available

in Data Release 1 and 3¹. Since the JADES data include spectra without reliable redshift determinations, we select galaxies whose spectroscopic redshifts are determined using emission lines and/or a strong continuum break (flag A, B, and C in the JADES catalogs; see D'Eugenio et al. 2024). In addition to the JADES galaxies in Data Release 3, we include three recently identified galaxies at $z > 13$ in the JADES program: JADES-GS-z14-0, JADES-GS-z14-1 (Carniani et al. 2024a,b), and JADES-GS-z13-1-LA (Witstok et al. 2024). Nakajima et al. (2023) and Harikane et al. (2024a) have reduced the GLASS, CEERS, GO 1433, and DDT 2750 data using the JWST pipeline version 1.8.5 with the Calibration Reference Data System context file of `jwst_1028.pmap` or `jwst_1027.pmap`, with additional processes improving the flux calibration, noise estimate, and composition. They produced catalogs containing only galaxies with redshifts determined via emission lines and/or a strong continuum break. The catalogs of the JADES team and Nakajima et al. (2023) & Harikane et al. (2024a) contain 2562 galaxies with redshifts determined at $0.1 \leq z_{\text{spec}} \leq 14.2$ in total. To investigate the reionization history using Ly α properties, we select galaxies at $z > 4.5$ with grating or prism spectra that cover the rest-frame Ly α line at $\lambda_a = 1215.67 \text{ \AA}$. This selection yields 586 galaxies: 456 from JADES, 6 from GLASS, 117 from CEERS, 1 from GO 1433, and 6 from DDT 2750. Among these, 398 galaxies have grating spectra that cover the Ly α wavelength.

3. MEASUREMENTS OF LYMAN-ALPHA EQUIVALENT WIDTHS

3.1. Lyman-alpha Flux Measurements

By fitting the observed spectra, we derive the Ly α emission properties of galaxies, including the EW. The intrinsic Ly α emission line is modeled as a Gaussian, while the continuum is assumed to follow a power-law profile. The intrinsic spectrum is expressed as:

$$f_\lambda = a \left(\frac{\lambda}{\lambda_a(1+z)} \right)^\beta + \frac{A}{\sqrt{2\pi}\sigma} \exp\left(-\frac{(\lambda - (\lambda_a + \Delta\lambda)(1+z))^2}{2\sigma^2}\right), \quad (1)$$

where a , β , A , σ , and $\Delta\lambda$ are the fitting parameters. We assume that the IGM completely absorbs photons with wavelengths shorter than $\lambda = \lambda_a(1+z)$. To account for instrumental effects, we convolve the intrinsic spectrum with the line spread function (LSF) of the NIRSpec instrument, as evaluated by Isobe et al. (2023)

¹ <https://jades-survey.github.io/scientists/data.html>

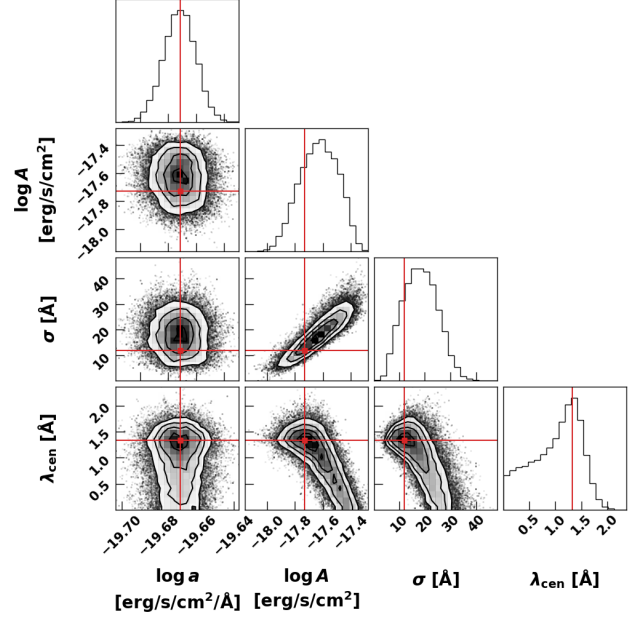


Figure 1. Posterior distributions of the fitting parameters for the grating spectrum of JADES-5591 (GN-z11), obtained by MCMC simulations. The red lines indicate the best-fit values for each parameter.

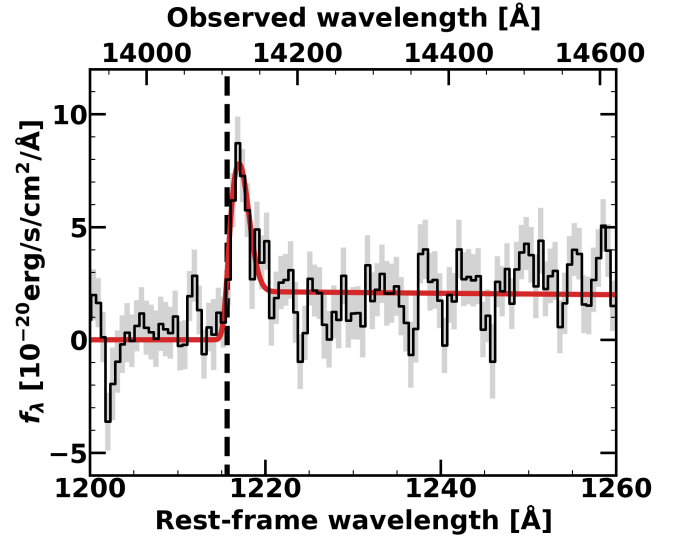


Figure 2. Grating spectrum of JADES-5591 (GN-z11) around the Ly α emission line. The red solid line represents the best-fit model spectrum obtained from MCMC simulations. The black solid line and shaded region show the observed spectrum and associated 1σ error, respectively. The black dashed line marks the Ly α wavelength.

using calibration data of a planetary nebula. Approximating the LSF as a Gaussian with standard deviation

σ_0 , the observed spectrum is expressed as:

$$f_\lambda = \frac{a}{2} \left(\frac{\lambda}{\lambda_a(1+z)} \right)^\beta \operatorname{erfc} \left(\frac{\lambda_a(1+z) - \lambda}{\sqrt{2}\sigma_0} \right) + \frac{A}{2\sqrt{2\pi}\sqrt{\sigma^2 + \sigma_0^2}} \exp \left(-\frac{(\lambda - (\lambda_a + \Delta\lambda)(1+z))^2}{2(\sigma^2 + \sigma_0^2)} \right) \times \operatorname{erfc} \left(\frac{\sigma^2\lambda_a(1+z) - \sigma^2\lambda - \sigma_0^2\Delta\lambda(1+z)}{\sqrt{2}\sigma\sigma_0\sqrt{\sigma^2 + \sigma_0^2}} \right). \quad (2)$$

We derive the fitting parameters using `emcee` (Foreman-Mackey et al. 2013) to perform Markov Chain Monte Carlo (MCMC) simulations. The wavelength range of 1200 Å–1800 Å is used for the fitting procedure. For galaxies with available grating spectra, we use these spectra for the fitting process. Due to the low signal-to-noise ratio in the grating spectra, it is challenging to simultaneously fit the continuum amplitude a and slope β . Therefore, we fix β to -2 , which is typical for star-forming galaxies (e.g., Saxena et al. 2024; Yanagisawa et al. 2024). For other galaxies, we use the prism spectra and fit all parameters, including β . The Ly α properties derived from the grating and prism spectra are shown to be consistent by Nakane et al. (2024). We determine the best-fit parameters and their 1σ uncertainties by the mode and 68% highest posterior density interval (HPDI) of the posterior distribution. Figure 1 and 2 show an example of the MCMC posterior distributions and spectrum of JADES-5591 (GN-z11), respectively. Figure A1 and Table A1 summarize the Ly α properties of all galaxies in our sample.

3.2. Lyman-alpha Equivalent Width

Using the fitting parameters derived in Section 3.1, we calculate the flux of the Ly α emission line as:

$$F_{\text{Ly}\alpha} = \int_{\lambda_a(1+z)}^{\infty} d\lambda \frac{A}{\sqrt{2\pi}\sigma} \exp \left(-\frac{(\lambda - (\lambda_a + \Delta\lambda)(1+z))^2}{2\sigma^2} \right). \quad (3)$$

The rest-frame EW is then calculated as:

$$\text{EW} = \frac{F_{\text{Ly}\alpha}}{a(1+z)}, \quad (4)$$

where a is the continuum flux density at $\lambda = \lambda_a(1+z)$ in Equation (1). We determine the best-fit EW value and its 1σ uncertainty by the mode and 68% HPDI. For galaxies without a Ly α detection at the 3σ significance level, we calculate the 3σ upper limit of the EW. For JADES-GS-z14-0, JADES-GS-z14-1, and JADES-GS-z13-1-LA, we adopt the EW values reported by Carniani et al. (2024a) and Witstok et al. (2024). Among

the 586 galaxies in our sample, Ly α emission lines are detected at the 3σ significance level for 60 galaxies.

In Figure 3, we show the distribution of M_{UV} and redshift for galaxies in our sample, with and without Ly α detection. We derive the M_{UV} values by integrating the prism spectra over the rest-frame wavelength range of 1400 Å to 1600 Å. For galaxies lacking prism spectra, the grating spectra are used instead. For galaxies observed in the GLASS and GO 1433 programs, we use the M_{UV} values obtained by Nakajima et al. (2023) and Harikane et al. (2024a), which account for lensing effects.

3.3. Lyman-alpha Fraction

In this section, we derive the Ly α fraction $X_{\text{Ly}\alpha}^{\text{EW}_{\text{th}}}$, defined as the fraction of galaxies with Ly α EW values exceeding the threshold EW_{th} , in our sample. We define $n_{\text{Ly}\alpha}$ as the number of galaxies with $\text{EW} > \text{EW}_{\text{th}}$ and N as the total number of galaxies in the sample. Since many galaxies in our sample have large EW upper limits, the true value of $n_{\text{Ly}\alpha}$ cannot be directly equated to the number of galaxies with Ly α detections at the 3σ level and the best-fit value $\text{EW} > \text{EW}_{\text{th}}$. To avoid underestimating $n_{\text{Ly}\alpha}$, we account for completeness in the analysis (see also Tang et al. 2024b and Jones et al. 2024 for completeness evaluations). By considering the uncertainties in the EW measurements for individual galaxies, we perform Monte Carlo simulations to estimate $n_{\text{Ly}\alpha}$.

We also account for the effect of binomial noise in the same manner as Gehrels (1986). When the true value of $X_{\text{Ly}\alpha}^{\text{EW}_{\text{th}}}$ is fixed, the probability of observing $n_{\text{Ly}\alpha}$ galaxies with $\text{EW} > \text{EW}_{\text{th}}$ follows:

$$p(n_{\text{Ly}\alpha} | X_{\text{Ly}\alpha}^{\text{EW}_{\text{th}}}) = {}_N C_{n_{\text{Ly}\alpha}} (X_{\text{Ly}\alpha}^{\text{EW}_{\text{th}}})^{n_{\text{Ly}\alpha}} (1 - X_{\text{Ly}\alpha}^{\text{EW}_{\text{th}}})^{N - n_{\text{Ly}\alpha}}. \quad (5)$$

Using Bayes' theorem, the posterior distribution of $X_{\text{Ly}\alpha}^{\text{EW}_{\text{th}}}$ is expressed as a beta distribution:

$$p(X_{\text{Ly}\alpha}^{\text{EW}_{\text{th}}} | n_{\text{Ly}\alpha}) = \frac{1}{B(n_{\text{Ly}\alpha} + 1, N - n_{\text{Ly}\alpha} + 1)} \times (X_{\text{Ly}\alpha}^{\text{EW}_{\text{th}}})^{n_{\text{Ly}\alpha}} (1 - X_{\text{Ly}\alpha}^{\text{EW}_{\text{th}}})^{N - n_{\text{Ly}\alpha}}, \quad (6)$$

where $B(x, y)$ is the beta function. A uniform prior is assumed for $X_{\text{Ly}\alpha}^{\text{EW}_{\text{th}}}$.

In this way, we calculate $X_{\text{Ly}\alpha}^{\text{EW}_{\text{th}}}$ while accounting for the completeness effect and binomial noise. Previous studies have investigated the Ly α fraction with $\text{EW}_{\text{th}} = 25$ Å for galaxies with $-20.25 < M_{\text{UV}} < -18.75$ (e.g., Stark et al. 2011; Ono et al. 2012; Schenker et al. 2012; Pentericci et al. 2018; Mason et al. 2019; Jones et al. 2024; Nakane et al. 2024; Napolitano et al. 2024; Tang

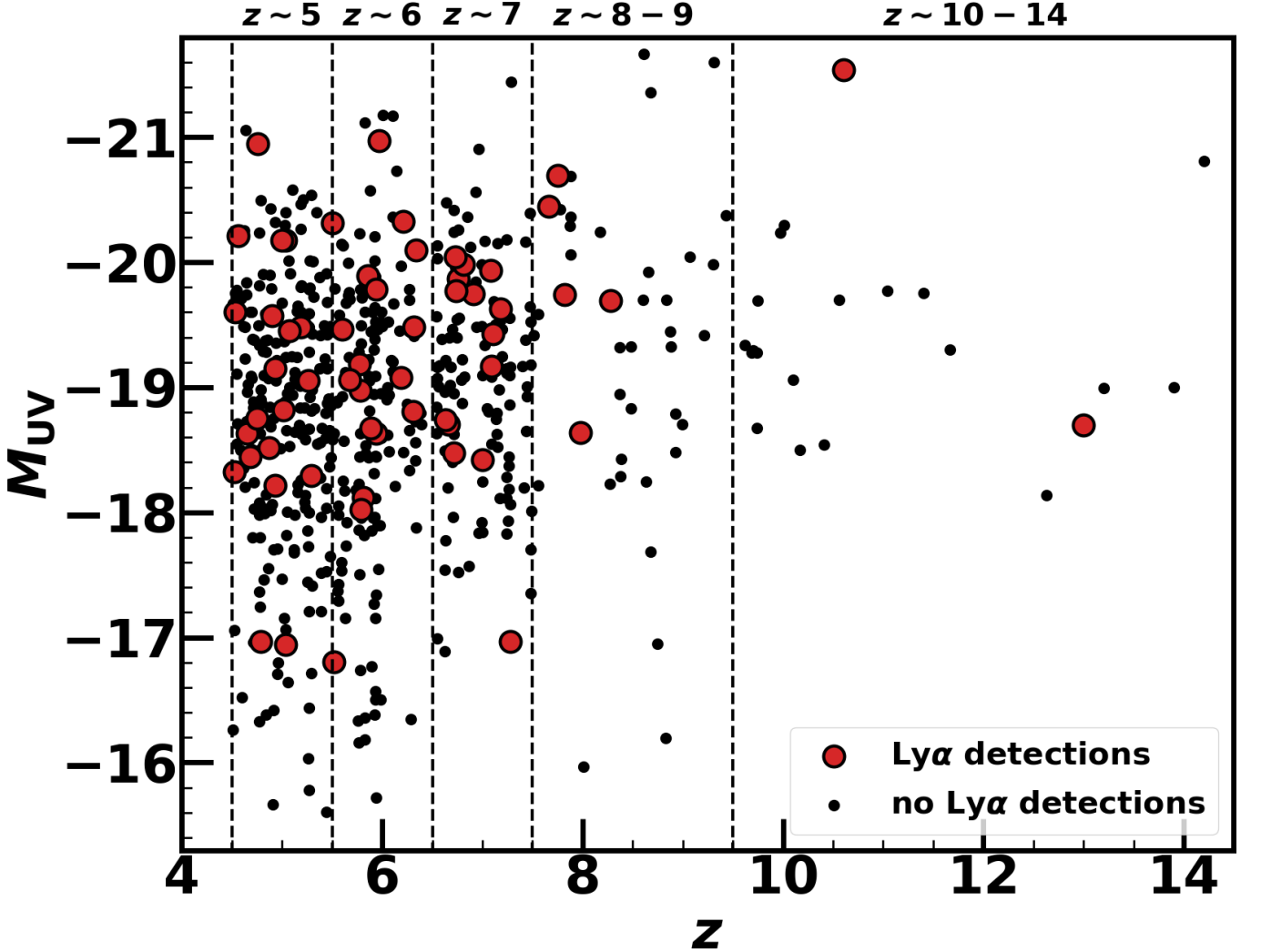


Figure 3. Distribution of absolute UV magnitudes M_{UV} and redshifts z in our sample. The red (black) circles represent galaxies with (without) 3σ Ly α detections. Our sample is divided into five redshift bins for subsequent analyses: $4.5 < z \leq 5.5$, $5.5 < z \leq 6.5$, $6.5 < z \leq 7.5$, $7.5 < z \leq 9.5$, and $9.5 < z \leq 14.2$.

et al. 2024b). In Figure 4, we compare our $X_{Ly\alpha}^{EWth}$ measurements with those from the literature. We adopt two UV magnitude bins, $-20.25 < M_{UV} < -18.75$ and $-18.75 < M_{UV} < -17.25$, as well as two threshold values, 25 \AA and 10 \AA . Although our results at $z \sim 5-6$ are lower than pre-JWST measurements, they are consistent with other JWST studies. Across all four panels in Figure 4, $X_{Ly\alpha}^{EWth}$ shows a decreasing trend with redshift, suggesting damping wing absorption by neutral hydrogen in the IGM. For instance, $X_{Ly\alpha}^{25}$ ($X_{Ly\alpha}^{10}$) decreases from $22^{+5}_{-4}\%$ ($29^{+7}_{-4}\%$) at $z \sim 5$ to $< 10\%$ ($10^{+13}_{-8}\%$) at $z \sim 11$ for galaxies with $-20.25 < M_{UV} < -18.75$. The decreasing trend is particularly pronounced for galaxies with $-18.75 < M_{UV} < -17.25$, likely due to the smaller ionized bubble radius around faint galaxies, making Ly α photons more susceptible to absorption by the IGM. No-

tably, $X_{Ly\alpha}^{EWth}$ at $z \sim 11$ for $-18.75 < M_{UV} < -17.25$ galaxies is elevated because it includes the recently identified LAE at $z = 13$, JADES-GS-z13-1-LA. In Table 1, we summarize our Ly α fractions.

3.4. Lyman-alpha Escape Fraction

We calculate the Ly α escape fraction $f_{esc}^{Ly\alpha}$ for galaxies observed with the gratings in the JADES program in our sample by the equation:

$$f_{esc}^{Ly\alpha} = \frac{F_{Ly\alpha,obs}}{F_{Ly\alpha,int}}, \quad (7)$$

where $F_{Ly\alpha,obs}$ is the Ly α flux obtained in Section 3.1 and $F_{Ly\alpha,int}$ is the intrinsic Ly α flux. We assume the electron temperature and density during the EoR are $T_e = 1.5 \times 10^4 \text{ K}$ and $n_e = 500 \text{ cm}^{-3}$, respectively (Isobe

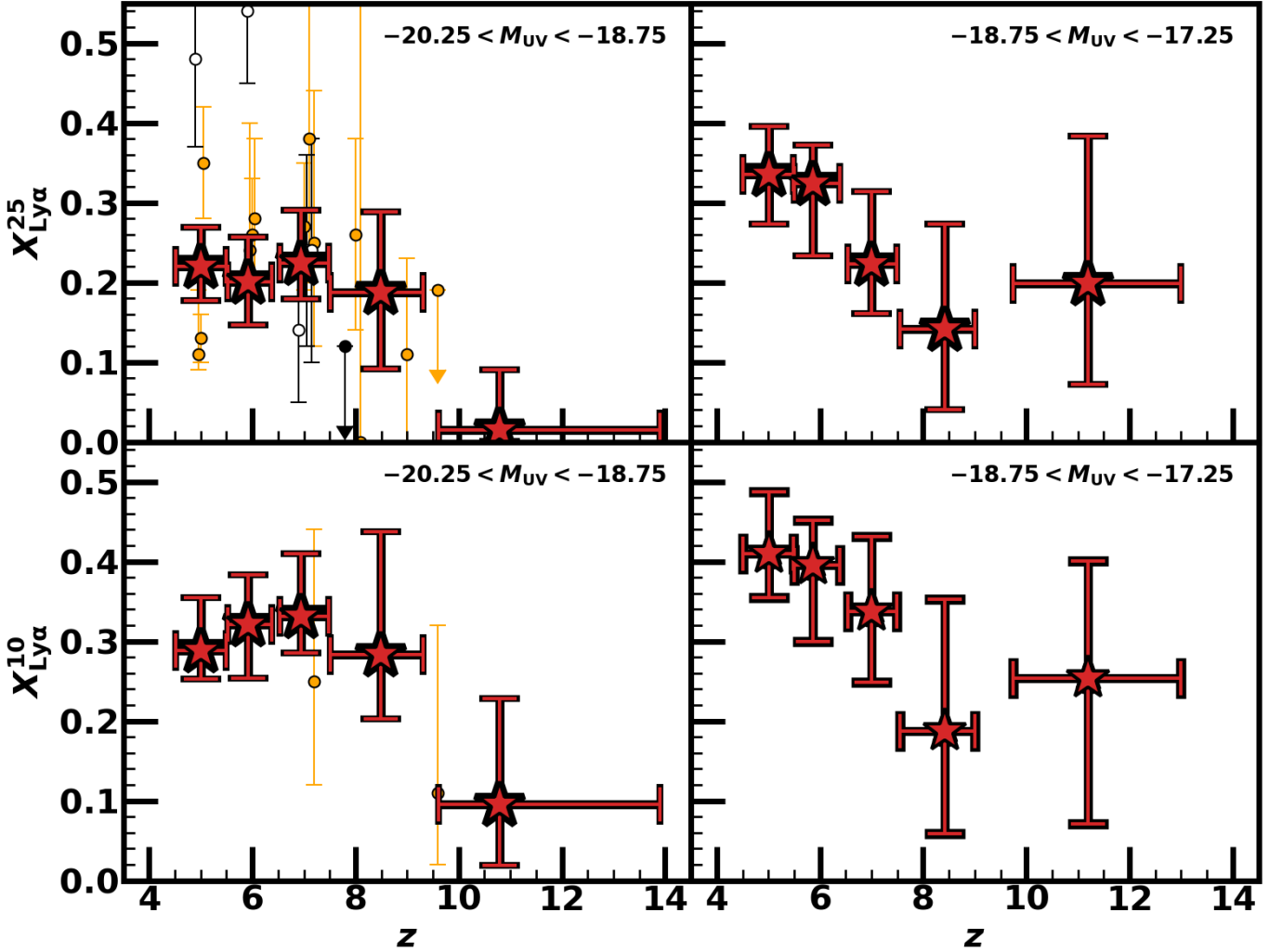


Figure 4. Ly α fraction as a function of redshift. The red stars represent $X_{\text{Ly}\alpha}^{\text{EW}_{\text{th}}}$, the fraction of galaxies in our sample with Ly α EW exceeding EW_{th} . The top two panels show $X_{\text{Ly}\alpha}^{25}$, while the bottom two panels display $X_{\text{Ly}\alpha}^{10}$. The left (right) two panels correspond to galaxies with $-20.25 < M_{\text{UV}} < -18.75$ ($-18.75 < M_{\text{UV}} < -17.25$). The white circles indicate pre-JWST measurements of $X_{\text{Ly}\alpha}^{25}$ from the literature (Stark et al. 2011; Ono et al. 2012; Schenker et al. 2012; Pentericci et al. 2018; Mason et al. 2019), while the orange circles represent recent JWST results (Jones et al. 2024; Nakane et al. 2024; Napolitano et al. 2024; Tang et al. 2024b). Across all panels, $X_{\text{Ly}\alpha}^{\text{EW}_{\text{th}}}$ decreases with redshift, suggesting increasing damping wing absorption by neutral hydrogen in the IGM.

Table 1. Ly α Fraction

$-20.25 < M_{\text{UV}} < -18.75$			$-18.75 < M_{\text{UV}} < -17.25$		
z	$X_{\text{Ly}\alpha}^{25}$	$X_{\text{Ly}\alpha}^{10}$	z	$X_{\text{Ly}\alpha}^{25}$	$X_{\text{Ly}\alpha}^{10}$
(1)	(2)	(3)	(1)	(2)	(3)
$5.01^{+0.48}_{-0.50}$	$0.22^{+0.05}_{-0.04}$	$0.29^{+0.07}_{-0.04}$	$5.01^{+0.47}_{-0.50}$	$0.34^{+0.06}_{-0.06}$	$0.41^{+0.08}_{-0.06}$
$5.92^{+0.46}_{-0.40}$	$0.20^{+0.06}_{-0.05}$	$0.32^{+0.06}_{-0.07}$	$5.87^{+0.52}_{-0.36}$	$0.32^{+0.05}_{-0.09}$	$0.40^{+0.06}_{-0.10}$
$6.95^{+0.53}_{-0.41}$	$0.22^{+0.07}_{-0.04}$	$0.33^{+0.08}_{-0.05}$	$7.01^{+0.48}_{-0.46}$	$0.22^{+0.09}_{-0.06}$	$0.34^{+0.09}_{-0.09}$
$8.49^{+0.82}_{-0.98}$	$0.19^{+0.10}_{-0.10}$	$0.28^{+0.15}_{-0.08}$	$8.42^{+0.58}_{-0.87}$	$0.14^{+0.13}_{-0.10}$	$0.19^{+0.17}_{-0.13}$
$10.80^{+3.10}_{-1.18}$	$0.02^{+0.08}_{-0.01}$	$0.10^{+0.13}_{-0.08}$	$11.19^{+1.81}_{-1.45}$	$0.20^{+0.19}_{-0.13}$	$0.25^{+0.15}_{-0.18}$

NOTE—(1): Mean redshift and the lower/upper boundary of a subsample. (2): Fraction of galaxies with Ly α EW > 25 Å. (3): Fraction of galaxies with Ly α EW > 10 Å.

et al. 2023; Nakajima et al. 2023). Using PyNeb (Luridiana et al. 2015), we derive the intrinsic flux ratios of Ly α and Balmer lines under the assumption of case B recombination: $F_{\text{Ly}\alpha}/F_{\text{H}\alpha} = 8.98$, $F_{\text{Ly}\alpha}/F_{\text{H}\beta} = 25.02$, and $F_{\text{Ly}\alpha}/F_{\text{H}\gamma} = 52.89$. We use the flux values of Balmer lines in the JADES catalogs (D’Eugenio et al. 2024) and calculate $f_{\text{esc}}^{\text{Ly}\alpha}$ for galaxies with H α , H β , or H γ flux measurements. We assume the dust extinction of Balmer lines is negligible. We also calculate the ionizing photon production efficiency under the assumption of zero LyC escape ($\xi_{\text{ion},0}$) from Balmer line fluxes. Assuming ionizing photons do not escape from a galaxy, the amount of ionizing photons produced in a unit time is given by

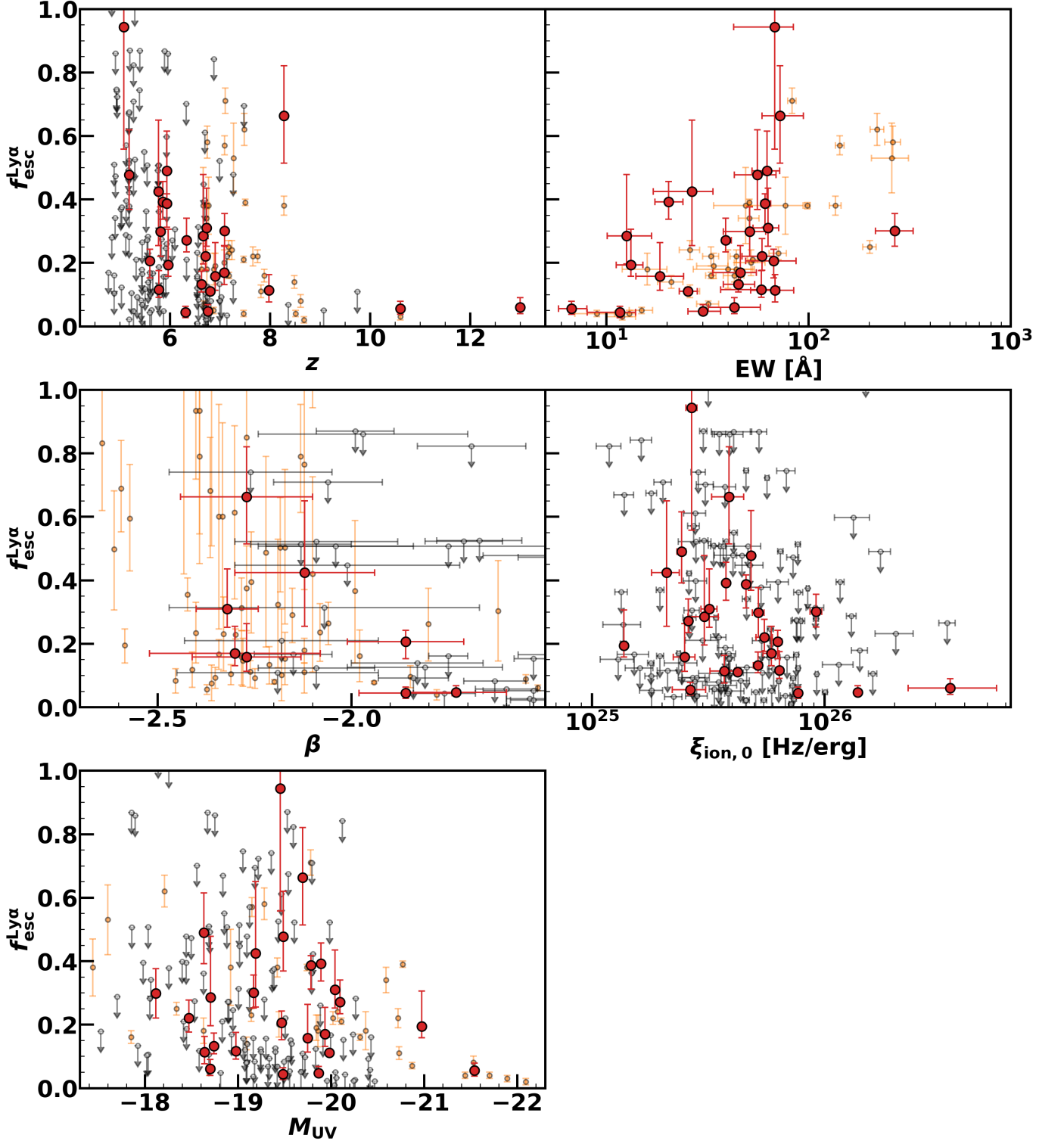


Figure 5. Escape fraction of Ly α photons ($f_{\text{esc}}^{\text{Ly}\alpha}$) as a function of various galaxy properties. Top left: $f_{\text{esc}}^{\text{Ly}\alpha}$ versus redshift (z). Top right: $f_{\text{esc}}^{\text{Ly}\alpha}$ versus Ly α EW. Middle left: $f_{\text{esc}}^{\text{Ly}\alpha}$ versus UV continuum slope (β). Middle right: $f_{\text{esc}}^{\text{Ly}\alpha}$ versus ionizing photon production efficiency under the assumption of zero LyC escape ($\xi_{\text{ion},0}$). Bottom left: $f_{\text{esc}}^{\text{Ly}\alpha}$ versus UV magnitude (M_{UV}). The red circles represent galaxies with Ly α detection at the 3σ level, while the open circles indicate galaxies without Ly α detection. Yellow circles show measurements of Tang et al. (2024a) and Tang et al. (2024b).

Table 2. Ly α LF at $z = 5 - 14$

z	$\log \Phi_{\text{Ly}\alpha}(L_{\text{Ly}\alpha})$ ($\text{Mpc}^{-3} \text{ dex}^{-1}$)		
	$\log L_{\text{Ly}\alpha} = 42.3$ (erg s^{-1})	$\log L_{\text{Ly}\alpha} = 42.8$ (erg s^{-1})	$\log L_{\text{Ly}\alpha} = 43.3$ (erg s^{-1})
$z \sim 5$	$-2.45^{+0.11}_{-0.12}$	$-2.80^{+0.09}_{-0.10}$	$-3.49^{+0.15}_{-0.15}$
$z \sim 6$	$-2.80^{+0.08}_{-0.13}$	$-3.25^{+0.14}_{-0.15}$	$-4.00^{+0.06}_{-0.26}$
$z \sim 7$	$-2.91^{+0.20}_{-0.31}$	$-3.87^{+0.19}_{-0.24}$	$-4.47^{+0.29}_{-0.14}$
$z \sim 8 - 9$	$-3.59^{+0.36}_{-0.48}$	$-4.38^{+0.11}_{-0.74}$	-
$z \sim 10 - 14$	$-4.57^{+0.52}_{-0.83}$	$-6.07^{+0.65}_{-0.59}$	-

the equation (Osterbrock & Ferland 2006):

$$\dot{n} = 7.28 \times 10^{11} \text{ s}^{-1} L(\text{H}\alpha) / (\text{erg s}^{-1}), \quad (8)$$

where $L(\text{H}\alpha)$ is the H α luminosity. For galaxies with H β or H γ measurements but without H α measurements, we use Balmer decrements $\text{H}\alpha/\text{H}\beta = 2.79$ and $\text{H}\alpha/\text{H}\gamma = 5.89$ to derive H α luminosity. Then $\xi_{\text{ion},0}$ is obtained by the equation:

$$\xi_{\text{ion},0} = \frac{\dot{n}}{L_{\text{UV}}}, \quad (9)$$

where L_{UV} is the luminosity in units of $\text{erg s}^{-1} \text{ Hz}^{-1}$ at $\lambda = 1500 \text{ \AA}$.

In Figure 5, we show $f_{\text{esc}}^{\text{Ly}\alpha}$ as a function of redshift, Ly α EW, UV continuum slope (β), $\xi_{\text{ion},0}$, and M_{UV} . We use the β values measured by Yanagisawa et al. (2024). For JADES-GS-z13-1-LA, we adopt the values of $f_{\text{esc}}^{\text{Ly}\alpha}$, β , $\xi_{\text{ion},0}$, and M_{UV} reported by Witstok et al. (2024). The $f_{\text{esc}}^{\text{Ly}\alpha}$ values decrease with z and increase with Ly α EW, suggesting increasing damping wing absorption in the IGM. Galaxies with a red UV slope, high $\xi_{\text{ion},0}$, and bright M_{UV} tend to have a low $f_{\text{esc}}^{\text{Ly}\alpha}$. This correlation can be explained as follows: In bright galaxies with a thick gaseous disc, the LyC escape fraction is low, and ionizing photons are absorbed within the interstellar medium (ISM), resulting in a high $\xi_{\text{ion},0}$. The UV spectrum becomes redder due to an increased contribution from nebular emission. Ly α photons are also less likely to escape in such galaxies, leading to a low $f_{\text{esc}}^{\text{Ly}\alpha}$.

3.5. Lyman-alpha Luminosity Functions

In this section, we derive the Ly α luminosity functions from $z \sim 5$ to $z \sim 14$, using the Ly α EW distributions and UV luminosity functions. The Ly α EW, Ly α luminosity $L_{\text{Ly}\alpha}$, and UV magnitude M_{UV} are connected by the equation:

$$\text{EW} = L_{\text{Ly}\alpha} \frac{\lambda_a^2}{4\pi cd^2} 10^{0.4(M_{\text{UV}}+48.6)}, \quad (10)$$

Table 3. Best-fit Parameters for Ly α LF at $z = 5 - 14$

z	$\log \phi^*$	$\log L^*$	α
	($\text{Mpc}^{-3} \text{ dex}^{-1}$)	(erg s^{-1})	
$5.01^{+0.47}_{-0.50}$	$-2.50^{+0.06}_{-0.06}$	42.69 (fixed)	-1.61 (fixed)
$5.90^{+0.49}_{-0.40}$	$-3.03^{+0.07}_{-0.13}$	42.75 (fixed)	-1.39 (fixed)
$6.96^{+0.52}_{-0.42}$	$-4.45^{+0.09}_{-0.10}$	43.23 (fixed)	-2.49 (fixed)
$8.41^{+1.03}_{-0.90}$	$-4.98^{+0.21}_{-0.35}$	43.03 (fixed)	-2.56 (fixed)
$11.00^{+3.18}_{-1.39}$	$-6.33^{+0.44}_{-0.50}$	43.03 (fixed)	-2.56 (fixed)

where $d = 10 \text{ pc/cm} = 3.09 \times 10^{19}$. We assume a flat continuum at $\lambda = 1216 \text{ \AA} - 1500 \text{ \AA}$, which is the same assumption as the UV slope $\beta = -2$ for the grating spectra in Section 3.1. Then, the Ly α luminosity function is derived by the equation:

$$\Phi_{\text{Ly}\alpha}(L_{\text{Ly}\alpha}) = \int dM_{\text{UV}} \Phi_{\text{UV}}(M_{\text{UV}}) \text{EW} p(\text{EW}, M_{\text{UV}}), \quad (11)$$

where $\Phi_{\text{UV}}(M_{\text{UV}})$ is the UV luminosity function and $p(\text{EW}, M_{\text{UV}})$ is the Ly α EW distribution for galaxies with the UV magnitude M_{UV} . Equation (10) is substituted to Equation (11).

The Ly α EW distribution $p(\text{EW}, M_{\text{UV}})$ is derived from our measurements. To account for the dependence of the EW distribution on M_{UV} , We divide our sample into five M_{UV} bins: $M_{\text{UV}} \leq -20.0$, $-20.0 < M_{\text{UV}} \leq -19.0$, $-19.0 < M_{\text{UV}} \leq -18.0$, $-18.0 < M_{\text{UV}} \leq -17.0$, and $-17.0 < M_{\text{UV}}$. We determine the M_{UV} bins so that each bin contains at least 20 galaxies at $z \sim 5$. We numerically construct the distribution from the histogram of the observed EW values. For the UV luminosity function $\Phi_{\text{UV}}(M_{\text{UV}})$, we adopt the form of the Schechter function:

$$\Phi_{\text{UV}}(M_{\text{UV}}) = \frac{\ln 10}{2.5} \phi^* 10^{-0.4(M_{\text{UV}} - M_{\text{UV}}^*)(\alpha+1)} \times \exp\left(-10^{-0.4(M_{\text{UV}} - M_{\text{UV}}^*)}\right). \quad (12)$$

The parameters ϕ^* , M_{UV}^* , and α are taken from the literature (Bouwens et al. 2021; Harikane et al. 2024b). Note that the EW values measured in this study are not corrected for slit loss effects. From Nakane et al. (2024), the EW of the entire galaxy, including the extended components outside the slit, is obtained by multiplying the measured EW value by two to correct for the slit loss effect of NIRSspec.

We show the results of Ly α luminosity functions for $\log L_{\text{Ly}\alpha} = 42.3$, 42.8, and 43.3 erg s^{-1} in Figure 6 and Table 2. The error of the Ly α luminosity function at each luminosity bin is estimated using bootstrap sampling of the Ly α EW distribution and the error of ϕ^*

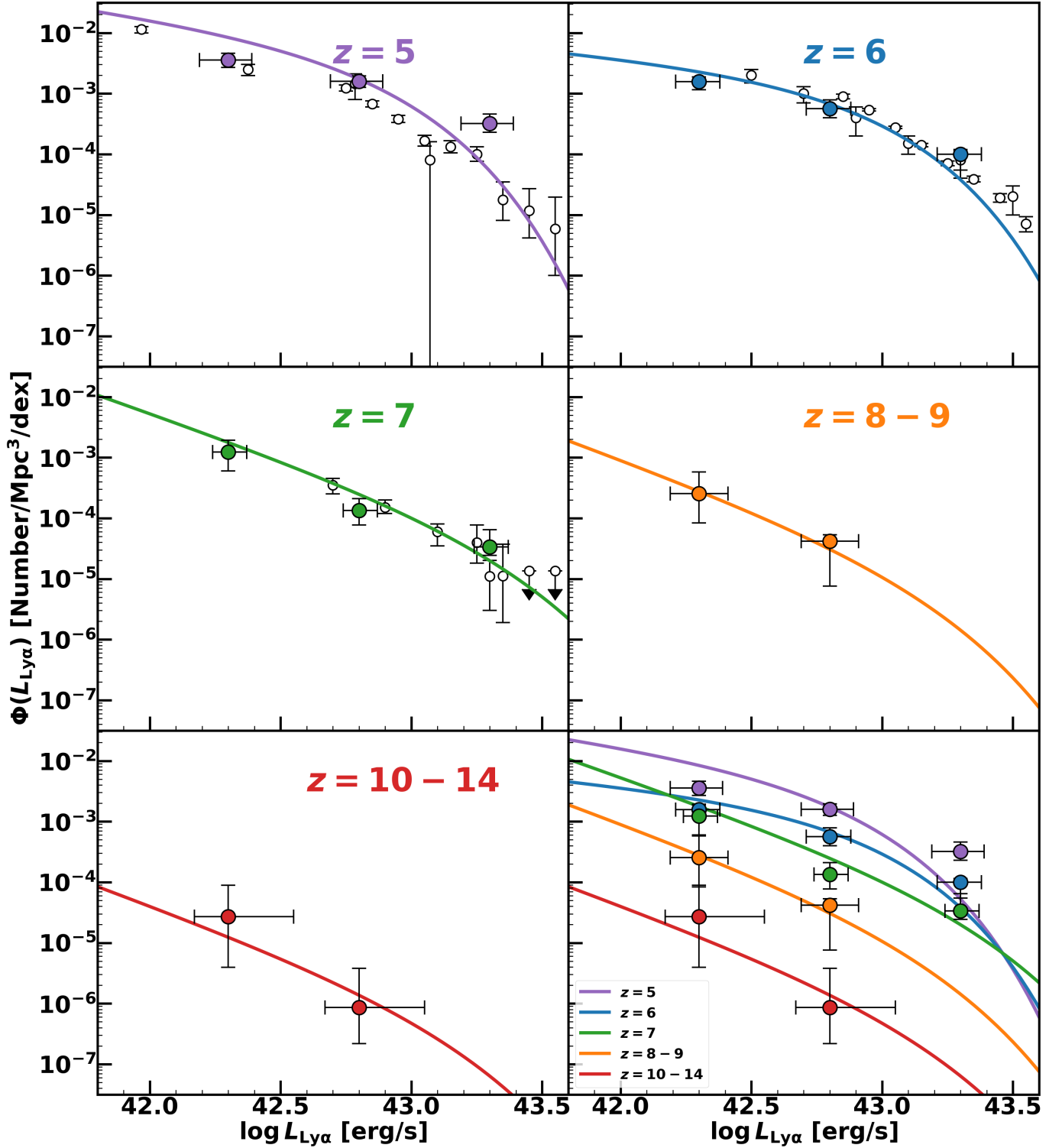


Figure 6. Evolution of Ly α luminosity function. The Ly α luminosity function at $z = 5$ (top left), $z = 6$ (top right), $z = 7$ (middle left), $z = 8 - 9$ (middle right), and $z = 10 - 14$ (bottom left) are shown. The solid lines represent the best-fit Schechter functions. The open circles represent the measurements of Ly α luminosity function from Ouchi et al. (2008), Drake et al. (2017), Ota et al. (2017), and Umeda et al. (2024b). The bottom right panel summarizes the evolution of the Ly α luminosity function.

in the UV luminosity functions presented in [Bouwens et al. \(2021\)](#) and [Harikane et al. \(2024b\)](#). The error in the x-direction in Figure 6 corresponds to the width of the redshift bin. The Ly α luminosity function at $\log L_{\text{Ly}\alpha} = 42 - 43 \text{ erg s}^{-1}$ decreases by ~ 3 dex from $z \sim 5$ to $z \sim 10 - 14$, suggesting an increase in damping wing absorption.

We fit the Ly α luminosity function with the Schechter function form:

$$\begin{aligned} \Phi_{\text{Ly}\alpha}(L_{\text{Ly}\alpha}) \\ = \ln 10 \phi^* \left(\frac{L_{\text{Ly}\alpha}}{L^*} \right)^{\alpha+1} \exp \left(-\frac{L_{\text{Ly}\alpha}}{L^*} \right). \end{aligned} \quad (13)$$

We fix the L^* and α values at $z \sim 5, 6, 7, 8 - 9$, and $10 - 14$ to the ones at $z = 4.9, 5.7, 7.0, 7.3$, and 7.3 derived by [Umeda et al. \(2024b\)](#). We obtain the posterior distribution of ϕ^* with the MCMC method. The best-fit parameters are presented in Table 3.

4. MODELING LYMAN-ALPHA EW DISTRIBUTIONS

In this section, we construct theoretical Ly α EW distribution models in order to estimate x_{HI} by comparing them with the observed EW values. We assume that the Ly α emission line at $z \sim 5$ is not absorbed by the IGM and that the intrinsic EW distribution at $z \gtrsim 6$ is identical to the distribution at $z \sim 5$. The models of EW probability distribution are then calculated by multiplying the Ly α photon transmittance through the IGM (Section 4.2) to the intrinsic EW distribution (Section 4.1).

4.1. Lyman-alpha EW Distribution at $z = 5$

We use the EW values of galaxies in the redshift range $4.5 < z < 5.5$ to estimate the intrinsic Ly α EW distribution. For details about the derivation of the EW distribution, see Section 3.5. Previous studies have parameterized the intrinsic distribution using an exponential (e.g., [Dijkstra et al. 2011](#)), an exponential plus a delta function (e.g., [Mason et al. 2018](#)), or a log-normal distribution (e.g., [Tang et al. 2024b](#)). In this work, we do not assume any specific functional form and instead numerically derive the distribution from the histogram of the observed EW values for each UV magnitude bin.

4.2. 21cmFAST Simulation

To model EW distributions at $z \gtrsim 6$, we calculate the transmission fraction of Ly α photons following the methodology presented in [Mason et al. \(2018\)](#). The optical depth of Ly α photons, τ , depends on velocity v , redshift z , the volume-averaged neutral fraction x_{HI} , and

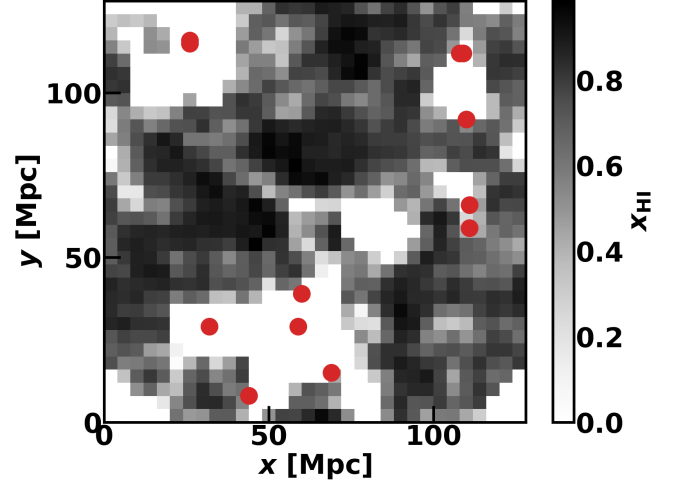


Figure 7. Spatial distribution of neutral regions (black) and halos (red) from our 21cmFAST simulation box at $z = 7$. While the full simulation uses a three-dimensional 1024^3 cMpc^3 box, this figure shows a two-dimensional slice of 128^2 cMpc^2 .

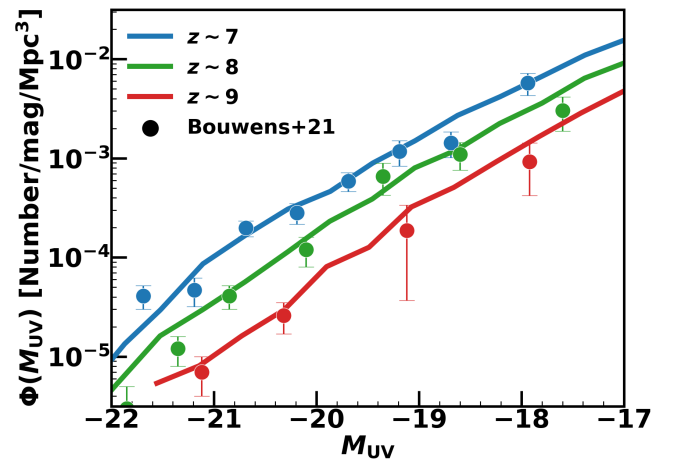


Figure 8. UV luminosity functions at $z = 7, 8$, and 9 . The blue, green, and red solid lines represent the UV luminosity functions at $z = 7, 8$, and 9 derived from our 21cmFAST simulation. The circles show the observational UV luminosity functions reported by [Bouwens et al. \(2021\)](#), which agree with our simulation results.

the UV magnitude of the Ly α -emitting galaxy M_{UV} . We assume that Ly α photons blueward of the circular velocity $v_c = (10GM_h H(z))^{1/3}$ are completely absorbed by the circumgalactic medium and the residual neutral gas within the ionized region in the IGM. Here, M_h is the halo mass. We adopt the relation between M_{UV} and M_h derived by [Mason et al. \(2015, 2018\)](#):

$$\log M_h [M_\odot] = \gamma(M_{\text{UV}} + 20.0 + 0.26z) + 11.75, \quad (14)$$

where $\gamma = -0.3$ for $M_{\text{UV}} > -20.0 - 0.26z$ and $\gamma = -0.7$ otherwise.

We assume that the optical depth at $v > v_c$ is solely due to damping wing absorption in the IGM. To calculate this, we use the semi-numerical cosmological simulation code **21cmFAST v3** (Mesinger et al. 2011; Murray et al. 2020) to model the IGM ionization and galaxy distributions. We run a **21cmFAST** simulation from $z = 15$ to $z = 4$ with a box size of 1024^3 cMpc 3 , a halo distribution map resolution of 1 Mpc/cell, and an ionization box resolution of 4 Mpc/cell. We calculate the IGM ionization and halo distribution maps from the same initial density map. Figure 7 illustrates a portion of our simulation box at $z = 7$.

The reionization process in **21cmFAST** is primarily determined by two parameters: the ionizing efficiency ζ and the minimum virial temperature $T_{\text{vir}}^{\text{min}}$. ζ represents the number of ionizing photons per baryon inside a halo. It is expressed as

$$\zeta = N_\gamma f_{\text{esc}} f_\star, \quad (15)$$

where N_γ is the number of ionizing photons per stellar baryon, f_{esc} is the escape fraction of ionizing photons, and f_\star is the fraction of stellar baryons relative to the total baryons in a halo. Since the number of ionizing photons emitted from a halo is determined solely by ζ , we do not assume specific values for N_γ and f_\star . $T_{\text{vir}}^{\text{min}}$ defines the threshold temperature at which a halo can emit ionizing photons. This temperature corresponds to the minimum halo mass capable of emitting ionizing photons M_h^{min} , which is given by the relation (Barkana & Loeb 2001):

$$T_{\text{vir}}^{\text{min}} = 1.98 \times 10^4 \left(\frac{\mu}{0.6} \right) \times \left(\frac{M_h^{\text{min}}}{10^8 h^{-1} M_\odot} \right)^{2/3} \left(\frac{\Omega_m \Delta_c}{\Omega_m^z 18\pi^2} \right)^{1/3} \left(\frac{1+z}{10} \right) \text{K}, \quad (16)$$

where μ is the mean molecular weight, $\Omega_m^z = \frac{\Omega_m(1+z)^3}{\Omega_m(1+z)^3 + 1 - \Omega_m}$, $\Delta_c = 18\pi^2 + 82d - 39d^2$, with $d = \Omega_m^z - 1$. In our simulation, we adopt fiducial parameters of $\zeta = 20$ and $T_{\text{vir}}^{\text{min}} = 5 \times 10^4$ K. We also set the mean free path of ionizing photons within ionized regions R_{mfp} to 15 cMpc to account for the effects of recombination. In the **21cmFAST** simulations, R_{mfp} is treated as the maximum horizon of ionizing photons. For the determination of these fiducial parameters, see Mesinger et al. (2016) and Greig & Mesinger (2017).

In our simulation box, we confirm that the UV luminosity function during the EoR and the CMB optical depth are reproduced. We convert the halo mass function in our simulation box into the UV luminosity function using Equation (14). Figure 8 shows the UV luminosity functions at $z = 7, 8,$ and 9 from our simulation.

Our results are consistent with the measurements by Bouwens et al. (2021). The optical depth of the CMB, τ_e , corresponding to the **21cmFAST** model reionization history, is calculated as:

$$\tau_e = \int_0^{1090} dz (1 - x_{\text{HI}}(z)) \frac{c(1+z)^2}{H(z)} \times n_0 \sigma_{\text{T}} \left(1 + \frac{\eta Y_p}{4X_p} \right), \quad (17)$$

where σ_{T} is the Thomson scattering cross section, $X_p = 1 - Y_p (= 0.76)$ is the hydrogen abundance, and η represents the relative ionization fraction of helium to hydrogen. Following Kuhlen & Faucher-Giguère (2012), we assume helium is singly ionized ($\eta = 1$) at $z > 4$ and doubly ionized ($\eta = 2$) at $z \leq 4$. The reionization history $x_{\text{HI}}(z)$ is obtained from the **21cmFAST** simulations. The obtained value, $\tau_e = 0.054$, agrees with the Planck measurement ($\tau_e = 0.0561 \pm 0.0071$; Planck Collaboration et al. 2020). Since our simulation reproduces key observations related to structure formation and reionization, it is well-suited for modeling the EW distribution during the EoR.

We calculate the optical depth of Ly α photons emitted from a halo with mass M_h at redshift z in the simulation box, as a function of volume-averaged neutral fractions x_{HI} . Since the reionization morphology has only a small effect when using galaxies spread in redshift ($\Delta z > 0.1$ bin; e.g., Sobacchi & Mesinger 2015), we superimpose the ionization maps with different x_{HI} values from a single simulation onto the halo distribution map. This approach follows the methodology of Mason et al. (2018).

Based on the formulation of Miralda-Escudé (1998), the optical depth is calculated using the following equation:

$$\begin{aligned} \tau(v, z, x_{\text{HI}}, M_{\text{UV}}(M_h)) &= \int_5^z \frac{dz'}{1+z'} \frac{c}{H(z')} n_0 (1+z')^3 X_{\text{HI}}(z', x_{\text{HI}}, M_{\text{UV}}) \\ &\times \sigma \left(\frac{\omega}{\omega_a} = \frac{1+z'}{(1+z)(1+v/c)} \right). \end{aligned} \quad (18)$$

Here, we assume that reionization has ended at $z = 5$. The halo mass M_h is converted into M_{UV} using Equation (14). $X_{\text{HI}}(z, x_{\text{HI}}, M_{\text{UV}})$ is the line-of-sight neutral fraction distribution of the halo in the simulation box, which differs from the volume-averaged neutral fraction x_{HI} at redshift z . Although Miralda-Escudé (1998) assumes a constant x_{HI} value, we consider the effect of inhomogeneous neutral hydrogen distributions. The value n_0 represents the comoving hydrogen number density. $\sigma(\omega)$ is the Ly α damping wing cross section at the ve-

locity $v = \omega/(2\pi)$, given by

$$\sigma(\omega) = \frac{3\lambda_a^2 \Lambda^2}{8\pi} \frac{(\omega/\omega_a)^4}{(\omega - \omega_a)^2 + (\Lambda^2/4)(\omega/\omega)^6}, \quad (19)$$

where $\omega_a = 2\pi c/\lambda_a$ and $\Lambda = 6.25 \times 10^8 \text{ s}^{-1}$.

Using the optical depth, we calculate the transmission fraction \mathcal{T} . Following Mason et al. (2018), we model the Ly α lineshape after transmission through the ISM as a Gaussian, with the full width at half maximum (FWHM) equal to the peak velocity offset Δv . We use the value of Δv which follows a halo mass-dependent log-normal distribution described in Mason et al. (2018), whose peak is expressed as:

$$\log \Delta v_{\text{peak}}(M_h) = 0.32 \log \left(\frac{M_h}{1.55 \times 10^{12} M_\odot} \right) + 2.48. \quad (20)$$

The transmission fraction is then calculated using the equation:

$$\begin{aligned} \mathcal{T}(z, x_{\text{HI}}, M_{\text{UV}}, \Delta v) \\ = \frac{\int_{v_c}^{\infty} dv \exp\left(-\frac{(v-\Delta v)^2}{2\sigma_a^2}\right) \exp(-\tau(v, z, x_{\text{HI}}, M_{\text{UV}}))}{\int_{v_c}^{\infty} dv \exp\left(-\frac{(v-\Delta v)^2}{2\sigma_a^2}\right)}, \end{aligned} \quad (21)$$

where $2\sqrt{2 \ln 2} \sigma_a = \Delta v$. Because \mathcal{T} varies significantly across sightlines, we calculate \mathcal{T} for all the halos in the simulation box to derive the transmission fraction as a probability distribution $p(\mathcal{T} | z, x_{\text{HI}}, M_{\text{UV}}, \Delta v)$.

4.3. Lyman-alpha EW Distribution at $z \gtrsim 6$

By combining the observed intrinsic EW distribution with the simulated transmission distribution, we construct models of EW distributions at $z \gtrsim 6$ as a function of x_{HI} and M_{UV} through the following steps. First, an intrinsic EW value EW_{int} is randomly selected from the distribution derived in Section 4.1. Next, the velocity offset is randomly determined from the distribution $p(\Delta v | M_{\text{UV}})$. Using this velocity offset, the transmission fraction \mathcal{T} is randomly chosen from the distribution $p(\mathcal{T} | z, x_{\text{HI}}, M_{\text{UV}}, \Delta v)$ derived in Section 4.2. The observed EW value is then calculated as $\text{EW}_{\text{obs}} = \text{EW}_{\text{int}} \mathcal{T}$. By repeating this procedure multiple times, we obtain the observed EW distribution $p(\text{EW} | z, x_{\text{HI}}, M_{\text{UV}})$. In Figure 9, we present examples of the distributions for galaxies with $M_{\text{UV}} \sim -18.5$ at $z = 7$. As x_{HI} increases, Ly α photons experience greater absorption, reducing the likelihood of observing large EW values.

5. OBSERVATIONAL CONSTRAINTS ON THE COSMIC REIONIZATION HISTORY

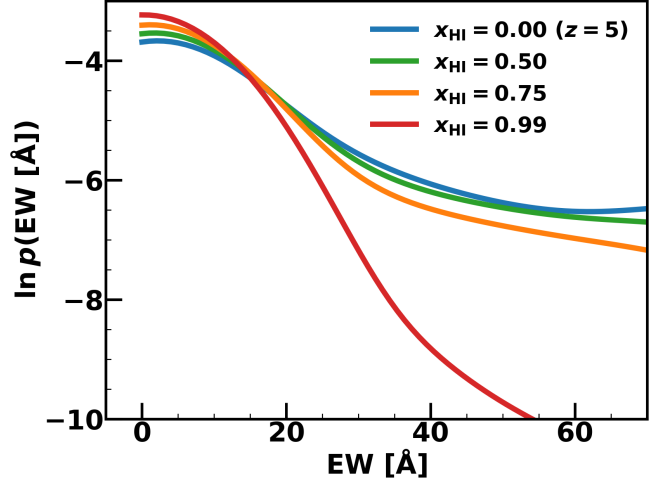


Figure 9. Models of Ly α EW distributions for galaxies with $M_{\text{UV}} \sim -18.5$ at $z = 7$. We show the distributions for four values of x_{HI} . The distribution for $x_{\text{HI}} = 0.00$ represents the intrinsic distribution at $z = 5$ without IGM absorption. As x_{HI} increases, the probability of observing large EW values decreases due to stronger absorption by the IGM.

5.1. Neutral Fraction Estimate

By comparing the observed EW values to the models of EW distributions, we estimate the neutral fraction x_{HI} . We divide $z > 5.5$ galaxies in our sample into four redshift bins: $5.5 < z \leq 6.5$, $6.5 < z \leq 7.5$, $7.5 < z \leq 9.5$, and $9.5 < z \leq 14.2$. The number of galaxies in each bin is 159, 128, 42, and 21, respectively. At each redshift bin, the posterior distribution of x_{HI} is derived using Bayes' theorem:

$$\begin{aligned} p_z(x_{\text{HI}} | \{\text{EW}, M_{\text{UV}}\}) \\ \propto \prod_i p(\text{EW}_i | z, x_{\text{HI}}, M_{\text{UV},i}) p(x_{\text{HI}}), \end{aligned} \quad (22)$$

where EW_i and $M_{\text{UV},i}$ are the EW value and UV magnitude of the i th galaxy, respectively. We assume a flat prior distribution for x_{HI} . Given that the EW value of each galaxy contains an error from spectral fitting, the equation is rewritten as:

$$\begin{aligned} p_z(x_{\text{HI}} | \{\text{EW}, M_{\text{UV}}\}) \\ \propto \prod_i \int d\text{EW} p(\text{EW} | z, x_{\text{HI}}, M_{\text{UV},i}) p_i(\text{EW}), \end{aligned} \quad (23)$$

where $p_i(\text{EW})$ is the posterior EW distribution of the i th galaxy obtained from spectral MCMC fitting, and $p(\text{EW} | z, x_{\text{HI}}, M_{\text{UV},i})$ is the EW distribution model derived in Section 4.3. The posterior distributions of x_{HI} for each redshift bin are shown in Figure 10. We determine the x_{HI} values and their 1σ errors by the mode and 68% HPDI of the posterior distributions. The estimated values are $x_{\text{HI}} = 0.17_{-0.16}^{+0.23}$, $0.63_{-0.28}^{+0.18}$, $0.79_{-0.21}^{+0.13}$,

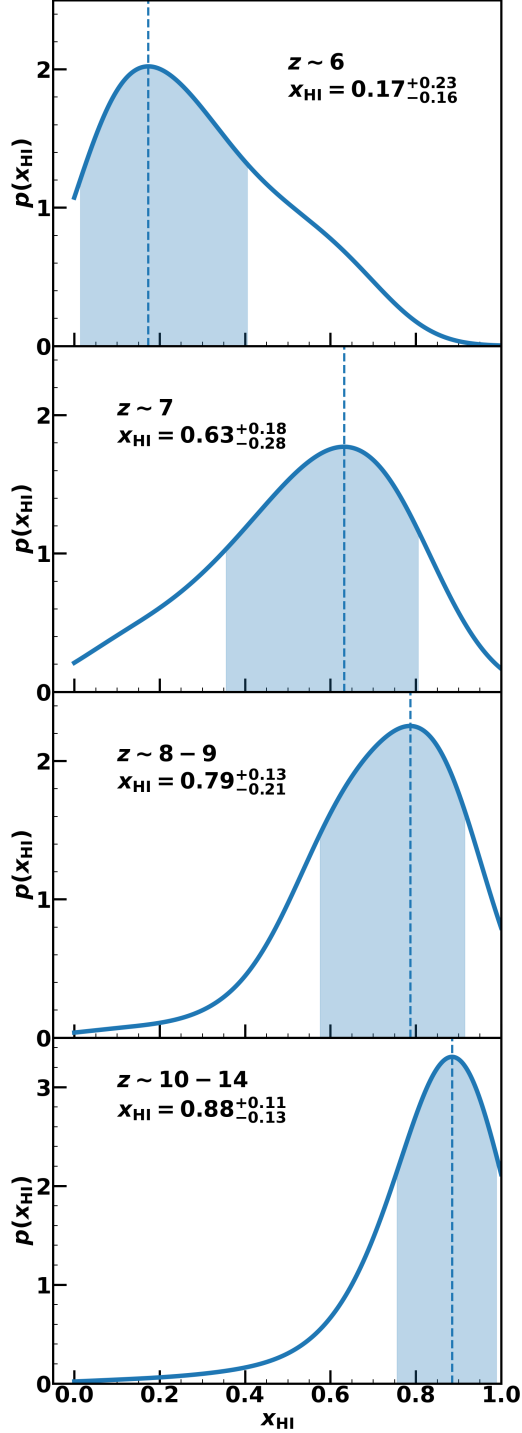


Figure 10. Posterior distributions of x_{HI} at $z \sim 6, 7, 8-9$, and $10-14$ (from top to bottom). The vertical dashed lines represent the mode of each distribution, and the shaded regions indicate the 68% HPDI. The estimated values are $x_{\text{HI}} = 0.17^{+0.23}_{-0.16}$, $0.63^{+0.18}_{-0.28}$, $0.79^{+0.13}_{-0.21}$, and $0.88^{+0.11}_{-0.13}$, respectively.

and $0.88^{+0.11}_{-0.13}$ at $z \sim 6, 7, 8-9$, and $10-14$, respectively (Table 4).

Table 4. x_{HI} Estimate

(1)	(2)	(3)	(4)
5.90	$5.50 \leq z \leq 6.39$	159	$0.17^{+0.23}_{-0.16}$
6.96	$6.54 \leq z \leq 7.49$	129	$0.63^{+0.18}_{-0.28}$
8.41	$7.51 \leq z \leq 9.43$	42	$0.79^{+0.13}_{-0.21}$
11.00	$9.62 \leq z \leq 14.18$	21	$0.88^{+0.11}_{-0.13}$

NOTE—(1): Mean redshift. (2) Redshift range. (3) Number of galaxies in a subsample. (4): Estimated x_{HI} value at each redshift. The mode and 68% HPDI are presented.

5.2. Cosmic Reionization History

Figure 11 shows our x_{HI} constraints at $z = 6-14$. Our high x_{HI} values suggest a late reionization. For comparison, we include x_{HI} estimates from the literature.

Our x_{HI} value at $z \sim 6$ is consistent with estimates from Ly α damping wing absorption of GRBs and QSOs, LAE clustering, Ly α luminosity function, and Ly α/β forests (e.g., Totani et al. 2014; Āurovčíková et al. 2024; Umeda et al. 2024b; Spina et al. 2024). At higher redshift ($z \sim 8-9$ and $10-14$), our x_{HI} values also agree with estimates from Ly α EW distributions and Ly α damping wing absorption of LBGs (e.g., Bruton et al. 2023; Curtis-Lake et al. 2023; Hsiao et al. 2024; Nakane et al. 2024; Tang et al. 2024a; Umeda et al. 2024a). Note that many of the galaxies used in these studies are included in our sample. At $z \sim 7$, numerous x_{HI} estimates exist, some of which are inconsistent with each other. Our moderately high neutral fraction at $z \sim 7$ ($x_{\text{HI}} = 0.63^{+0.18}_{-0.28}$) is consistent with many other measurements (e.g., Āurovčíková et al. 2024; Nakane et al. 2024; Tang et al. 2024a), with some studies showing even higher best-fit values (Wang et al. 2020: $x_{\text{HI}} = 0.70^{+0.20}_{-0.23}$ and Jones et al. 2024: $x_{\text{HI}} = 0.81^{+0.07}_{-0.10}$). However, our result is inconsistent with some estimates from Ly α luminosity functions (Morales et al. 2021: $x_{\text{HI}} = 0.28 \pm 0.05$ and Umeda et al. 2024b: $x_{\text{HI}} = 0.18^{+0.14}_{-0.12}$ at $z = 7.0$). Interestingly, Morales et al. (2021) and Umeda et al. 2024b both report high x_{HI} at $z = 7.3$ (Morales et al. 2021: $x_{\text{HI}} = 0.83^{+0.06}_{-0.07}$ and Umeda et al. 2024b: $x_{\text{HI}} = 0.75^{+0.09}_{-0.13}$), suggesting a very sharp reionization history from $z = 7.3$ to $z = 7.0$. These results share the late reionization feature found in our study, although the timing of the sharp progress differs slightly. This inconsistency might be attributed to differences in redshift binning. Note that our $z \sim 7$ bin has a width of $\Delta z \sim 1$, so galaxies at $z = 7.0$ and $z = 7.3$ are both included in the $z \sim 7$ bin.

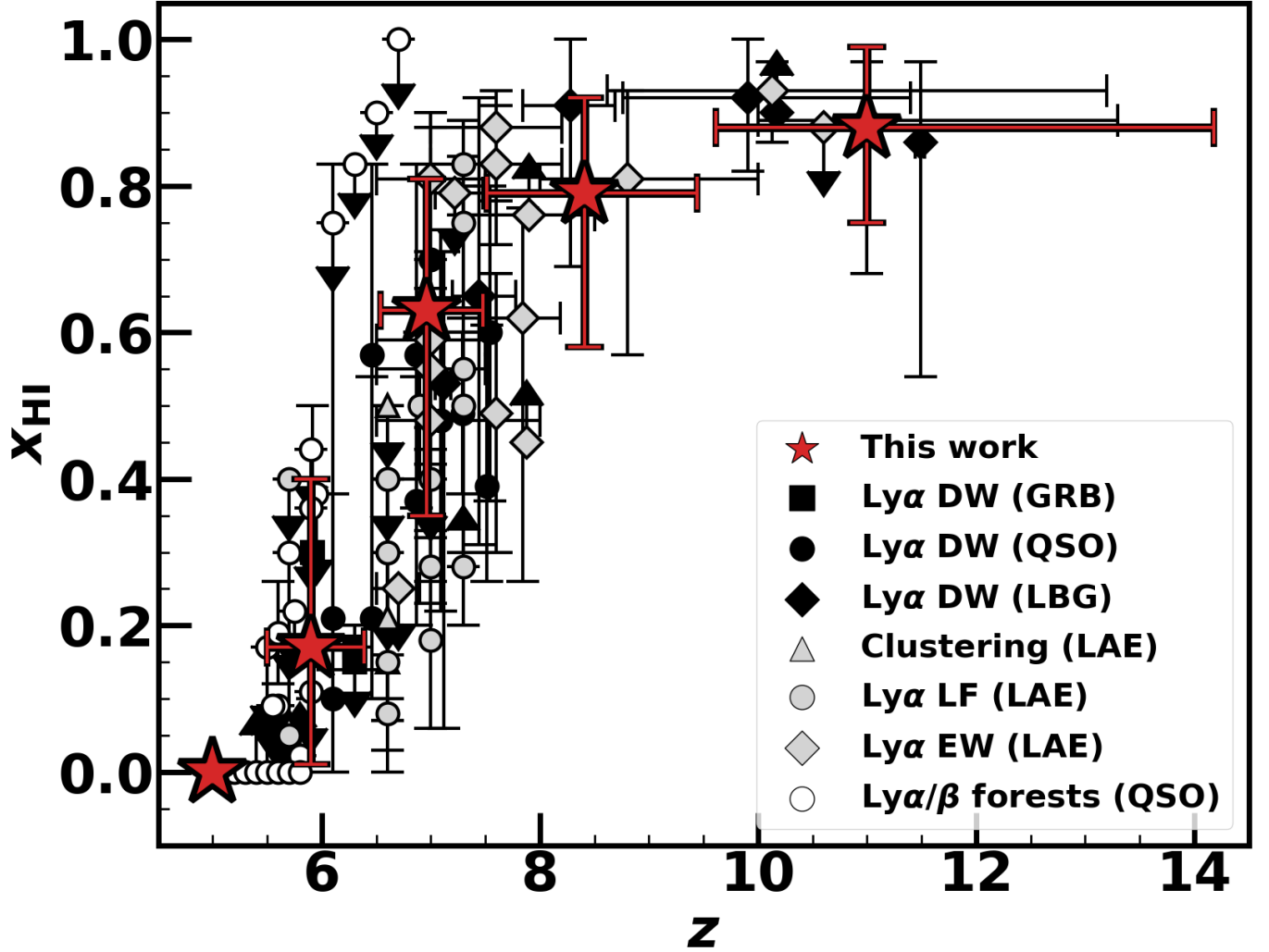


Figure 11. Redshift evolution of x_{HI} . The red stars at $z \gtrsim 6$ represent the x_{HI} values obtained in this work using Ly α EW distributions. At $z = 5$, x_{HI} is assumed to be zero in this study. We also present x_{HI} estimates from the literature using various methods: Ly α damping wing absorption of GRBs (black squares; Totani et al. 2006, 2014; Fausey et al. 2024), QSOs (black circles; Davies et al. 2018; Wang et al. 2020; Yang et al. 2020; Greig et al. 2022; Āurovčíková et al. 2024), and LBGs (black diamonds; Curtis-Lake et al. 2023; Hsiao et al. 2024; Umeda et al. 2024a); LAE clustering (gray triangles; Sobacchi & Mesinger 2015; Ouchi et al. 2018; Umeda et al. 2024b); Ly α luminosity function (gray circles; Ouchi et al. 2010; Konno et al. 2014, 2018; Zheng et al. 2017; Inoue et al. 2018; Morales et al. 2021; Goto et al. 2021; Ning et al. 2022; Umeda et al. 2024b); Ly α EW distribution (gray diamonds; Mason et al. 2018, 2019; Hoag et al. 2019; Jung et al. 2020; Whitler et al. 2020; Bolan et al. 2022; Bruton et al. 2023; Morishita et al. 2023; Nakane et al. 2024; Tang et al. 2024a; Jones et al. 2024); and Ly α forests and/or Ly α + β dark fraction/gaps (white circles; McGreer et al. 2015; Bosman et al. 2022; Zhu et al. 2022, 2024; Jin et al. 2023; Spina et al. 2024).

We compare our observational results to models of reionization history. We use 21cmFAST to generate reionization scenarios. We perform a total of nine simulations by varying two input parameters, ζ and $T_{\text{vir}}^{\text{min}}$, each in three different ways. The values of ζ are set to 20, 30, and 40, while $T_{\text{vir}}^{\text{min}}$ is set to 1×10^4 , 3×10^4 , and 5×10^4 K. Figure 12 represents these nine reionization scenarios. In all scenarios, the high observed x_{HI} values at $z \geq 7$ cannot be explained, or reionization does not complete by $z = 5.3$. When $\zeta = 40$, the ionizing ef-

iciency is too high, causing reionization to finish too early, which is inconsistent with the observational results. For $\zeta = 30$, increasing $T_{\text{vir}}^{\text{min}}$ brings the model closer to the observations at $z \geq 7$. However, it becomes inconsistent with the results of Bosman et al. (2022), which suggest that reionization is almost complete at $z = 5.3$ (i.e., $x_{\text{HI}} \sim 10^{-5}$). Similarly, for $\zeta = 20$, it becomes easier to explain late reionization at $z \geq 7$, but the value of x_{HI} remains too high at $z = 5.3$. Therefore, a very sharp reionization scenario (i.e., reionization pro-

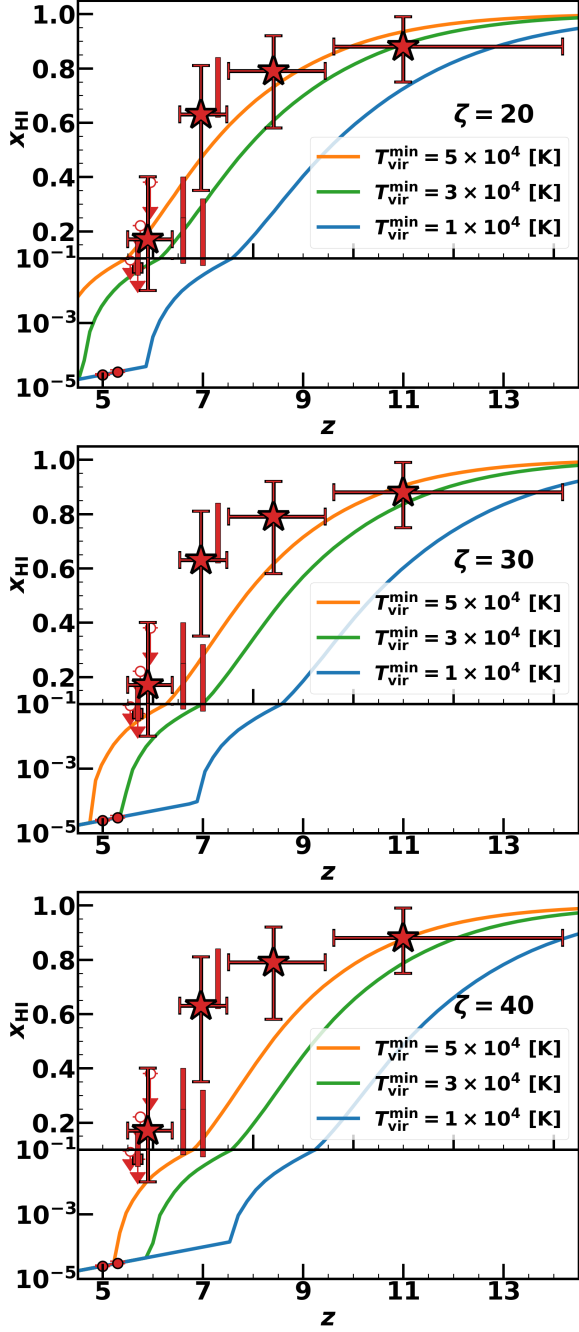


Figure 12. Models of cosmic reionization history. The curves show the results of nine 21cmFAST simulations with different combinations of ζ and $T_{\text{vir}}^{\text{min}}$. The red stars indicate the x_{HI} values derived in this work. The red rectangles, open circles, and red circles show observational constraints from Ly α luminosity function/angular correlation function (Umeda et al. 2024b), Ly α + β forest dark gaps (Zhu et al. 2022), and Ly α forest optical depth (Bosman et al. 2022), respectively. The observational results suggest a sharper reionization history than any of the nine models.

gresses rapidly around $z \sim 6 - 7$) is required to satisfy the high x_{HI} values observed at $z \geq 7$ while ensuring that reionization completes by $z = 5.3$. Note that the resolution of 21cmFAST does not provide sufficient accuracy to precisely determine the end of reionization (i.e., $x_{\text{HI}} \sim 10^{-5}$). Therefore, once the model reaches the extrapolation of the results by Bosman et al. (2022) at $z = 5.0 - 5.3$, the reionization history follows the extrapolated values in Figure 12. Although this section compares the observational results only with several models, we perform fitting to the observational data by treating ζ and $T_{\text{vir}}^{\text{min}}$ as free parameters in Section 6.2.

Note that we estimate x_{HI} assuming that the intrinsic Ly α EW distribution does not evolve with redshift. Some studies suggest that the intrinsic Ly α EW distribution shifts toward larger EWs at higher redshift (e.g., Naidu et al. 2022) due to the increasing fraction of young, metal-poor galaxies. If this is the case, an even later reionization history would be required to explain the decreasing trend of observed Ly α EWs.

5.3. Onset of Cosmic Reionization

Recently, a faint ($M_{\text{UV}} = -18.7$) LAE with a Ly α EW of 43 Å at $z = 13.0$, JADES-GS-z13-1-LA, was identified by Witstok et al. (2024). We include this object in our sample. We test whether the existence of such a strong LAE is consistent with our high x_{HI} value, $x_{\text{HI}} \sim 0.88$, at $z \sim 10 - 14$. To address this, we construct a Ly α EW distribution model at $z = 13.0$ with $x_{\text{HI}} = 0.88$ and $M_{\text{UV}} = -18.7$, following the methodology described in Section 4.3. In this model, the probability of observing a galaxy with EW > 43 Å is 5%. Given that our sample includes five galaxies with $M_{\text{UV}} \geq -18.7$ at $z = 10 - 14$, the existence of JADES-GS-z13-1-LA is naturally explained within our framework. Although our simulation does not fully resolve the complex morphology of ionized bubbles at the onset of reionization, Qin & Wythe (2024) have investigated the detectability of Ly α emission at $z = 13$ using more sophisticated simulations. Their results suggest that the probability of observing Ly α emission with EW > 40 Å is $\sim 10\%$. Thus, our high x_{HI} value at $z = 10 - 14$, based on Ly α emission from galaxies including JADES-GS-z13-1-LA, is self-consistent.

6. DISCUSSION

In this section, we interpret the late and sharp reionization history derived in Section 5. One possibility is the significant impact of recombination. Recent observations have reported that the mean free path of ionizing photons at $z \sim 6$ is relatively short (e.g., Becker et al. 2021; Gaikwad et al. 2023; Zhu et al. 2023; Davies et al.

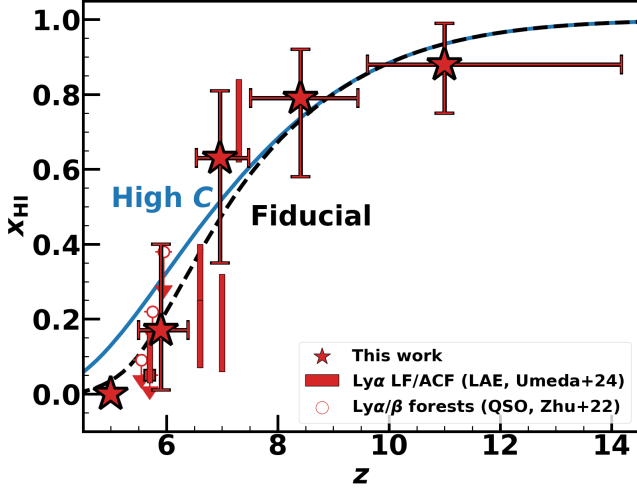


Figure 13. Reionization scenario assuming a high recombination rate. The blue solid line shows the reionization history with a short mean free path ($R_{\text{mfp}} = 6$ cMpc), which corresponds to a high clumping factor C . The black dashed line represents the history with fiducial parameters ($R_{\text{mfp}} = 15$ cMpc), which corresponds to a low clumping factor. The scenario with a short mean free path shows a more gradual x_{HI} evolution than the fiducial one.

2024b; Satyavolu et al. 2024). These findings may imply the existence of more small-scale structures in the IGM than accounted for in traditional reionization simulations, resulting in a high clumping factor ($C \sim 12$; Davies et al. 2024a). Under these conditions, the formation of large ionized bubbles may be hindered by recombination until the galaxy number density becomes sufficiently high at later epochs, potentially explaining the observed late reionization history. Another possible interpretation is that massive halos are the primary sources of reionization. Within the framework of hierarchical structure formation, late reionization can be explained by the delayed formation of massive halos, which emerge as the dominant contributors at later epochs (e.g., Naidu et al. 2020). In Section 6.1, we examine the role of strong recombination. In Section 6.2, we explore the scenario in which massive halos drive reionization. Section 6.3 summarizes our discussion.

6.1. Late Reionization by Strong Recombination

In this section, we focus on the impact of strong recombination. Observations of quasar spectra by Zhu et al. (2023) indicate that the mean free path of ionizing photons at $z = 5.93$ is ~ 0.8 pMpc, corresponding to a clumping factor of $C \sim 12$ (Davies et al. 2024a). To match this result, we set the mean free path in the 21cmFAST simulation to 6 cMpc, treating it as a redshift-independent parameter. We adopt the default values of $\zeta = 20$ and $T_{\text{vir}}^{\text{min}} = 5 \times 10^4$ K, which corresponds to a

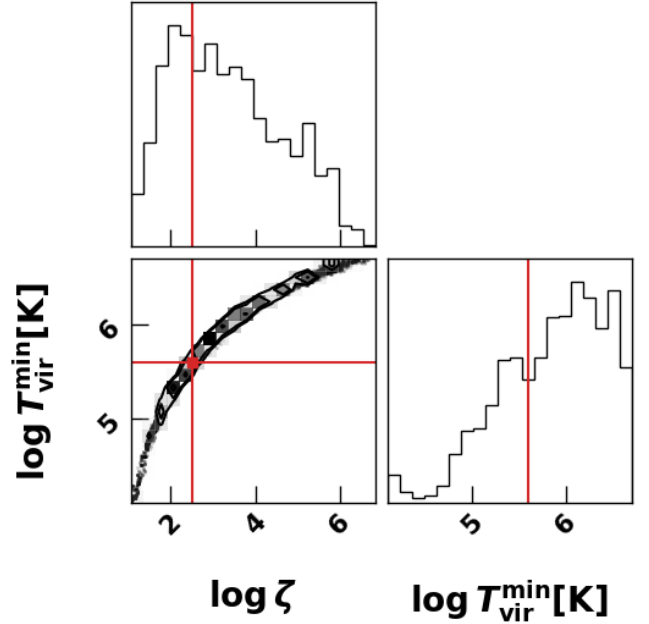


Figure 14. Posterior distributions of EoR parameters. The plot shows the ionizing efficiency ζ and the minimum virial temperature required for a halo to emit ionizing photons $T_{\text{vir}}^{\text{min}}$. The red lines indicate the best-fit values: $\log \zeta = 2.5$ and $\log T_{\text{vir}}^{\text{min}}/\text{K} = 5.6$. Such a high $T_{\text{vir}}^{\text{min}}$ corresponds to the minimum halo mass $M_h^{\text{min}} \sim 10^{10.5} M_{\odot}$ at $z \sim 6.5$.

limiting magnitude $M_{\text{UV}} = -10$ (Das et al. 2017; Greig & Mesinger 2017), in order to account for the contribution from faint galaxies ($M_{\text{UV}} \gtrsim -17$).

The blue solid and black dashed lines in Figure 13 represent the scenario with $R_{\text{mfp}} = 6$ cMpc and $R_{\text{mfp}} = 15$ cMpc, respectively. The scenario with a short mean free path (i.e., a high clumping factor) shows a more gradual decline in x_{HI} at $z \sim 6 - 7$ compared to the fiducial case ($R_{\text{mfp}} = 15$ cMpc), highlighting the difficulty of achieving a sharp reionization history when assuming a short mean free path. Qin et al. (2024) simulate the reionization history using the constraints from the CMB, UV luminosity functions, and forest data (without high- z LAE observations), and found a similar gradual evolution. Although a high clumping factor (or a short mean free path) naturally explains the residual neutral islands at $z \lesssim 6$, the sharp reionization history is difficult to explain with this effect.

6.2. Reionization Driven by Massive Halos

To explain the x_{HI} measurements indicating a late and sharp reionization history, we fit observational constraints on x_{HI} , including our results, to reionization scenarios generated with 21cmFAST. We treat the ionizing efficiency ζ and the minimum virial temperature $T_{\text{vir}}^{\text{min}}$ as free parameters (see Section 4.2). Each 21cmFAST

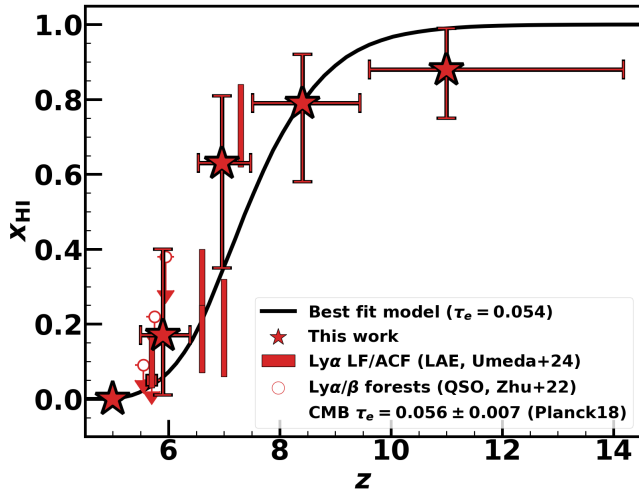


Figure 15. Cosmic reionization history: observational constraints and best-fit model. The black line represents the best-fit reionization scenario obtained from the parameter fitting procedure. The red stars indicate the x_{HI} values derived in this work. The red rectangles and open circles show observational constraints from Ly α luminosity function/angular correlation function (Umeda et al. 2024b) and Ly $\alpha + \beta$ forest dark gaps (Zhu et al. 2022), respectively, which are used for the fitting procedure. The best-fit scenario reproduces the observed x_{HI} values and the CMB optical depth, supporting a late and sharp reionization.

simulation run with these two EoR parameters provides a redshift evolution of x_{HI} , which we compare with observational results to estimate the best-fit parameters. A high $T_{\text{vir}}^{\text{min}}$ corresponds to reionization dominated by massive halos, as it sets the minimum halo mass capable of emitting ionizing photons. Since 21cmFAST can incorporate inhomogeneous reionization processes, we use observational results reflecting such processes for our fitting. Specifically, the following constraints are applied:

- Ly α EW distributions observed by JWST (this work)
- Ly α luminosity functions and angular correlation functions observed by Subaru (Umeda et al. 2024b)
- Ly α and Ly β forest dark gaps of QSOs observed by Keck and VLT (Zhu et al. 2022)
- Optical depth of CMB observed by Planck ($\tau_e = 0.0561 \pm 0.0071$; Planck Collaboration et al. 2020).

We calculate the optical depth of the CMB using Equation (17). We adopt flat priors of $-\infty < \log \zeta < \infty$ and $4.0 < \log T_{\text{vir}}^{\text{min}}/\text{K} < 6.7$. The lower limit of the prior, $\log T_{\text{vir}}^{\text{min}} = 4.0$, corresponds to the threshold for efficient atomic cooling (Barkana & Loeb 2001), while the upper limit, $\log T_{\text{vir}}^{\text{min}} = 6.7$, corresponds to a minimum halo mass of $10^{12} M_{\odot}$.

In Figure 14, we present the posterior distributions of ζ and $T_{\text{vir}}^{\text{min}}$. Despite a strong degeneracy between these two parameters, we derive $\log \zeta = 2.50_{-0.96}^{+1.61}$ and $\log T_{\text{vir}}^{\text{min}}/\text{K} = 5.61_{-0.05}^{+1.01}$. Figure 15 shows the reionization history derived from the best-fit EoR parameters, which successfully reproduces the measured x_{HI} values. At $z \sim 7$, the best-fit scenario lies between the constraints of this study and those from Umeda et al. (2024b). Additionally, the optical depth of the corresponding reionization scenario, $\tau_e = 0.054$, agrees with the Planck result.

Note that our x_{HI} values are derived through comparison with a simulation using $\zeta = 20$ and $T_{\text{vir}}^{\text{min}} = 5 \times 10^4 \text{ K}$, which are inconsistent with the obtained best-fit parameters. To address this discrepancy, we run a simulation with the best-fit parameters and re-estimate the x_{HI} values. The recalculated x_{HI} values are < 0.41 , $0.70_{-0.32}^{+0.20}$, $0.86_{-0.18}^{+0.12}$, and $0.89_{-0.13}^{+0.11}$ at $z \sim 6, 7, 8 - 9$, and $10 - 14$, respectively. These values are consistent with those derived in Section 5.1 within errors. Therefore, we confirm that the selection of input parameters does not significantly affect the estimation of x_{HI} values, and that our x_{HI} values and the best-fit reionization history are self-consistent.

From Equation (16), the best-fit value of the minimum virial temperature, $T_{\text{vir}}^{\text{min}} = 10^{5.6} \text{ K}$, corresponds to a minimum halo mass of $M_h^{\text{min}} = 10^{10.5} M_{\odot}$ at $z = 6.5$. This implies that only halos more massive than $10^{10.5} M_{\odot}$ are capable of emitting ionizing photons beyond their boundaries. Using Equation (14), the UV magnitude of the faintest ionizing sources is estimated to be $M_{\text{UV}} = -17$. Since our galaxy sample at $z \sim 6.5$ includes galaxies with $M_{\text{UV}} > -17$, this threshold luminosity is brighter than our current observational limit. Previous studies often assumed that all star-forming galaxies contribute to ionizing photon escape and that the minimum halo mass for ionizing photon emission is the same as the minimum halo mass required for star formation through efficient cooling. For instance, Ishigaki et al. (2018) derive a lower limit for the threshold UV magnitude of $M_{\text{UV}} > -14.0$ under this assumption. However, our brighter threshold value of $M_{\text{UV}} = -17$ suggests that the minimum mass for ionizing sources is larger than the one for galaxy-hosting halos. This implies that the faintest galaxies do not significantly contribute to ionizing photon escape.

We then consider the implications of $\zeta \sim 10^{2.5}$. In the following discussion, we consider two types of ionizing sources: star-forming galaxies and active galactic nuclei (AGNs). First, assuming that star-forming galaxies are the dominant sources, we connect ζ to the ionizing photon production efficiency ξ_{ion} , which is defined as the

ratio of the ionizing photon emission rate to the UV luminosity, and the escape fraction of ionizing photons, f_{esc} . By multiplying the number of baryons and differentiating Equation (15) with respect to the look-back time t , we derive the following equation:

$$\zeta \frac{dM_h}{dt} \frac{\Omega_b X_p}{\Omega_m m_p} = f_{\text{esc}} \xi_{\text{ion}} L_{\text{UV}}, \quad (24)$$

where M_h is the halo mass, m_p is the proton mass, and L_{UV} is the UV luminosity of a galaxy residing in a halo with mass M_h . Hereafter, we focus on ξ_{ion} and f_{esc} at $z \sim 6.5$, although this method can also be applied to other redshifts. We adopt the mean halo mass growth rate derived by [Fakhouri et al. \(2010\)](#):

$$\left\langle \frac{dM_h}{dt} \right\rangle = 46.1 M_{\odot} \text{ yr}^{-1} \left(\frac{M_h}{10^{12} M_{\odot}} \right)^{1.1} \times (1 + 1.11z) \sqrt{\Omega_m (1+z)^3 + \Omega_{\Lambda}}. \quad (25)$$

Using the halo mass-UV magnitude relation from Equation (14), both M_h and L_{UV} can be expressed as functions of M_{UV} . From observations, [Simmonds et al. \(2024\)](#) derive $\xi_{\text{ion},0}$, which is the ionizing photon production efficiency under the assumption of an escape fraction of zero, as a function of UV magnitude for $6 < z \leq 7$:

$$\log \xi_{\text{ion},0} [\text{Hz erg}^{-1}] = -0.03 M_{\text{UV}} + 24.88. \quad (26)$$

The relationship between ξ_{ion} and $\xi_{\text{ion},0}$ is given by:

$$\xi_{\text{ion},0} = (1 - f_{\text{esc}}) \xi_{\text{ion}}. \quad (27)$$

Substituting this into Equation (24) gives the following expression for f_{esc} :

$$f_{\text{esc}} = \frac{1}{1 + \frac{\xi_{\text{ion},0} L_{\text{UV}} \Omega_m m_p}{\zeta (dM_h/dt) \Omega_b X_p}}. \quad (28)$$

In the top panel of Figure 16, we show f_{esc} at $z \sim 6.5$ as a function of M_{UV} . The blue solid line and the shaded region correspond to the best-fit and 1σ uncertainty of the posterior distribution of ζ in Figure 14. The large ζ value obtained in this work implies a high escape fraction of $f_{\text{esc}} \sim 50\%$. In contrast, [Chisholm et al. \(2022\)](#) derive the relation between f_{esc} and the UV spectral slope β from the Low-redshift Lyman Continuum Survey (LzLCS) and literature observations at $z \sim 0$. They infer f_{esc} at $z \sim 6$, shown as the black solid line in the top panel of Figure 16, from the relation. The f_{esc} derived from these local galaxy observations is approximately 10%, significantly lower than the value estimated in this work. [Harikane et al. \(2020\)](#) directly derive an upper limit of the escape fraction at $z \sim 6$, $f_{\text{esc}} < 0.15 \pm 0.16$,

through interstellar absorption lines in the composite spectrum of $z \sim 6$ galaxies with $M_{\text{UV}} \sim -23$, which is also lower than our estimate. These discrepancies suggest that the late and sharp reionization history derived in this work cannot be explained by star-forming galaxies without assuming an implausibly sharp redshift evolution in galaxy properties. In the bottom panel of Figure 16, we plot ξ_{ion} calculated using f_{esc} from the top panel and $\xi_{\text{ion},0}$ derived by [Simmonds et al. \(2024\)](#). Our ξ_{ion} values are ~ 0.3 dex higher than $\xi_{\text{ion},0}$ because the effect of the high f_{esc} is non-negligible in Equation (27).

We compare our results to one of the most sophisticated and precise reionization simulations, THESAN. The THESAN simulations ([Kannan et al. 2022](#); [Garaldi et al. 2022](#); [Smith et al. 2022](#)) include several runs, and our x_{HI} values align with the sharpest scenario: THESAN-HIGH-2. In this simulation, only massive halos ($> 10^{10} M_{\odot}$) contribute to reionization, and their escape fraction is $f_{\text{esc}} = 0.80$. Therefore, the high $T_{\text{vir}}^{\text{min}}$ and f_{esc} values derived with 21cmFAST above are consistent with the THESAN simulations. Explaining our late and sharp reionization remains challenging unless an extremely high f_{esc} is assumed.

We note that recent observations report that the cosmic star formation rate at $z \gtrsim 10$ is higher than model predictions assuming constant star formation efficiencies (e.g., [Harikane et al. 2024a](#)). This suggests that the number of bright galaxies is larger than predicted by Equation (14) used in this work, highlighting the challenge of reproducing our late reionization history.

Second, we assume that AGNs are the primary reionization sources, rather than star-forming galaxies. In this case, the time derivative of Equation (15) is expressed as:

$$\zeta \frac{dM_h}{dt} \frac{\Omega_b X_p}{\Omega_m m_p} = f_{\text{AGN}} f_{\text{esc}} \dot{n}, \quad (29)$$

where f_{AGN} represents the fraction of halos with mass M_h hosting AGNs at redshift z , and \dot{n} is the ionizing photon emission rate of AGNs. A high f_{AGN} value implies a large AGN duty cycle. In the following discussion, we connect f_{AGN} to the best-fit ζ value. To link halo mass with AGN UV magnitude, we use the AGN UV flux ratio $f_{\text{UV,AGN}}$ obtained by [Zhang et al. \(2021\)](#), which quantifies the contribution of AGN UV flux to the total UV flux (including the host galaxy):

$$\log f_{\text{UV,AGN}} = -0.118 M_{\text{UV}} - 3.056, \quad (30)$$

where M_{UV} is the AGN+host galaxy UV magnitude. Using this relation, the AGN UV luminosity can be determined as a function of the host galaxy's UV luminos-

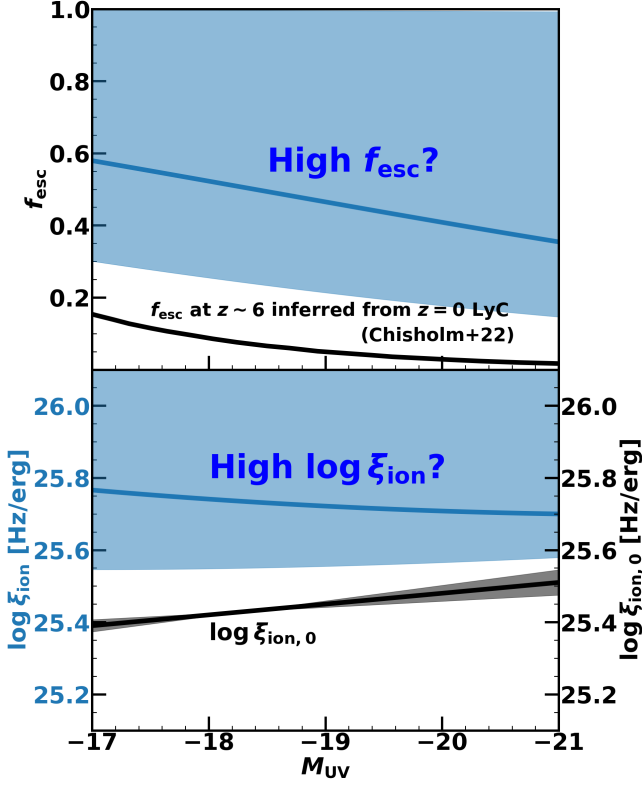


Figure 16. Lyman continuum escape fraction f_{esc} (top) and ionizing photon production efficiency ξ_{ion} (bottom) of star-forming galaxies at $z \sim 6.5$, as a function of UV magnitude. The blue lines indicate f_{esc} and ξ_{ion} obtained in this work. The blue shaded regions represent the 1σ errors. These quantities are derived based on the ζ values in Figure 14 and the ionizing photon production efficiency assuming an escape fraction of zero, $\xi_{\text{ion},0}$, obtained by Simmonds et al. (2024). The black line in the bottom panel shows $\xi_{\text{ion},0}$ obtained by Simmonds et al. (2024). Our ξ_{ion} values are higher than $\xi_{\text{ion},0}$ because the effect of the high f_{esc} is non-negligible in Equation (27). The black line in the top panel shows f_{esc} at $z = 6$, which is inferred from the Low-redshift Lyman Continuum Survey (LzLCS) (Chisholm et al. 2022). The f_{esc} estimated from the reionization history in this work and LzLCS in Chisholm et al. (2022) exhibit a clear tension.

ity. Assuming that the host galaxy’s UV luminosity follows Equation (14), we derive the AGN UV luminosity as a function of halo mass. We model the spectral energy distribution (SED) of AGN as a power law ($f_\nu \propto \nu^\alpha$) with an index of $\alpha = -0.61$ for $\lambda > 912 \text{ \AA}$ and $\alpha = -1.7$ for $\lambda \leq 912 \text{ \AA}$ (Lusso et al. 2015). This allows us to calculate \dot{n} for a given AGN UV luminosity.

We estimate f_{AGN} for three cases: $f_{\text{esc}} = 50\%$, 75% , and 100% (Figure 17). Even with an escape fraction of 100% , the estimated f_{AGN} at $M_{\text{UV}} \gtrsim -19$ exceeds 100% , indicating that faint AGNs are unlikely to contribute ionizing photons at the efficiency of $\zeta \sim 10^{2.5}$. For comparison, we also calculate f_{AGN} using the ratio

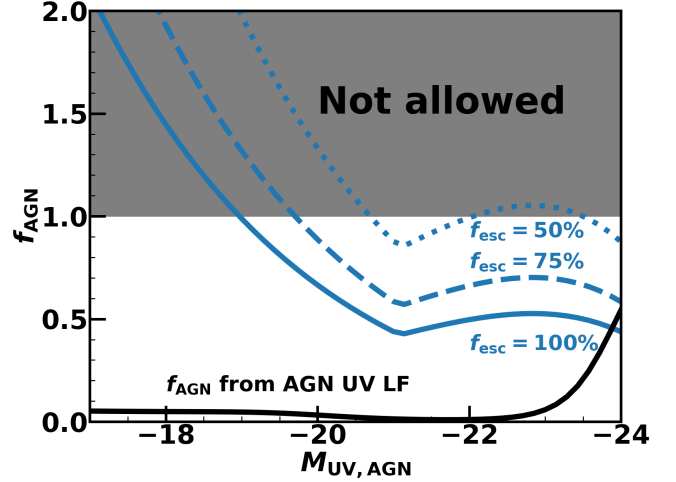


Figure 17. AGN fraction f_{AGN} as a function of AGN UV magnitude without the contribution from the host galaxy, at $z \sim 6.5$. f_{AGN} represents the fraction of halos with mass M_h hosting AGNs. The blue dotted, dashed, and solid lines correspond to f_{AGN} values derived in this work assuming $\zeta = 10^{2.5}$ and escape fractions $f_{\text{esc}} = 50\%$, 75% , and 100% , respectively. The gray shaded region indicates unphysical values where $f_{\text{AGN}} > 1$. The black solid line shows f_{AGN} values derived from the ratio of the galaxy and AGN UV luminosity functions at $z \sim 6$. Across most of the UV magnitude range, our f_{AGN} values significantly exceed those inferred from luminosity functions.

of the galaxy UV luminosity function (Bouwens et al. 2021) to the AGN UV luminosity function at $z \sim 6$. The black solid line in Figure 17 shows f_{AGN} derived from the galaxy and AGN UV luminosity functions. The AGN luminosity function at $z \sim 6$ combines bright AGNs (Matsuoka et al. 2018) and faint AGNs (Harikane et al. 2023). Our f_{AGN} values, derived under the assumption of high ionizing efficiency ($\zeta \sim 10^{2.5}$), are significantly higher than those derived from luminosity functions. Note that we derive f_{AGN} assuming ζ as a constant parameter. If ζ is larger for brighter AGNs, the problem that f_{AGN} exceeds 100% for faint AGNs may be solved. However, Solving the tension with f_{AGN} derived from luminosity functions is difficult because our f_{AGN} values are higher than those derived from luminosity functions across most of the UV magnitude range.

6.3. Possible Explanations

In Section 6.1 and 6.2, we demonstrate that neither star-forming galaxies in massive halos, AGNs in massive halos, nor strong recombination cannot fully account for the late and sharp reionization history derived in this work. In this subsection, we discuss several potential solutions to address the discrepancy.

First, the escape fraction of star-forming galaxies during the EoR may be indeed as high as $f_{\text{esc}} \sim 50\%$, as

suggested in Figure 16. Although this value is inconsistent with predictions based on observations of local galaxies (Chisholm et al. 2022), galaxy properties can evolve with redshift. For instance, Naidu et al. (2022) show that approximately half of LAEs at $z \sim 2$ exhibit $f_{\text{esc}} \sim 50\%$. This may result from ionizing photons produced by massive and young stars escaping feedback-induced holes in the ISM. While such LAEs constitute only a small fraction of galaxies at $z \sim 2$, the late and sharp reionization history could be explained if these galaxies dominate the universe during the EoR. See also Naidu et al. (2020) and Matthee et al. (2022) for reionization models dominated by bright galaxies or LAEs.

Second, the duty cycle of faint AGNs may be significantly larger than currently understood. Although JWST observations have identified numerous faint broad-line AGNs, the number density could be even larger when narrow-line type 2 AGNs are included (e.g., Scholtz et al. 2023). Ionizing photons emitted by these faint type 2 AGNs could address the reionization challenge. Asthana et al. (2024) and Madau et al. (2024) also propose late and sharp reionization scenarios where faint AGNs dominate (or partially contribute to) the photon budget, although our ζ value exceeds theirs.

Third, f_{esc} might evolve with redshift. If f_{esc} increases toward lower redshift, the late and sharp reionization can be explained. For example, Yajima et al. (2014) investigate the redshift evolution of f_{esc} with simulations and show a mild increase from $z \sim 10$ to $z \sim 7$, attributed to the lower gas density in galaxies at lower redshift. Another possibility is that external UV radiation ionizes the outer layers of dwarf galaxies at lower redshift, potentially resulting in a higher f_{esc} .

Fourth, our $x_{\text{H I}}$ values may be biased. To derive models of EW distributions, we assume that the peak velocity of Ly α emission follows a log-normal distribution, with its peak given by Equation (20). This probability distribution depends solely on M_h . However, it is possible that the peak velocity also evolves with redshift. The velocity offset of Ly α emission originates from interactions with galactic outflows. Therefore, the offset could be smaller at higher redshifts if outflows are weaker. In such a scenario, Ly α photons would experience stronger absorption at higher redshifts. Consequently, the observed evolution of Ly α emission could be explained without adopting high $x_{\text{H I}}$ values.

Lastly, alternative sources beyond star-forming galaxies and AGNs may significantly contribute to reionization and produce a late and sharp reionization history. Potential contributors include globular clusters with $f_{\text{esc}} \sim 1$ (e.g., Ricotti 2002), high-mass X-ray binaries (e.g., Jeon et al. 2014), and primordial black holes

(e.g., Ricotti et al. 2008; Tashiro & Sugiyama 2013; Clark et al. 2018). The late and sharp reionization could be explained if these sources efficiently produce ionizing photons at $z \sim 6 - 8$.

7. SUMMARY

In this paper, we present our constraints on $x_{\text{H I}}$ from Ly α EWs of galaxies at $z \sim 5 - 14$. We select 586 galaxies at $z = 4.5 - 14.2$ observed by multiple JWST/NIRSpec spectroscopy projects, JADES, GLASS, CEERS, and GO/DDT programs. The redshifts of galaxies in our sample are determined with emission lines and/or a strong continuum break. We fit the galaxy spectra near rest-frame 1216 Å to obtain Ly α EW measurements or upper limits for all these galaxies. Our major findings are summarized below:

1. We find that the fraction of LAEs with $\text{EW} > 25 \text{ \AA}$ (10 \AA) decreases from $22_{-4}^{+5}\%$ ($29_{-4}^{+7}\%$) at $z \sim 5$ to $< 10\%$ ($10_{-8}^{+13}\%$) at $z \sim 10 - 14$ for $-20.25 < M_{\text{UV}} < -18.75$ galaxies, suggesting increasing Ly α damping wing absorption at higher redshift. The Ly α fractions obtained in this work are consistent with past JWST measurements. The decreasing trend of Ly α fraction is more clearly seen for fainter ($-18.75 < M_{\text{UV}} < -17.25$) galaxies, likely due to the smaller ionized bubble radius around faint galaxies.
2. We derive the Ly α escape fraction $f_{\text{esc}}^{\text{Ly}\alpha}$. We find that $f_{\text{esc}}^{\text{Ly}\alpha}$ decreases with redshift and increases with Ly α EW, suggesting increasing Ly α damping wing absorption at higher redshift. We also find $f_{\text{esc}}^{\text{Ly}\alpha}$ values are low for galaxies with a red UV spectrum (β) and high ionizing photon production efficiency assuming zero LyC escape ($\xi_{\text{ion},0}$), which can be explained by a thick gaseous disc.
3. We derive Ly α luminosity functions at $z = 5 - 14$ with the observed Ly α EW distributions and galaxy UV luminosity functions. We find the Ly α luminosity function at $L_{\text{Ly}\alpha} = 10^{42} - 10^{43} \text{ erg s}^{-1}$ decreases by ~ 3 dex from $z \sim 5$ to $z \sim 10 - 14$.
4. To obtain EW distribution models during the EoR, We use the EW distribution at $z \sim 5$ as the intrinsic Ly α EW distribution and model Ly α absorption in the IGM at $z \gtrsim 6$ calculated with 21cmFAST semi-numerical simulations that reproduce the observed UV luminosity function during the EoR and the CMB optical depth. We obtain $x_{\text{H I}} = 0.17_{-0.16}^{+0.23}$, $0.63_{-0.28}^{+0.18}$, $0.79_{-0.21}^{+0.13}$, and $0.88_{-0.13}^{+0.11}$ at $z \sim 6, 7, 8 - 9$, and $10 - 14$, respectively, via the comparisons of the observed EW

distributions with the models. Our high $x_{\text{H I}}$ values at $z \sim 7 - 14$ suggest a very late and sharp reionization.

5. Assuming star-forming galaxies or AGNs as major ionizing sources, the late and sharp reionization history obtained in this study is explained with massive halos ($M_h > 10^{10.5} M_\odot$) as the main ionizing sources. However, an extremely high escape fraction $f_{\text{esc}} \sim 50\%$ and ionizing photon production efficiency (large duty cycle) are required for galaxies (AGNs) at the same time. We also confirm that a high recombination rate cannot explain our $x_{\text{H I}}$ measurements. Therefore, a redshift evolution of the escape fraction, a high number density of obscured AGNs, or alternative ionizing sources may be needed.

ACKNOWLEDGEMENTS

We thank Sarah Bosman, Akio Inoue, Laura Keating, Charlotte Mason, Kana Moriwaki, Hyunbae Park, Hayato Shimabukuro, and Daniel Stark for valuable discussions on this work. We thank Yuki Isobe for providing us with the table of the line spread function of the NIRpec instrument. We thank Hiroto Yanagisawa for providing us with the table of the UV slope measurements. This work is based on observations made with the NASA/ESA/CSA James Webb Space Telescope. The data were obtained from the Mikulski Archive for Space Telescopes at the Space Telescope Science Institute, which is operated by the Association of Univer-

sities for Research in Astronomy, Inc., under NASA contract NAS 5-03127 for JWST. These observations are associated with programs GTO 1180/1181 (JADES; PI: D. Eisenstein), GTO 1210/1286 (JADES; PI: N. Lützgendorf), GO 3215 (JADES; PI: D. Eisenstein & R. Maiolino), ERS 1324 (GLASS; PI: T. Treu), ERS 1345 (CEERS; PI: S. Finkelstein), GO 1433 (PI: D. Coe), and DDT 2750 (PI: P. Arrabal Haro). The authors acknowledge the teams conducting these observations for developing their observation programs. We thank the JADES team for publicly releasing reduced spectra and catalogs from the JADES survey. This publication is based on work supported by the World Premier International Research Center Initiative (WPI Initiative), MEXT, Japan, KAKENHI (21H04489, 24H00245, 24K00625, 24K17098) through the Japan Society for the Promotion of Science, and JST FOREST Program (JPMJFR202Z). This work was supported by the joint research program of the Institute for Cosmic Ray Research (ICRR), the University of Tokyo. This research was supported by FoPM, WINGS Program, the University of Tokyo.

Software: 21cmFAST (Mesinger et al. 2011; Murray et al. 2020), Astropy (Astropy Collaboration et al. 2013, 2018, 2022), corner (Foreman-Mackey 2016), emcee (Foreman-Mackey et al. 2013), matplotlib (Hunter 2007), NumPy (Harris et al. 2020), PyNeb (Luridiana et al. 2015), scikit-learn (Pedregosa et al. 2011), and SciPy (Virtanen et al. 2020).

APPENDIX

A. SAMPLE IN THIS STUDY



Figure A1. Spectra of the galaxies in our sample. The black solid lines and shaded regions represent the observed spectra and associated 1σ errors, respectively. The vertical dashed lines represent the rest-frame Ly α wavelength. The yellow regions indicate the detected Ly α lines.

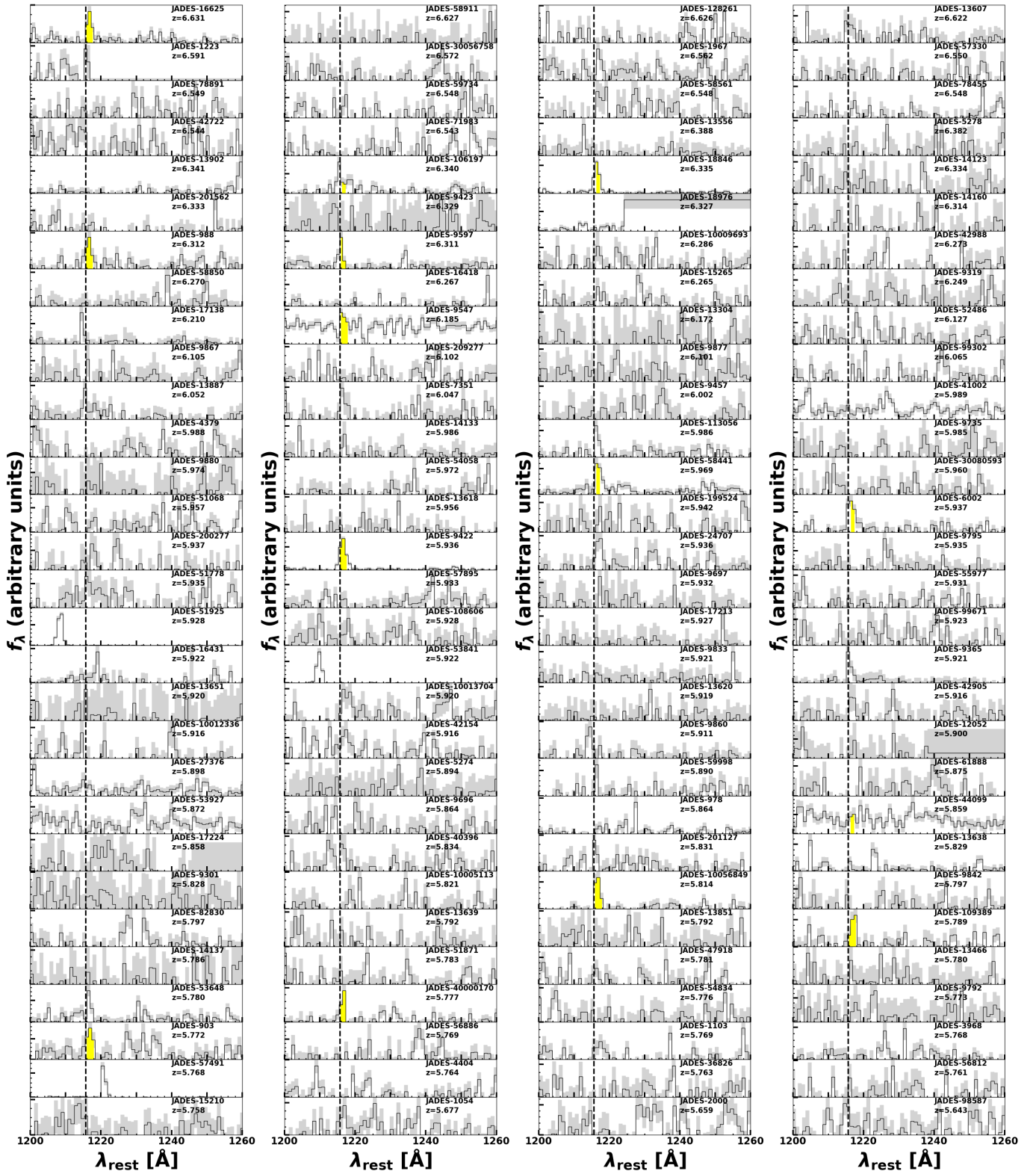


Figure A1. Continued.

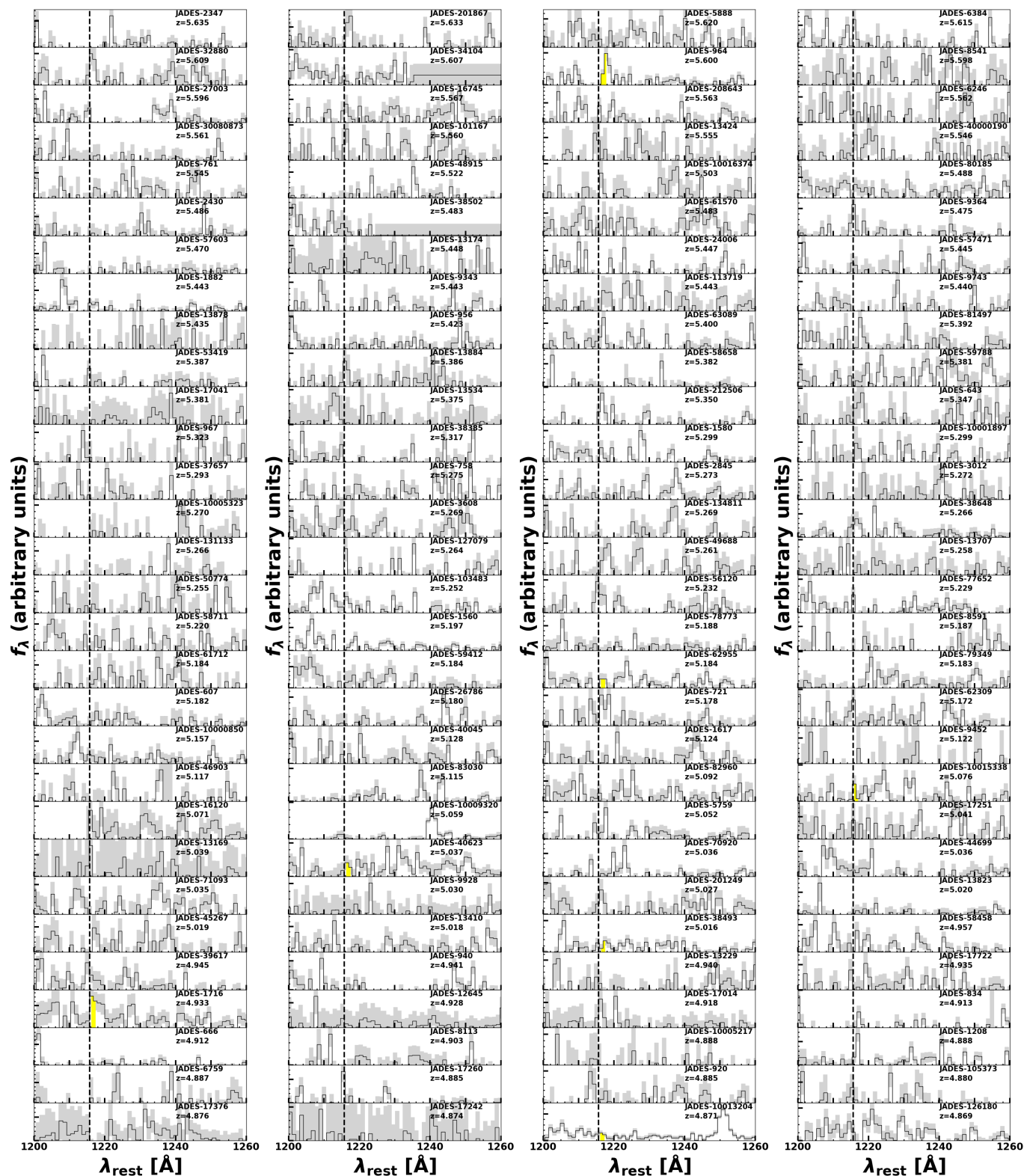


Figure A1. Continued.

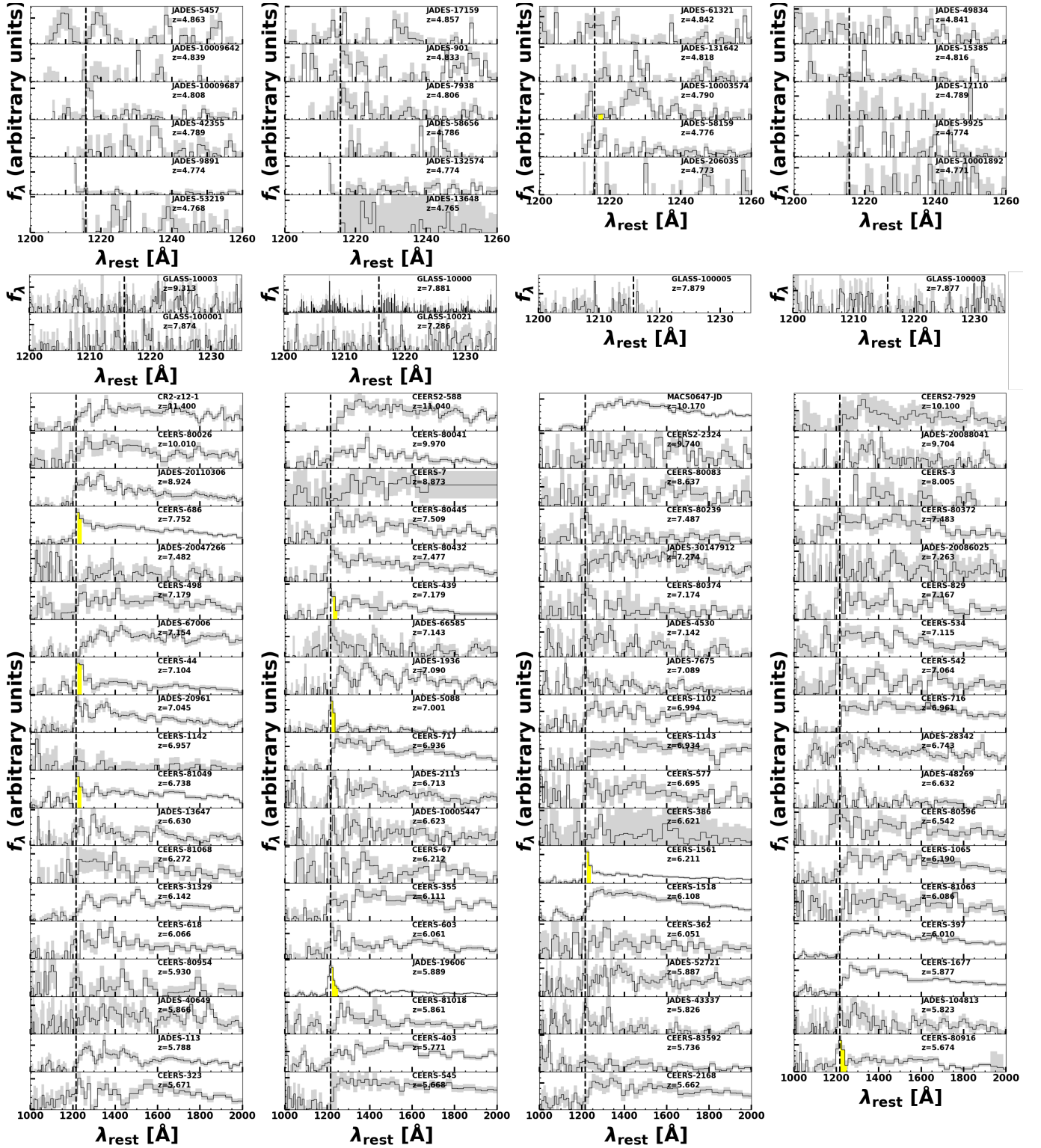


Figure A1. Continued.

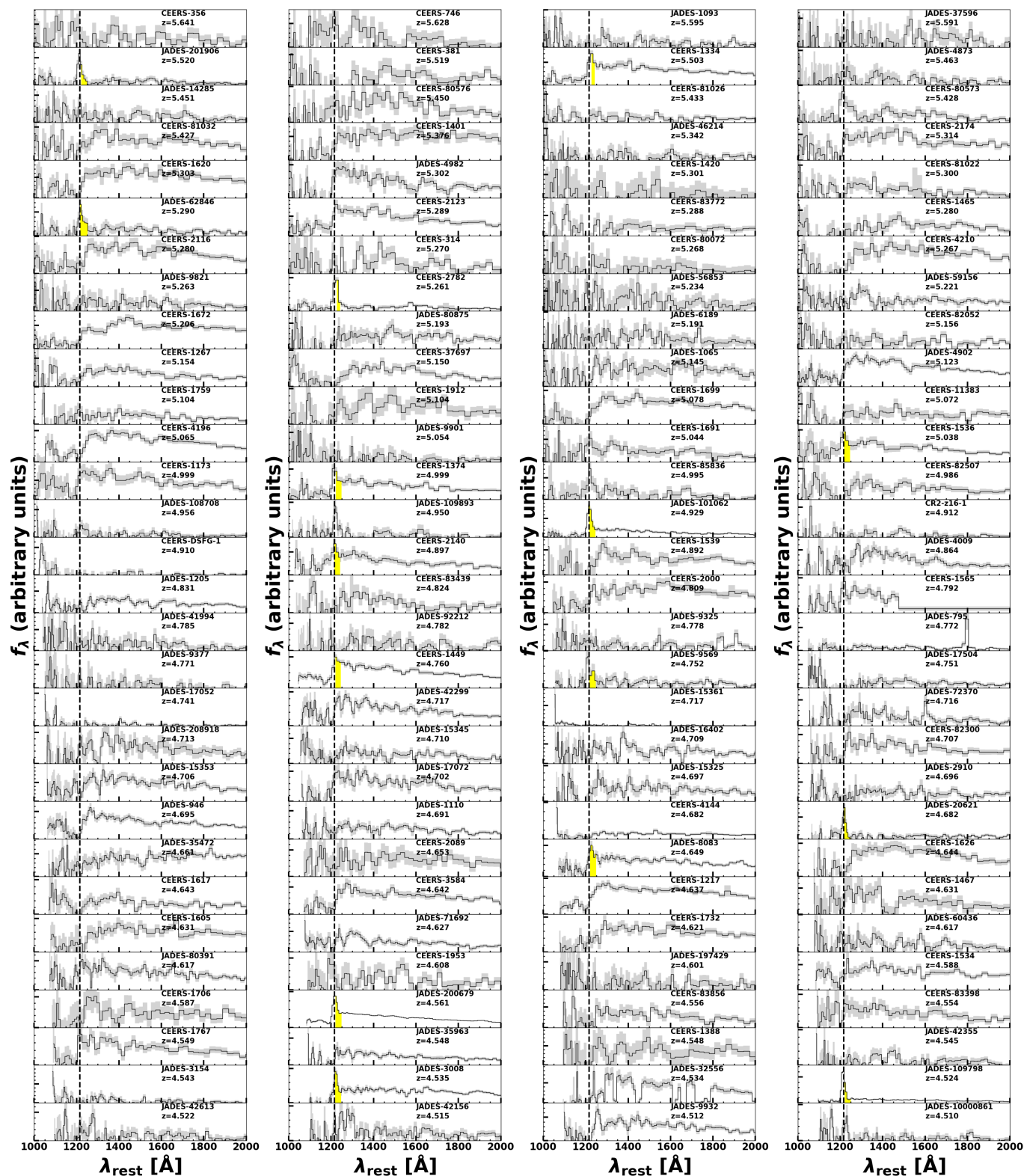


Figure A1. Continued.

Table A1. Sample in this study

ID	R.A. (deg)	Decl. (deg)	z_{sys}	M_{UV} (mag)	$F_{\text{Ly}\alpha}$ ($10^{-19} \text{ erg s}^{-1} \text{ cm}^{-2}$)	$\Delta v_{\text{Ly}\alpha}$ (km s^{-1})	$f_{\text{esc}}^{\text{Ly}\alpha}$	$\text{EW}_{\text{Ly}\alpha}$ (\AA , This work)	$\text{EW}_{\text{Ly}\alpha}$ (\AA , Tang24)	$\text{EW}_{\text{Ly}\alpha}$ (\AA , Jones24)	PID
(1)	(2)	(3)	(4)	(5)	(6)	(7)	(8)	(9)	(10)	(11)	(12)
JADES-GS-z14-0	53.08294	-27.85563	14.180 ^a	-20.81 ^b				< 5 ^b			1287
JADES-GS-z14-1	53.07427	-27.88592	13.90 ^b	-19.0 ^b				< 10 ^b			1287
JADES-17400	53.14988	-27.77650	13.200	-18.99	< 10			< 16	< 45		1210
JADES-GS-z13-1-LA	53.06475	-27.89024	13.01 ^c	-18.66 ^c		696 \pm 299 ^c	0.06 \pm 0.02 ^c	43 \pm 13 ^c	< 103	< 242	1287
JADES-2773	53.16634	-27.82156	12.630	-18.14	< 2			< 11			1210
JADES-10014220	53.16477	-27.77463	11.668	-19.30	< 4			< 24	< 45		1210
CR2-z12-1	214.94317	52.94244	11.400	-19.76	< 4			< 8	< 26		2750
CEERS2-588	214.90662	52.94550	11.040	-19.77	< 3			< 4	< 38		2750
JADES-5591	189.10604	62.24204	10.604	-21.54	19 \pm 7	334 \pm 110	0.06 \pm 0.02	7 \pm 1	12 \pm 2	7 \pm 1	1181
JADES-20030133	53.16594	-27.83424	10.563	-19.70	< 5			< 9			1286
JADES-10014177	53.15884	-27.77349	10.409	-18.54	< 12			< 14	< 35		1210
MACS0647-JD	101.97133	70.23972	10.170	-20.3 ^d	< 6			< 67	< 31		1433
CEERS2-7929	214.92279	52.91153	10.100	-19.06	< 18			< 125	< 30		2750
CEERS-80026	214.81183	52.73711	10.010	-20.29	< 14			< 21	< 10		1345
CEERS-80041	214.73254	52.75808	9.970	-20.24	< 10			< 477	< 14		1345
JADES-55757	189.21769	62.19949	9.746	-19.69	< 16		< 0.11	< 21	< 31		1181
JADES-80088	189.23911	62.21094	9.744	-19.28	< 3			< 13	< 84		1181
CEERS2-2324	214.86158	52.90461	9.740	-18.68	< 6			< 7			2750
JADES-20088041	53.17552	-27.78064	9.704	-19.29	< 6			< 62	< 10		1286
JADES-6438	53.16735	-27.80750	9.686	-19.28	< 9			< 46	< 79		1210
JADES-59720	189.23980	62.21083	9.617	-19.34	< 23			< 26			1181
JADES-265801	53.11244	-27.77463	9.433	-20.37	< 3			< 2	< 3		3215
GLASS-10003	3.61725	-30.42556	9.313	-21.60 ^d	< 3			< 1	< 5		1324
JADES-19715	189.13833	62.28987	9.305	-19.98	< 35			< 31	< 49	34 \pm 7	1181
JADES-17858	189.14222	62.28460	9.210	-19.41	< 18			< 75	< 11		1181
JADES-619	189.15825	62.22136	9.070	-20.04	< 9		< 0.05	< 5	< 24		1181
CEERS-23	214.89725	52.84386	8.998	-18.71	< 10			< 50	< 20		1345
JADES-13643	189.20417	62.27076	8.930	-18.79	< 28			< 177	< 45		1181
JADES-20110306	53.16913	-27.80292	8.924	-18.48	< 6			< 29	< 47		3215
CEERS-24	214.90125	52.84700	8.881	-19.33	< 11			< 29	< 21		1345
CEERS-7	215.01171	52.98830	8.873	-19.44	< 19			< 29	< 27		1345
JADES-20079187	53.15862	-27.83408	8.837	-19.70	< 21			< 22		40 \pm 8	1180
JADES-20111790	53.11685	-27.80056	8.827	-16.20	< 4			< 33	< 64		3215
JADES-20100293	53.16874	-27.81698	8.748	-16.95	< 5			< 34	< 197		3215
JADES-36424	53.17603	-27.81739	8.680	-17.68	< 28			< 164			1286
CEERS-1019	215.03539	52.89066	8.679	-21.36	< 34			< 7	3 \pm 1		1345

Table A1 continued

Table A1 (continued)

ID	R.A. (deg)	Decl. (deg)	z_{sys}	M_{UV} (mag)	$F_{\text{Ly}\alpha}$ ($10^{-19} \text{ erg s}^{-1} \text{ cm}^{-2}$)	$\Delta v_{\text{Ly}\alpha}$ (km s^{-1})	$f_{\text{esc}}^{\text{Ly}\alpha}$	EW $_{\text{Ly}\alpha}$ (Å, This work)	EW $_{\text{Ly}\alpha}$ (Å, Tang24)	EW $_{\text{Ly}\alpha}$ (Å, Jones24)	PID
(1)	(2)	(3)	(4)	(5)	(6)	(7)	(8)	(9)	(10)	(11)	(12)
JADES-54165	189.27184	62.19518	8.657	-19.92	< 7			< 49	< 29		1181
CEERS-80083	214.96128	52.84236	8.637	-18.25	< 19			< 34	< 31		1345
CEERS-1029	215.21876	53.06986	8.610	-21.66	< 4			< 1	3 ± 1		1345
JADES-74111	189.18051	62.18047	8.603	-19.70	< 6			< 4	< 13		1181
JADES-20213084	53.15891	-27.76508	8.485	-19.33	< 27			< 73	21 ± 3	18 ± 3	3215
JADES-6139	53.16448	-27.80218	8.481	-18.83	< 30			< 176	< 143	< 56	1180
JADES-20211388	53.18354	-27.77014	8.385	-18.43	< 12			< 39			1180
JADES-5776	189.07727	62.24253	8.374	-18.29	< 31			< 13	< 205		1181
JADES-45170	189.20716	62.17039	8.368	-18.94	< 8			< 47	< 64		1181
JADES-45131	189.21140	62.17030	8.368	-19.32	< 7		< 0.07	< 10	< 37		1181
JADES-1899	189.19774	62.25696	8.279	-19.69	146 ± 20	2 ± 44	0.66 ± 0.15	78 ± 18	136 ± 9	109 ± 13	1181
JADES-20198852	53.10776	-27.81294	8.268	-18.22	< 7			< 44	< 72		3215
CEERS-1149	215.08971	52.96618	8.175	-20.24	< 6			< 4	< 54		1345
CEERS-3	215.00519	52.99658	8.005	-15.96	< 10			< 20	< 86		1345
JADES-21842	53.15682	-27.76716	7.981	-18.64	8 ± 3	145 ± 62	0.11 ± 0.04	81 ± 16	< 2	29 ± 8	1210
GLASS-10000	3.60134	-30.37923	7.881	-20.36°	< 2			< 2	< 9		1324
GLASS-100005	3.60646	-30.38099	7.879	-20.06°	< 4			< 32	< 9		1324
GLASS-100003	3.60451	-30.38044	7.877	-20.69°	< 4			< 3	< 9		1324
GLASS-100001	3.60385	-30.38223	7.874	-20.29°	< 5			< 7	< 11		1324
CEERS-1027	214.88299	52.84042	7.822	-19.74	52 ± 14	5 ± 86		32 ± 8	26 ± 3		1345
CEERS-1023	215.18841	53.03365	7.776	-20.42	< 16			< 8	< 25		1345
CEERS-686	215.15086	52.98956	7.752	-20.69	99 ± 20	114 ± 405		25 ± 6	44 ± 3		1345
JADES-12637	53.13347	-27.76037	7.663	-20.44	20 ± 8	149 ± 80		30 ± 7	33 ± 3	9 ± 1	1180
JADES-60729	53.15661	-27.75428	7.557	-18.22	< 11			< 40			1180
JADES-44323	53.16778	-27.73616	7.556	-19.59	< 77			< 271	< 60		1180
CEERS-689	214.99905	52.94198	7.545		< 20			< 125	< 80		1345
CEERS-80445	214.84312	52.74789	7.509	-19.41	< 20			< 182	51 ± 1		1345
CEERS-80372	214.92780	52.85000	7.483	-19.52	< 43			< 298	< 14		1345
CEERS-80239	214.89605	52.86985	7.487	-18.01	< 63			< 31	219 ± 17		1345
JADES-20047266	53.17685	-27.79678	7.482	-17.70	< 8			< 3889			1180
JADES-20087739	53.20042	-27.78210	7.481	-19.18	< 83		< 0.69	< 403		41 ± 11	1180
JADES-44713	53.17293	-27.79767	7.480	-17.35	< 12			< 91			1180
CEERS-80432	214.81206	52.74675	7.477	-19.65	< 53			< 2436	53 ± 3		1345
CEERS-698	215.05032	53.00744	7.471	-20.39	< 48			< 13	9 ± 2		1345
CEERS-1163	214.99047	52.97199	7.447	-19.01	< 52			< 87	< 123		1345
JADES-38684	189.12109	62.27781	7.441	-18.93	< 15			< 36	< 61		1181
JADES-135134	53.18148	-27.76950	7.433	-18.65	< 49			< 317			1180
JADES-13552	53.18346	-27.79099	7.432	-20.16	< 115			< 458	< 32		1180
JADES-60331	189.27524	62.21244	7.431	-19.38	< 47			< 181	< 22	24 ± 6	1181

Table A1 continued

Table A1 (continued)

ID	R.A. (deg)	Decl. (deg)	z_{sys}	M_{UV} (mag)	$F_{\text{Ly}\alpha}$ ($10^{-19} \text{ erg s}^{-1} \text{ cm}^{-2}$)	$\Delta v_{\text{Ly}\alpha}$ (km s^{-1})	$f_{\text{esc}}^{\text{Ly}\alpha}$	EW $_{\text{Ly}\alpha}$ (\AA , This work)	EW $_{\text{Ly}\alpha}$ (\AA , Tang24)	EW $_{\text{Ly}\alpha}$ (\AA , Jones24)	PID
(1)	(2)	(3)	(4)	(5)	(6)	(7)	(8)	(9)	(10)	(11)	(12)
JADES-4685	189.09629	62.23914	7.415	-18.20	< 11			< 68			1181
JADES-8115	53.15508	-27.80177	7.399	-19.17	< 16			< 35	< 78		1210
GLASS-10021	3.60851	-30.41854	7.286	-21.44 ^e	< 3			< 1	< 12		1324
JADES-9425	53.17977	-27.77465	7.279	-18.07	< 48			< 290	< 68		1180
JADES-30141745	53.18012	-27.77144	7.277	-19.16	< 22			< 111			1180
JADES-10013682	53.16746	-27.77201	7.275	-16.97	24 \pm 4	197 \pm 40		277 \pm 31	259 \pm 54	146 \pm 31	1210
JADES-30147912	53.18628	-27.77904	7.274	-19.55	< 21			< 198			1180
JADES-20046019	53.18393	-27.79999	7.270	-18.86	< 14			< 87	< 32		1180
JADES-20085619	53.19105	-27.79731	7.267	-19.10	< 11		< 0.14	< 9			1286
JADES-43252	53.18714	-27.80129	7.266	-18.37	< 19			< 128			1286
JADES-20086025	53.18374	-27.79390	7.263	-18.19	< 33			< 2122	< 84		1286
JADES-20046866	53.18404	-27.79783	7.263	-18.44	< 32		< 0.48	< 72			1180
JADES-8079	53.15283	-27.80194	7.259	-17.94	< 10			< 73	< 102		1210
JADES-30141478	53.18674	-27.77064	7.245	-17.83	< 27			< 184	< 643		1180
JADES-15423	53.16959	-27.73805	7.244	-20.18	< 33			< 56	26 \pm 3	< 12	1180
JADES-30139499	53.19415	-27.76838	7.244	-18.11	< 14			< 55			1180
JADES-9886	53.16556	-27.77266	7.242	-18.28	< 21			< 67	< 36	< 63	1180
JADES-11547	53.16483	-27.78826	7.239	-19.15	< 19			< 29	< 43		1180
JADES-9942	53.16172	-27.78539	7.237	-19.11	< 29			< 62	< 91		1180
JADES-13905	53.11833	-27.76901	7.197	-19.25	< 23			< 23	< 22		1180
CEERS-1038	215.03970	52.90160	7.194	-19.47	< 15	13 \pm 234		< 14	< 161		1345
CEERS-439	214.82536	52.86306	7.179	-19.62	50 \pm 15			39 \pm 11	71 \pm 7		1345
CEERS-498	214.81304	52.83425	7.179	-19.54	< 29			< 93	33 \pm 2		1345
CEERS-80374	214.89807	52.82489	7.174	-18.11	< 62			< 882	201 \pm 15		1345
CEERS-829	214.86159	52.87616	7.167	-18.98	< 43			< 10	< 21		1345
JADES-67006	189.24982	62.24122	7.154	-20.15	< 7			< 54	< 27		1181
JADES-31803	53.16610	-27.82751	7.147	-18.52	< 13			< 94			1180
JADES-66585	189.25889	62.23745	7.143	-18.63	< 92			< 3			1181
JADES-4530	189.10914	62.23866	7.142	-18.80	< 55			< 28	< 95		1181
JADES-24819	189.13647	62.22340	7.141	-19.49	< 5		< 0.03	< 3	< 27		1181
JADES-66336	189.25929	62.23546	7.140	-19.51	< 41		< 0.22	< 74	< 56		1181
JADES-9442	53.13806	-27.78186	7.139	-18.75	< 29			< 107	< 278		1180
JADES-3982	189.10941	62.23880	7.132	-19.50	< 33			< 40	< 25		1181
CEERS-534	214.85912	52.85364	7.115	-19.69	< 51			< 32	< 21		1345
CEERS-44	215.00111	53.01127	7.104	-19.43	63 \pm 16	1233 \pm 347		59 \pm 14	83 \pm 4		1345
JADES-1936	189.19571	62.28242	7.090	-19.09	< 5			< 28	< 51		1181
JADES-13041	189.20377	62.26843	7.090	-19.17	110 \pm 18	184 \pm 44	0.30 \pm 0.05	272 \pm 58	143 \pm 7	233 \pm 43	1181
JADES-7675	189.09630	62.24797	7.089	-18.55	< 57			< 74		< 35	1181
JADES-1129	189.17975	62.28239	7.087	-19.93	157 \pm 29	0 \pm 45	0.17 \pm 0.06	47 \pm 11	52 \pm 9	91 \pm 13	1181

Table A1 continued

Table A1 (continued)

ID	R.A. (deg)	Decl. (deg)	z_{sys}	M_{UV} (mag)	$F_{\text{Ly}\alpha}$ ($10^{-19} \text{ erg s}^{-1} \text{ cm}^{-2}$)	$\Delta v_{\text{Ly}\alpha}$ (km s^{-1})	$f_{\text{esc}}^{\text{Ly}\alpha}$	$\text{EW}_{\text{Ly}\alpha}$ (\AA , This work)	$\text{EW}_{\text{Ly}\alpha}$ (\AA , Tang24)	$\text{EW}_{\text{Ly}\alpha}$ (\AA , Jones24)	PID
(1)	(2)	(3)	(4)	(5)	(6)	(7)	(8)	(9)	(10)	(11)	(12)
CEERS-542	214.83162	52.83150	7.064	-18.81	< 50		< 1815	< 23			1345
JADES-20961	53.13423	-27.76891	7.045	-18.83	< 25		< 116				1210
JADES-2389	189.19834	62.29701	7.043	-18.40	< 30		< 11			< 281	1181
JADES-1931	189.06964	62.28102	7.026	-19.33	< 14		< 8				1181
JADES-1166	189.18336	62.28772	7.025	-20.17	< 62		< 19		< 12		1181
JADES-20053246	53.17688	-27.78156	7.003	-18.24	< 20		< 153				1286
JADES-5088	189.17253	62.24054	7.001	-18.42	65 ± 21	919 ± 397	152 ± 54	< 160	< 19	282 ± 69	1181
JADES-2316	189.16253	62.25825	6.997	-17.84	< 51		< 24				1181
JADES-7424	189.23290	62.24738	6.997	-19.09	< 8		< 13		< 27		1181
CEERS-1102	215.09105	52.95428	6.994	-19.49	< 25		< 11		< 13		1345
JADES-1893	189.20531	62.25077	6.994	-19.98	< 115		< 480		< 30		1181
JADES-1254	189.18629	62.22539	6.990	-17.92	< 19		< 13		< 44		1181
JADES-20049790	53.18302	-27.78946	6.961	-17.84	< 16		< 33				1286
CEERS-716	215.08035	52.99324	6.961	-20.91	< 29		< 15		< 8		1345
CEERS-1142	215.06072	52.95871	6.957		< 45		< 101		< 20		1345
JADES-13609	53.11730	-27.76408	6.938	-19.48	< 29		< 193		< 104		1180
CEERS-717	215.08141	52.97218	6.936	-20.56	< 23		< 216		< 7		1345
CEERS-1143	215.07701	52.96950	6.934	-19.85	< 14		< 68		< 10		1345
JADES-1075	189.20260	62.27551	6.907	-19.75	29 ± 13	249 ± 104	19 ± 5	34 ± 6	< 12		1181
JADES-30074749	53.14555	-27.78380	6.878	-20.12	< 132		< 744		16 ± 4	< 18	1180
JADES-137573	53.15647	-27.76726	6.868	-17.57	< 6		< 14		< 80		3215
JADES-17509	53.14771	-27.71537	6.846	-20.36	< 45		< 154		< 22		1180
JADES-9104	189.24527	62.25253	6.816	-19.09	< 11		< 14		< 21		1181
JADES-18536	189.15531	62.28647	6.809	-19.98	44 ± 4	265 ± 20	25 ± 3	< 21	< 21	30 ± 5	1181
JADES-38681	189.13563	62.26388	6.800	-19.23	< 27		< 182		< 64		1181
JADES-15362	53.11634	-27.76194	6.797	-18.87	< 18		< 92		< 170	< 37	1180
JADES-13178	53.11817	-27.79302	6.790	-19.06	< 19		< 28		< 36		1180
JADES-73977	189.18550	62.17981	6.767	-19.55	< 6		< 3		< 17		1181
JADES-10806	189.15400	62.25954	6.761	-17.52	< 12		< 54		< 22		1181
JADES-954	189.15197	62.25964	6.760	-19.87	56 ± 18	297 ± 73	30 ± 6			62 ± 10	1181
JADES-896	189.08265	62.25248	6.759	-20.26	< 23		< 8		< 11		1181
JADES-926	189.07982	62.25646	6.756	-19.96	< 11		< 10		< 21		1181
JADES-1066	189.13808	62.27445	6.747	-19.40	< 31		< 167		< 26		1181
JADES-1076	189.13851	62.27561	6.743	-19.54	< 14		< 15		< 15		1181
JADES-28342	189.22436	62.27561	6.743	-19.77	< 66		< 7		40 ± 13		1181
CEERS-81049	214.78982	52.73079	6.738	-19.77	64 ± 16	181 ± 382	37 ± 9		99 ± 3		1345
JADES-1972	189.18840	62.30305	6.733	-19.96	< 16		< 13				1181
JADES-38420	189.17514	62.28226	6.733	-20.04	108 ± 29	158 ± 72	62 ± 9		51 ± 6		1181
JADES-4108	189.18778	62.30211	6.731		< 63		< 351				1181

Table A1 continued

Table A1 (continued)

ID	R.A. (deg)	Decl. (deg)	z_{sys}	M_{UV} (mag)	$F_{\text{Ly}\alpha}$ ($10^{-19} \text{ erg s}^{-1} \text{ cm}^{-2}$)	$\Delta v_{\text{Ly}\alpha}$ (km s^{-1})	$f_{\text{esc}}^{\text{Ly}\alpha}$	EW $_{\text{Ly}\alpha}$ (\AA , This work)	EW $_{\text{Ly}\alpha}$ (\AA , Tang24)	EW $_{\text{Ly}\alpha}$ (\AA , Jones24)	PID
(1)	(2)	(3)	(4)	(5)	(6)	(7)	(8)	(9)	(10)	(11)	(12)
JADES-1948	189.17731	62.29106	6.728	-19.84	< 14	< 0.12	< 103	< 21	< 11	< 21	1181
JADES-89464	189.18658	62.27091	6.725	-20.06	< 8	< 0.03	< 3	< 11	< 11	< 11	1181
JADES-38432	189.18617	62.27086	6.718	-20.24	< 12	< 0.02	< 8	< 8	< 8	< 8	1181
JADES-38423	189.17686	62.26454	6.713	-18.63	< 51	< 0.11	< 26	< 62	< 58	< 58	1181
JADES-2113	189.17033	62.22950	6.713	-18.95	< 48	< 0.11	< 18	< 68	< 68	< 68	1181
JADES-12359	189.17781	62.26559	6.713	-18.69	< 11	205 \pm 41	0.22 \pm 0.05	56 \pm 10	125 \pm 27	125 \pm 27	1210
JADES-4297	53.15579	-27.81520	6.713	-18.47	29 \pm 6	< 0.06	< 531	< 107	< 107	< 107	1180
JADES-13286	53.15497	-27.81580	6.713	-19.82	< 103	< 0.06	< 9	< 8	< 8	< 8	1181
JADES-38428	189.17927	62.27590	6.711	-20.42	< 27	< 0.06	< 9	< 8	< 8	< 8	1181
JADES-3334	53.15138	-27.81917	6.706	-17.96	< 19	< 0.61	< 52	< 83	< 83	< 83	1210
JADES-1203	189.15463	62.29292	6.700	-19.46	< 103	< 0.40	< 25	< 27	< 27	< 27	1181
JADES-39799	189.26352	62.15479	6.697	-18.40	< 23	< 0.04	< 177	< 36	< 36	< 36	1345
CEERS-577	214.89286	52.86516	6.695	-18.69	< 21	< 0.04	< 7	< 26	< 26	< 26	1181
JADES-44124	189.27270	62.16741	6.687	-19.16	< 12	< 0.45	< 477	43 \pm 11	43 \pm 11	43 \pm 11	1181
JADES-38509	189.09145	62.22810	6.675	-19.02	< 79	< 0.11	< 10	< 33	< 33	< 33	1181
JADES-18533	189.12121	62.28641	6.668	-19.40	< 14	143 \pm 101	0.29 \pm 0.14	14 \pm 3	49 \pm 15	40 \pm 11	1181
JADES-14373	189.14579	62.27332	6.663	-18.70	35 \pm 12	< 32	< 190	< 25	< 25	< 133	1181
JADES-8239	189.24892	62.24974	6.655	-18.20	< 21	< 21	< 23	< 8	< 8	< 8	1180
JADES-58930	53.10538	-27.72347	6.636	-20.48	< 49	< 0.13 \pm 0.03	< 290	44 \pm 10	44 \pm 10	42 \pm 7	1286
JADES-48269	53.15160	-27.78791	6.632	-17.77	< 14	< 48	< 14	< 45	< 45	< 90	1180
JADES-16625	53.16904	-27.77884	6.631	-18.74	22 \pm 5	< 5	< 41	< 119	< 119	< 90	3215
JADES-13647	53.16951	-27.75331	6.630	-19.22	< 24	< 12	< 186	< 44	< 44	< 44	1210
JADES-58911	53.17063	-27.74325	6.627	-18.49	< 24	< 50	< 217	< 45	< 45	42 \pm 5	1180
JADES-128261	53.12427	-27.77725	6.626	-16.89	< 5	< 50	< 27	< 186	< 186	< 186	1345
JADES-10005447	53.16288	-27.76928	6.623	-17.54	< 12	< 50	< 2658	< 17	< 17	< 17	1181
JADES-13607	53.13743	-27.76519	6.622	-18.79	< 50	< 374	< 0.08	< 37	< 37	< 37	1180
CEERS-386	214.83218	52.88508	6.621	-18.97	< 50	< 0.31	< 576	< 11	< 11	< 11	1181
JADES-1223	189.12034	62.29486	6.591	-19.39	< 374	< 0.01	< 3	< 13	< 13	< 13	1181
JADES-30056758	53.15005	-27.74501	6.572	-19.18	< 18	< 0.23	< 182	< 122	< 122	< 122	1181
JADES-1967	189.16503	62.30019	6.562	-19.00	< 111	< 0.12	< 29	< 17	< 17	< 17	1181
JADES-57330	189.22884	62.20400	6.550	-20.13	< 10	< 0.16	< 315	< 52	< 52	< 52	1181
JADES-78891	189.22582	62.20421	6.549	-20.03	< 7	< 37	< 30	< 86	< 86	< 86	1181
JADES-59734	189.28070	62.21083	6.548	-16.99	< 27	< 0.15	< 7	< 40	< 40	< 40	1181
JADES-58561	189.22183	62.20736	6.548	-19.07	< 33	< 0.15	< 7	< 40	< 40	< 40	1181
JADES-78455	189.23197	62.20233	6.548	-19.16	< 51	< 0.15	< 7	< 40	< 40	< 40	1181
JADES-42722	189.21063	62.16330	6.544	-18.63	< 37	< 0.15	< 7	< 40	< 40	< 40	1181
JADES-71983	189.19719	62.16706	6.543	-19.56	< 13	< 0.15	< 7	< 40	< 40	< 40	1181
CEERS-80596	214.77186	52.77819	6.542	-18.84	< 55	< 0.15	< 7	< 40	< 40	< 40	1345
JADES-13556	53.12556	-27.78676	6.388	-18.70	< 35	< 0.15	< 7	< 40	< 40	< 40	1180

Table A1 continued

Table A1 (continued)

ID	R.A. (deg)	Decl. (deg)	z_{sys}	M_{UV} (mag)	$F_{\text{Ly}\alpha}$ ($10^{-19} \text{ erg s}^{-1} \text{ cm}^{-2}$)	$\Delta v_{\text{Ly}\alpha}$ (km s^{-1})	$f_{\text{esc}}^{\text{Ly}\alpha}$	EW $_{\text{Ly}\alpha}$ (Å, This work)	EW $_{\text{Ly}\alpha}$ (Å, Tang24)	EW $_{\text{Ly}\alpha}$ (Å, Jones24)	PID
(1)	(2)	(3)	(4)	(5)	(6)	(7)	(8)	(9)	(10)	(11)	(12)
JADES-5278	53.12731	-27.78805	6.382	-18.79	< 21			< 150			1180
JADES-13902	53.19660	-27.81345	6.341	-17.88	< 16			< 82			1180
JADES-106197	53.13105	-27.80908	6.340		26 ± 6	2 ± 11		247 ± 44			3215
JADES-18846	53.13492	-27.77271	6.335	-20.09	90 ± 17	141 ± 40	0.27 ± 0.05	39 ± 2		44 ± 3	1210
JADES-14123	53.17836	-27.80098	6.334	-18.73	< 51			< 284		< 64	1180
JADES-201562	53.19404	-27.80293	6.333	-18.41	< 16		< 0.21	< 113		< 88	1180
JADES-9423	53.17583	-27.77447	6.329	-18.79	< 61			< 392			1180
JADES-18976	53.16660	-27.77240	6.327	-18.56	< 60		< 0.70	< 139			1210
JADES-14160	53.15516	-27.76072	6.314	-19.41	< 13			< 26			1180
JADES-988	189.16215	62.26381	6.312	-19.48	29 ± 10	122 ± 82	0.04 ± 0.02	12 ± 3		35 ± 9	1181
JADES-9597	53.16613	-27.77204	6.311	-18.81	32 ± 12	46 ± 29		36 ± 8		182 ± 35	1180
JADES-10009693	53.16238	-27.80332	6.286	-16.35	< 72			< 507			1210
JADES-42988	53.09068	-27.74422	6.273	-18.66	< 26			< 191			1180
CEERS-81068	214.82051	52.73715	6.272	-18.34	< 21			< 616			1345
JADES-58850	53.09517	-27.76061	6.270	-19.79	< 20			< 13			1180
JADES-16418	53.08340	-27.76447	6.267	-19.70	< 21			< 111			1180
JADES-15265	53.08311	-27.78635	6.265	-19.45	< 42			< 106			1180
JADES-9319	53.16902	-27.80079	6.249	-18.87	< 45			< 268		< 117	1180
CEERS-67	215.01560	53.01186	6.212	-18.48	< 39			< 38			1345
CEERS-1561	215.16610	53.07076	6.211	-20.33	332 ± 61	262 ± 380		67 ± 8			1345
JADES-17138	53.08604	-27.74760	6.210	-19.12	< 49			< 293		< 220	1180
CEERS-1065	215.11685	53.00108	6.190	-19.97	< 31			< 351			1345
JADES-9547	53.20800	-27.79005	6.185	-19.08	885 ± 83	1230 ± 184		18 ± 2			1180
JADES-13304	53.19852	-27.80818	6.172	-19.45	< 342			< 1981			1180
CEERS-31329	215.05512	53.00085	6.142	-20.73	< 24			< 51			1345
JADES-52486	53.19546	-27.77683	6.127	-18.21	< 45			< 72			1180
CEERS-355	214.80648	52.87883	6.111	-19.67	< 44			< 29			1345
CEERS-1518	215.00680	52.96504	6.108	-21.17	< 17			< 83			1345
JADES-9867	53.15613	-27.77585	6.105	-19.20	< 48			< 186			1180
JADES-209277	53.15618	-27.77576	6.102	-19.13	< 46		< 0.31	< 363			1180
JADES-9877	53.15953	-27.77152	6.101	-20.36	< 42			< 25			1180
CEERS-81063	214.79911	52.72512	6.086	-19.22	< 19			< 47			1345
CEERS-618	214.87647	52.83941	6.066	-18.94	< 19			< 53			1345
JADES-99302	53.12582	-27.81823	6.065	-18.49	< 13			< 16			3215
CEERS-603	214.86725	52.83674	6.061	-19.53	< 107			< 187			1345
JADES-13887	53.19588	-27.76843	6.052	-18.62	< 114			< 705			1180
CEERS-362	214.81269	52.88154	6.051	-19.00	< 31			< 61			1345
JADES-7351	189.10818	62.24715	6.047	-18.90	< 96		< 0.27	< 265		< 32	1181
CEERS-397	214.83620	52.88269	6.010	-21.18	< 20			< 1157			1345

Table A1 continued

Table A1 (continued)

ID	R.A. (deg)	Decl. (deg)	z_{sys}	M_{UV} (mag)	$F_{\text{Ly}\alpha}$ ($10^{-19} \text{ erg s}^{-1} \text{ cm}^{-2}$)	$\Delta v_{\text{Ly}\alpha}$ (km s^{-1})	$f_{\text{esc}}^{\text{Ly}\alpha}$	EW $_{\text{Ly}\alpha}$ (\AA , This work)	EW $_{\text{Ly}\alpha}$ (\AA , Tang24)	EW $_{\text{Ly}\alpha}$ (\AA , Jones24)	PID
(1)	(2)	(3)	(4)	(5)	(6)	(7)	(8)	(9)	(10)	(11)	(12)
JADES-9457	53.17324	-27.79567	6.002	-19.49	< 30			< 86			1180
JADES-41002	53.14227	-27.80684	5.989	-18.60	< 99			< 10			1180
JADES-4379	189.21939	62.23824	5.988	-19.61	< 25			< 11			1181
JADES-14133	53.17264	-27.76706	5.986	-18.95	< 68			< 370			1180
JADES-113056	53.11052	-27.79849	5.986	-16.50	< 33			< 221		347 \pm 116	3215
JADES-9735	53.19938	-27.79627	5.985	-19.52	< 19			< 29			1180
JADES-9880	53.16063	-27.77160	5.974	-17.89	< 86			< 552		48 \pm 10	1180
JADES-54058	53.15705	-27.77272	5.972		< 22			< 34			1180
JADES-58441	189.28642	62.20702	5.969	-20.97	93 \pm 32	243 \pm 95	0.19 \pm 0.07	13 \pm 2			1181
JADES-30080593	53.14885	-27.80970	5.960	-17.54	< 18			< 28			3215
JADES-51068	53.14902	-27.78070	5.957	-17.89	< 63		< 0.86	< 32			1286
JADES-13618	53.11911	-27.76080	5.956	-19.46	< 38			< 274			1180
JADES-199524	53.16692	-27.81033	5.942	-15.72	< 18			< 153		< 992	3215
JADES-6002	53.11041	-27.80892	5.937	-18.63	56 \pm 10	2 \pm 46	0.49 \pm 0.11	64 \pm 10		45 \pm 7	1210
JADES-200277	53.10969	-27.80761	5.937	-17.34	< 13			< 41			3215
JADES-9422	53.12175	-27.79763	5.936	-19.78	208 \pm 26	1 \pm 37	0.39 \pm 0.05	62 \pm 3		144 \pm 12	1210
JADES-24707	189.14972	62.22212	5.936	-18.44	< 143		< 0.39	< 882		< 252	1181
JADES-9795	53.14610	-27.79456	5.935	-19.53	< 128		< 1.75	< 417			1180
JADES-51778	53.13836	-27.77878	5.935	-18.45	< 122		< 0.26	< 187			1180
JADES-57895	53.14504	-27.76282	5.933	-19.88	< 35			< 39			1180
JADES-9697	53.13044	-27.80236	5.932	-19.09	< 70		< 0.60	< 373		< 89	1180
JADES-55977	53.15217	-27.76817	5.931	-16.57	< 39			< 76		< 1087	1180
CEERS-80954	214.91818	52.81183	5.930	-18.11	< 56			< 533			1345
JADES-51925	53.15218	-27.77840	5.928	-17.16	< 97			< 756			1286
JADES-108606	53.15420	-27.80551	5.928	-16.50	< 39			< 295		< 73	3215
JADES-17213	53.16192	-27.73993	5.927	-19.47	< 54			< 77			1180
JADES-99671	53.12664	-27.81773	5.923	-17.96	< 30			< 94			3215
JADES-16431	53.10547	-27.76115	5.922	-20.01	< 117			< 70			1180
JADES-53841	53.15444	-27.77332	5.922	-16.38	< 72			< 505			1180
JADES-9833	53.14208	-27.77985	5.921	-20.21	< 60			< 81			1180
JADES-9365	53.16280	-27.76084	5.921	-19.64	< 138			< 617		37 \pm 6	1180
JADES-13651	53.14987	-27.75283	5.920	-19.39	< 46			< 339			1180
JADES-10013704	53.12654	-27.81809	5.920	-18.94	< 71		< 0.25	< 59			1210
JADES-13620	53.12259	-27.76057	5.919	-19.76	< 22			< 76			1180
JADES-42905	53.14077	-27.80218	5.916	-19.30	< 65		< 0.16	< 140		< 29	1180
JADES-10012336	53.16233	-27.76687	5.916	-18.31	< 14			< 28			1180
JADES-42154	53.11415	-27.80404	5.916	-17.27	< 224			< 1315			1180
JADES-9860	53.16773	-27.76816	5.911	-17.95	< 29			< 142			1180
JADES-12052	53.19905	-27.77259	5.900		< 246			< 1618			1180

Table A1 continued

Table A1 (continued)

ID	R.A. (deg)	Decl. (deg)	z_{sys}	M_{UV} (mag)	$F_{\text{Ly}\alpha}$ ($10^{-19} \text{ erg s}^{-1} \text{ cm}^{-2}$)	$\Delta v_{\text{Ly}\alpha}$ (km s^{-1})	$f_{\text{esc}}^{\text{Ly}\alpha}$	$\text{EW}_{\text{Ly}\alpha}$ (\AA , This work)	$\text{EW}_{\text{Ly}\alpha}$ (\AA , Tang24)	$\text{EW}_{\text{Ly}\alpha}$ (\AA , Jones24)	PID
(1)	(2)	(3)	(4)	(5)	(6)	(7)	(8)	(9)	(10)	(11)	(12)
JADES-27376	189.10034	62.26994	5.898	-19.60	< 20		< 10	< 10			1181
JADES-5274	53.18628	-27.78663	5.894	-16.77	< 228		< 1099	< 1099			1180
JADES-59998	53.15430	-27.75659	5.890	-17.85	< 56		< 0.87	< 206			1180
JADES-19606	53.17655	-27.77111	5.889	-18.68	89 ± 21	15 ± 77		103 ± 10		< 45	1210
JADES-52721	53.20298	-27.77613	5.887	-19.45	< 54			< 107			1180
CEERS-1677	215.18874	53.06438	5.877	-20.57	< 14			< 576			1345
JADES-61888	189.16802	62.21701	5.875	-18.81	< 22		< 0.05	< 28			1181
JADES-53927	189.27735	62.19461	5.872	-19.06	< 35		< 0.16	< 5			1181
JADES-40649	53.18393	-27.80759	5.866	-18.44	< 17			< 37			1180
JADES-9696	53.17752	-27.80252	5.864	-19.09	< 36			< 264			1180
JADES-978	189.12842	62.26277	5.864	-18.64	< 234		< 2.47	< 1871			1181
CEERS-81018	214.80548	52.75473	5.861	-19.22	< 15			< 30			1345
JADES-44099	189.25707	62.16735	5.859	-19.89	185 ± 28	1215 ± 164	0.39 ± 0.06	22 ± 3			1181
JADES-17224	53.13159	-27.73881	5.858	-18.71	< 181			< 1140			1180
JADES-40396	53.17986	-27.80828	5.834	-18.53	< 74		< 0.27	< 529		< 64	1180
JADES-201127	53.16685	-27.80413	5.831	-18.47	< 68			< 46		< 64	3215
JADES-13638	53.14197	-27.75523	5.829	-19.60	< 143			< 160			1180
JADES-9301	53.16673	-27.80424	5.828	-21.12	< 120			< 37			1180
JADES-43337	53.18800	-27.80108	5.826	-16.36	< 68			< 723		< 227	1180
JADES-104813	53.15737	-27.81099	5.823	-16.19	< 12			< 264			3215
JADES-10005113	53.16730	-27.80287	5.821	-17.82	< 24			< 215			1210
JADES-10056849	53.11351	-27.77284	5.814	-18.12	37 ± 10	228 ± 61	0.30 ± 0.08	50 ± 12		96 ± 19	1210
JADES-9842	53.15409	-27.76606	5.797	-18.14	< 16			< 114			1180
JADES-82830	189.23788	62.23408	5.797	-19.72	< 18		< 0.10	< 8			1181
JADES-13639	53.12554	-27.75505	5.792	-19.49	< 37			< 40			1180
JADES-13851	53.13023	-27.77997	5.792	-17.96	< 74			< 352			1180
JADES-109389	53.12210	-27.80429	5.789	-18.02	16 ± 5	375 ± 93		37 ± 11		44 ± 12	3215
JADES-113	189.12383	62.21550	5.788	-19.35	< 13			< 21			1181
JADES-14137	53.12247	-27.80592	5.786	-18.15	< 30			< 202			1180
JADES-51871	53.13385	-27.77858	5.783	-16.74	< 54			< 371			1286
JADES-47918	189.20825	62.17809	5.781	-18.03	< 52		< 0.51	< 64			1181
JADES-13466	53.19185	-27.82499	5.780	-19.78	< 832			< 3807			1180
JADES-53648	53.13181	-27.77380	5.780	-18.63	< 111			< 832			1180
JADES-40000170	53.13600	-27.79849	5.777	-18.98	45 ± 15	200 ± 75	0.12 ± 0.04	60 ± 18		< 24	1180
JADES-54834	189.22124	62.19705	5.776	-18.45	< 24			< 11			1181
JADES-9792	53.16713	-27.79424	5.773	-17.50	< 77			< 369		< 51	1180
JADES-903	189.09179	62.25374	5.772	-19.19	59 ± 26	257 ± 123	0.42 ± 0.20	28 ± 8		< 27	1181
CEERS-403	214.82897	52.87570	5.771	-20.23	< 34			< 184			1345
JADES-56886	53.13557	-27.76569	5.769	-16.16	< 49			< 91			1180

Table A1 continued

Table A1 (continued)

ID	R.A. (deg)	Decl. (deg)	z_{sys}	M_{UV} (mag)	$F_{\text{Ly}\alpha}$ ($10^{-19} \text{ erg s}^{-1} \text{ cm}^{-2}$)	$\Delta v_{\text{Ly}\alpha}$ (km s^{-1})	$f_{\text{esc}}^{\text{Ly}\alpha}$	EW $_{\text{Ly}\alpha}$ (\AA , This work)	EW $_{\text{Ly}\alpha}$ (\AA , Tang24)	EW $_{\text{Ly}\alpha}$ (\AA , Jones24)	PID
(1)	(2)	(3)	(4)	(5)	(6)	(7)	(8)	(9)	(10)	(11)	(12)
JADES-1103	189.15823	62.27843	5.769	-19.28	< 128			< 216			1181
JADES-3968	53.14505	-27.81643	5.768	-18.00	< 41		< 1.68	< 75			1210
JADES-57491	53.10430	-27.77514	5.768	-18.23	< 1000			< 14219			1180
JADES-4404	53.11537	-27.81477	5.764	-19.25	< 30		< 0.11	< 14			1210
JADES-36826	53.11775	-27.81653	5.763	-17.86	< 36		< 0.51	< 71			1286
JADES-56812	53.13580	-27.76591	5.761	-16.33	< 38		< 0.49	< 47		< 214	1180
JADES-15210	53.21160	-27.79639	5.758	-19.23	< 41			< 68			1180
CEERS-83592	214.95669	52.83378	5.736	-18.18	< 42			< 35			1345
JADES-1054	189.15742	62.27361	5.677	-19.71	< 90		< 1.40	< 29			1181
CEERS-80916	214.89163	52.81594	5.674	-19.06	53 \pm 18	13 \pm 226		57 \pm 14			1345
CEERS-323	214.87256	52.87595	5.671	-19.24	< 79			< 50			1345
CEERS-545	214.86441	52.85366	5.668	-19.76	< 34			< 8			1345
CEERS-2168	215.15260	53.05706	5.662	-19.73	< 24			< 14			1345
JADES-2000	189.17595	62.31153	5.659	-20.00	< 34		< 0.17	< 8			1181
JADES-98587	53.16273	-27.81904	5.643	-17.92	< 101			< 127			1180
CEERS-356	214.80529	52.87786	5.641	-17.73	< 32			< 19			1345
JADES-2347	189.11152	62.27794	5.635	-19.68	< 35		< 0.05	< 14			1181
JADES-201867	53.18817	-27.80149	5.633	-19.12	< 128			< 133			1180
CEERS-746	214.80914	52.86848	5.628	-17.16	< 60			< 19			1345
JADES-5888	189.11400	62.24294	5.620	-18.17	< 161		< 2.03	< 168			1181
JADES-6384	53.13059	-27.80771	5.615	-18.57	< 67			< 60			1210
JADES-32880	53.17350	-27.82507	5.609	-18.25	< 104		< 1.17	< 810		< 462	1286
JADES-34104	53.18064	-27.82239	5.607	-20.13	< 100		< 0.15	< 27			1286
JADES-964	189.13724	62.26064	5.600	-19.47	123 \pm 26	560 \pm 52	0.21 \pm 0.04	74 \pm 19		< 45	1181
JADES-8541	189.10627	62.25055	5.598	-18.93	< 38		< 0.17	< 36			1181
JADES-27003	189.01460	62.26820	5.596	-20.15	< 27		< 0.04	< 4			1181
JADES-1093	189.17974	62.22463	5.595	-17.60	< 17			< 2977			1181
JADES-37596	53.18200	-27.81476	5.591	-17.54	< 21			< 35			1180
JADES-16745	53.13002	-27.77839	5.567	-19.58	< 25		< 0.14	< 9			1210
JADES-208643	53.13021	-27.77836	5.563	-17.98	< 54			< 270			3215
JADES-6246	53.12972	-27.80818	5.562	-18.05	< 18		< 0.28	< 23			1210
JADES-30080873	53.15167	-27.80925	5.561	-17.43	< 20			< 160			3215
JADES-101167	53.15531	-27.81587	5.560	-17.29	< 58			< 318			3215
JADES-13424	53.12659	-27.75398	5.555	-17.37	< 55			< 466			1180
JADES-40000190	53.13197	-27.77920	5.546	-18.89	< 117		< 0.27	< 140			1180
JADES-761	189.18089	62.23888	5.545	-18.88	< 93		< 0.51	< 93			1181
JADES-48915	53.14668	-27.78620	5.522	-19.79	< 62		< 0.36	< 335			1180
JADES-201906	53.14565	-27.80150	5.520	-16.80	20 \pm 6	22 \pm 105		210 \pm 44		231 \pm 53	3215
CEERS-381	214.81967	52.87976	5.519	-18.63	< 22			< 5			1345

Table A1 continued

Table A1 (continued)

ID	R.A. (deg)	Decl. (deg)	z_{sys}	M_{UV} (mag)	$F_{\text{Ly}\alpha}$ ($10^{-19} \text{ erg s}^{-1} \text{ cm}^{-2}$)	$\Delta v_{\text{Ly}\alpha}$ (km s^{-1})	$f_{\text{esc}}^{\text{Ly}\alpha}$	$\text{EW}_{\text{Ly}\alpha}$ (\AA , This work)	$\text{EW}_{\text{Ly}\alpha}$ (\AA , Tang24)	$\text{EW}_{\text{Ly}\alpha}$ (\AA , Jones24)	PID
(1)	(2)	(3)	(4)	(5)	(6)	(7)	(8)	(9)	(10)	(11)	(12)
JADES-10016374	53.11572	-27.77496	5.503	-18.58	< 18		< 0.12	< 29			1210
CEERS-1334	214.76836	52.71764	5.503	-20.32	75 ± 27	1049 ± 407		25 ± 4			1345
JADES-80185	189.14847	62.21166	5.488	-18.85	< 124		< 0.55	< 51			1181
JADES-2430	53.12819	-27.78769	5.486	-18.44	< 44			< 281		< 211	1180
JADES-38502	189.10968	62.29506	5.483	-19.49	< 91			< 21		< 78	1181
JADES-61570	53.16589	-27.75166	5.483	-17.65	< 216		< 2.28	< 1494			1180
JADES-9364	53.16574	-27.78492	5.475	-18.66	< 109			< 723			1180
JADES-57603	53.11698	-27.75542	5.470	-18.36	< 68			< 315			1180
JADES-4873	53.16611	-27.78574	5.463	-18.91	< 242			< 2447			1180
JADES-14285	189.12828	62.27297	5.451	-18.87	< 116			< 335			1181
CEERS-80576	214.76963	52.77294	5.450	-19.15	< 38			< 25			1345
JADES-13174	53.16405	-27.79972	5.448	-19.68	< 253			< 684			1180
JADES-24006	189.00733	62.25215	5.447	-19.42	< 48		< 0.07	< 298			1181
JADES-57471	53.11438	-27.79210	5.445	-18.04	< 91			< 524			1180
JADES-1882	189.08862	62.23949	5.443	-19.91	< 183		< 0.17	< 51			1181
JADES-9343	53.12874	-27.79787	5.443	-15.61	< 27		< 0.26	< 247			1210
JADES-113719	53.12429	-27.79744	5.443	-18.19	< 80			< 612			3215
JADES-9743	53.12300	-27.79661	5.440	-17.53	< 41		< 0.18	< 254			1210
JADES-13878	53.12647	-27.80709	5.435	-18.79	< 27			< 197			1180
CEERS-81026	214.80984	52.75422	5.433	-18.60	< 54			< 7			1345
CEERS-80573	214.77392	52.78060	5.428	-19.16	< 169			< 36			1345
CEERS-81032	214.81262	52.75485	5.427	-19.23	< 27			< 2782			1345
JADES-956	189.10637	62.25971	5.423	-19.49	< 55		< 0.08	< 16			1181
JADES-63089	189.23015	62.22080	5.400	-18.67	< 215		< 0.87	< 1130		< 285	1181
JADES-81497	189.23922	62.21980	5.392	-17.21	< 65		< 0.74	< 485			1181
JADES-53419	53.18549	-27.77442	5.387	-17.52	< 139			< 1093			1180
JADES-13884	53.12776	-27.78098	5.386	-17.96	< 144			< 847			1180
JADES-58658	53.10997	-27.75552	5.382	-18.56	< 30			< 84			1180
JADES-59788	189.24171	62.21099	5.381	-18.28	< 223		< 3.06	< 1521			1181
JADES-17041	53.09052	-27.77609	5.381	-19.41	< 79			< 331			1180
CEERS-1401	215.24580	53.06530	5.376	-19.88	< 42			< 8			1345
JADES-13534	53.20532	-27.80460	5.375	-19.15	< 68			< 451			1180
JADES-212506	53.15584	-27.76672	5.350	-18.55	< 79			< 602		54 ± 15	3215
JADES-643	189.11032	62.22544	5.347	-20.40	< 155		< 0.09	< 27			1181
JADES-46214	53.14009	-27.72568	5.342	-14.80	< 38			< 617			1180
JADES-967	189.12198	62.26131	5.323	-18.83	< 66		< 0.21	< 442			1181
JADES-38385	189.12302	62.27360	5.317		< 42			< 350			1181
CEERS-2174	215.08342	52.99151	5.314	-19.72	< 41			< 36			1345
CEERS-1620	215.08717	53.00289	5.303	-20.01	< 15			< 13			1345

Table A1 continued

Table A1 (continued)

ID	R.A. (deg)	Decl. (deg)	z_{sys}	M_{UV} (mag)	$F_{\text{Ly}\alpha}$ ($10^{-19} \text{ erg s}^{-1} \text{ cm}^{-2}$)	$\Delta v_{\text{Ly}\alpha}$ (km s^{-1})	$f_{\text{esc}}^{\text{Ly}\alpha}$	EW $_{\text{Ly}\alpha}$ (\AA , This work)	EW $_{\text{Ly}\alpha}$ (\AA , Tang24)	EW $_{\text{Ly}\alpha}$ (\AA , Jones24)	PID
(1)	(2)	(3)	(4)	(5)	(6)	(7)	(8)	(9)	(10)	(11)	(12)
JADES-4982	189.10085	62.24018	5.302	-18.98	< 47			< 179			1181
CEERS-1420	215.09286	52.96070	5.301	-17.41	< 23			< 13			1345
CEERS-81022	214.80045	52.74889	5.300	-19.09	< 30			< 30			1345
JADES-1580	189.09491	62.23946	5.299	-19.43	< 155			< 60			1181
JADES-10001897	189.14837	62.25365	5.299	-18.26	< 111			< 191			1181
JADES-37657	53.11913	-27.81465	5.293	-16.71	< 68			< 532			1180
JADES-62846	53.14837	-27.74662	5.290	-18.29	50 ± 16	510 ± 382		100 ± 26		< 146	1180
CEERS-2123	214.82458	52.84573	5.289	-20.54	< 153			< 442			1345
CEERS-83772	214.78573	52.73155	5.288	-18.81	< 16			< 5			1345
CEERS-1465	214.88800	52.88825	5.280	-18.92	< 21			< 877			1345
CEERS-2116	214.81169	52.83724	5.280	-20.01	< 21			< 144			1345
JADES-758	189.11960	62.23855	5.275	-19.79	< 220			< 56			1181
JADES-2845	189.15456	62.24754	5.273	-19.09	< 160			< 101			1181
JADES-3012	189.12011	62.30436	5.272	-19.59	< 111			< 593			1181
JADES-10005323	53.15761	-27.77103	5.270	-15.78	< 55			< 514			1180
CEERS-314	214.86895	52.87721	5.270	-18.67	< 38			< 14			1345
JADES-3608	189.18476	62.27329	5.269	-19.48	< 26			< 16			1181
JADES-134811	53.16416	-27.76984	5.269	-17.21	< 26			< 186			3215
CEERS-80072	214.89085	52.81394	5.268	-18.00	< 54			< 10			1345
CEERS-4210	215.23721	53.06109	5.267	-19.78	< 11			< 593			1345
JADES-38648	189.14568	62.26426	5.266	-19.28	< 556			< 2436			1181
JADES-131133	53.15615	-27.77341	5.266	-16.44	< 15			< 150			3215
JADES-127079	53.15090	-27.77912	5.264	-16.03	< 22			< 213			3215
JADES-9821	53.15106	-27.78293	5.263	-19.49	< 87			< 52			1180
JADES-49688	53.15031	-27.78446	5.261	-18.27	< 315			< 2246			1286
CEERS-2782	214.82345	52.83028	5.261	-19.05	177 ± 48	1187 ± 349		221 ± 27			1345
JADES-13707	53.13565	-27.75468	5.258	-17.73	< 161			< 1364			1180
JADES-50774	53.12718	-27.78148	5.255	-17.44	< 28			< 104			1180
JADES-103483	53.18831	-27.81283	5.252	-17.85	< 534			< 3450			1180
JADES-56853	53.08176	-27.78766	5.234	-18.14	< 38			< 658			1180
JADES-56120	189.31186	62.20057	5.232	-18.59	< 123			< 108			1181
JADES-77652	189.29323	62.19900	5.229	-18.03	< 48			< 172			1181
JADES-59156	189.30617	62.20920	5.221	-18.84	< 24			< 315			1181
JADES-58711	189.30647	62.20776	5.220	-18.08	< 81			< 214			1181
CEERS-1672	214.74464	52.75031	5.206	-20.50	< 23			< 8			1345
JADES-1560	189.10031	62.23085	5.197	-19.53	< 302			< 99			1181
JADES-80875	189.20629	62.21533	5.193	-19.81	< 42			< 8			1181
JADES-6189	189.24977	62.24390	5.191	-18.62	< 29			< 1130			1181
JADES-78773	189.20294	62.20465	5.188	-20.47	< 28			< 3			1181

Table A1 continued

Table A1 (continued)

ID	R.A. (deg)	Decl. (deg)	z_{sys}	M_{UV} (mag)	$F_{\text{Ly}\alpha}$ ($10^{-19} \text{ erg s}^{-1} \text{ cm}^{-2}$)	$\Delta v_{\text{Ly}\alpha}$ (km s^{-1})	$f_{\text{esc}}^{\text{Ly}\alpha}$	$\text{EW}_{\text{Ly}\alpha}$ (\AA , This work)	$\text{EW}_{\text{Ly}\alpha}$ (\AA , Tang24)	$\text{EW}_{\text{Ly}\alpha}$ (\AA , Jones24)	PID
(1)	(2)	(3)	(4)	(5)	(6)	(7)	(8)	(9)	(10)	(11)	(12)
JADES-8591	189.16261	62.25079	5.187	-18.26	< 75	< 0.38	< 0.38	< 523			1181
JADES-61712	189.22121	62.21652	5.184	-19.54	< 144	< 0.67	< 0.67	< 58			1181
JADES-59412	189.15632	62.21000	5.184	-20.26	< 212	< 0.28	< 0.28	< 28			1181
JADES-62955	189.23545	62.22043	5.184	-19.48	312 ± 68	1180 ± 200	0.48 ± 0.13	66 ± 13			1181
JADES-79349	189.20968	62.20725	5.183	-19.80	< 169	< 0.42	< 0.42	< 54			1181
JADES-607	189.11695	62.22208	5.182	-19.60	< 251	< 0.52	< 0.52	< 61			1181
JADES-26786	189.11855	62.24276	5.180	-18.84	< 63	< 0.67	< 0.67	< 533			1181
JADES-721	189.11532	62.23410	5.178	-19.01	< 295	< 0.51	< 0.51	< 184	< 61		1181
JADES-62309	189.24898	62.21835	5.172	-18.70	< 171	< 0.49	< 0.49	< 179			1181
JADES-1000850	189.26356	62.24915	5.157	-18.22	< 213	< 0.57	< 0.57	< 260			1181
CEERS-82052	214.76656	52.78227	5.156	-18.16	< 45	< 0.64	< 0.64	< 64			1345
CEERS-1267	215.22204	53.02737	5.154	-19.65	< 24	< 199	< 199	< 75			1345
CEERS-37697	214.89146	52.86746	5.150	-19.61	< 11	< 75	< 75	< 19			1345
JADES-1065	189.06428	62.27430	5.145	-19.24	< 15	< 19	< 19	< 19			1181
JADES-40045	53.12760	-27.80896	5.128	-19.12	< 135	< 0.57	< 0.57	< 126			1180
JADES-1617	189.16578	62.25420	5.124	-18.64	< 79	< 1.34	< 1.34	< 59			1181
JADES-4902	53.11852	-27.81297	5.123	-19.07	< 7	< 3	< 3	< 3			1210
JADES-9452	53.11583	-27.79755	5.122	-17.98	< 69	< 0.39	< 0.39	< 658			1210
JADES-46903	189.06961	62.27808	5.117	-17.70	< 86	< 0.29	< 0.29	< 616			1181
JADES-83030	189.24257	62.23853	5.115	-17.68	< 302	< 2447	< 2447	< 2447			1181
CEERS-1759	215.03644	52.94175	5.104	-20.58	< 295	< 687	< 687	< 687			1345
CEERS-1912	215.01083	53.01333	5.104	-18.94	< 33	< 99	< 99	< 99			1345
JADES-82960	189.25460	62.23668	5.092	-19.25	< 570	< 1.39	< 1.39	< 319	< 112		1181
CEERS-1699	215.05335	52.96489	5.078	-19.91	< 18	< 13	< 13	< 13			1345
JADES-10015338	53.11535	-27.77289	5.076	-19.45	336 ± 94	1088 ± 306	0.94 ± 0.31	82 ± 21	< 66		1210
CEERS-11383	215.08614	52.95221	5.072	-19.00	< 46	< 523	< 523	< 523			1345
JADES-16120	53.21077	-27.81382	5.071	-18.53	< 410	< 3680	< 3680	< 3680			1180
CEERS-4196	215.15341	53.01636	5.065	-20.01	< 9	< 101	< 101	< 101			1345
JADES-10009320	53.15623	-27.80074	5.059	-16.64	< 96	< 336	< 336	< 336			1210
JADES-9901	53.17178	-27.77699	5.054	-18.95	< 166	< 75	< 75	< 75			1180
JADES-5759	53.14946	-27.80979	5.052	-18.00	< 317	< 2.61	< 2.61	< 2518	< 248		1210
CEERS-1691	215.18543	53.05937	5.044	-18.66	< 94	< 13	< 13	< 13			1345
JADES-17251	53.12766	-27.77695	5.041	-17.82	< 144	< 137	< 137	< 137			1210
JADES-13169	53.20060	-27.80498	5.039	-20.40	< 498	< 2025	< 2025	< 2025			1180
CEERS-1536	214.97723	52.94078	5.038	-20.17	169 ± 46	15 ± 259	6.28 ± 2.12	30 ± 8			1345
JADES-40623	189.25114	62.15723	5.037	-16.94	366 ± 89	1230 ± 203	6.28 ± 2.12	64 ± 15			1181
JADES-70920	189.25096	62.16038	5.036	-19.39	< 343	< 0.37	< 0.37	< 335			1181
JADES-44699	189.24725	62.16897	5.036	-17.06	< 378	< 5.33	< 5.33	< 2782			1181
JADES-71093	189.27572	62.16169	5.035	-19.24	< 97	< 0.12	< 0.12	< 34			1181

Table A1 continued

Table A1 (continued)

ID	R.A. (deg)	Decl. (deg)	z_{sys}	M_{UV} (mag)	$F_{\text{Ly}\alpha}$ ($10^{-19} \text{ erg s}^{-1} \text{ cm}^{-2}$)	$\Delta v_{\text{Ly}\alpha}$ (km s^{-1})	$f_{\text{esc}}^{\text{Ly}\alpha}$	EW $_{\text{Ly}\alpha}$ (\AA , This work)	EW $_{\text{Ly}\alpha}$ (\AA , Tang24)	EW $_{\text{Ly}\alpha}$ (\AA , Jones24)	PID
(1)	(2)	(3)	(4)	(5)	(6)	(7)	(8)	(9)	(10)	(11)	(12)
JADES-9928	53.12812	-27.78988	5.030	-18.88	< 560			< 341			1180
JADES-201249	53.13076	-27.80391	5.027	-20.30	< 33			< 6			3215
JADES-13823	189.14074	62.27149	5.020	-17.16	< 213			< 1592			1181
JADES-45267	53.12144	-27.79616	5.019	-16.97	< 266			< 1818			1180
JADES-13410	189.18884	62.26991	5.018	-19.37	< 80			< 32			1181
JADES-38493	189.02753	62.25374	5.016	-18.82	616 ± 144	1216 ± 343	1.93 ± 0.55	291 ± 82		< 121	1181
CEERS-1374	214.94391	52.85004	4.999	-20.17	165 ± 45	12 ± 170		35 ± 6			1345
CEERS-1173	215.15421	52.95585	4.999	-19.67	< 90			< 10			1345
CEERS-85836	214.83120	52.75179	4.995	-17.47	< 144			< 11			1345
CEERS-82507	214.85321	52.84837	4.986	-18.51	< 12			< 10			1345
JADES-58458	189.19901	62.20702	4.957	-16.80	< 376			< 2977			1181
JADES-108708	53.19662	-27.80531	4.956	-17.71	< 97			< 373		< 527	1180
JADES-109893	53.16091	-27.80354	4.950	-16.71	< 78			< 254		< 432	3215
JADES-39617	53.13157	-27.80990	4.945	-19.22	< 401			< 135			1180
JADES-940	189.14179	62.25841	4.941	-19.36	< 250			< 877		< 167	1181
JADES-13229	53.14697	-27.75220	4.940	-18.51	< 139			< 889			1180
JADES-17722	189.10888	62.28422	4.935	-19.05	< 293			< 175			1181
JADES-1716	189.11565	62.29659	4.933	-19.15	800 ± 201	12 ± 234	2.61 ± 0.76	133 ± 37		< 183	1181
JADES-101062	53.12103	-27.81599	4.929	-18.22	113 ± 17	1 ± 74		85 ± 6		< 274	3215
JADES-12645	53.14645	-27.76004	4.928	-20.32	< 885			< 198			1180
JADES-17014	53.21033	-27.78916	4.918	-17.70	< 954			< 5709		< 615	1180
JADES-834	189.09701	62.24698	4.913	-18.75	< 198			< 1815			1181
CR2-z16-1	214.91455	52.94302	4.912	-16.42	< 9			< 87			2750
JADES-666	189.11341	62.22766	4.912	-18.50	< 181			< 1157			1181
CEERS-DSFG-1	214.90912	52.93720	4.910	-15.66	< 11			< 1			2750
JADES-8113	53.12300	-27.80176	4.903	-18.06	< 54			< 147			1210
CEERS-2140	214.79601	52.71588	4.897	-19.57	124 ± 30	18 ± 216		29 ± 7			1345
CEERS-1539	214.98008	52.94266	4.892	-19.79	< 40			< 18			1345
JADES-10005217	53.17351	-27.77187	4.888	-18.02	< 32			< 263			1210
JADES-1208	189.10826	62.29319	4.888	-19.54	< 563			< 281			1181
JADES-6759	189.15364	62.24548	4.887	-18.69	< 97			< 554			1181
JADES-17260	53.12689	-27.77689	4.885	-18.47	< 64			< 582			1210
JADES-920	189.09814	62.25555	4.885	-20.43	< 99			< 19			1181
JADES-105373	53.19146	-27.81014	4.880	-18.84	< 189			< 1199			1180
JADES-17376	53.12965	-27.72609	4.876	-19.59	< 419			< 2217			1180
JADES-17242	53.15806	-27.73707	4.874	-19.90	< 543			< 1271			1180
JADES-10013204	53.19407	-27.76912	4.871	-18.52	993 ± 65	1213 ± 88	7.47 ± 1.08	86 ± 7			1180
JADES-126180	53.18519	-27.78044	4.869	-18.49	< 991			< 77			1180
JADES-4009	53.15705	-27.81629	4.864	-19.07	< 10			< 319			1210

Table A1 continued

Table A1 (continued)

ID	R.A. (deg)	Decl. (deg)	z_{sys}	M_{UV} (mag)	$F_{\text{Ly}\alpha}$ (10^{-19} erg s $^{-1}$ cm $^{-2}$)	$\Delta v_{\text{Ly}\alpha}$ (km s $^{-1}$)	$f_{\text{esc}}^{\text{Ly}\alpha}$	EW $_{\text{Ly}\alpha}$ (Å, This work)	EW $_{\text{Ly}\alpha}$ (Å, Tang24)	EW $_{\text{Ly}\alpha}$ (Å, Jones24)	PID
(1)	(2)	(3)	(4)	(5)	(6)	(7)	(8)	(9)	(10)	(11)	(12)
JADES-5457	53.11667	-27.81093	4.863	-17.55	< 339		< 4.31	< 2303		1210	
JADES-17159	53.10319	-27.74496	4.857	-19.38	< 536			< 4264			1180
JADES-61321	53.15427	-27.75242	4.842	-18.14	< 601		< 1.04	< 881			1180
JADES-49834	53.20189	-27.78398	4.841	-16.39	< 960		< 10.35	< 544			1180
JADES-10009642	53.19268	-27.78422	4.839	-19.28	< 290		< 0.28	< 2181			1180
JADES-901	189.07141	62.25327	4.833	-19.59	< 786		< 6.75	< 187			1181
JADES-1205	189.11429	62.29300	4.831	-19.37	< 20			< 214			1181
CEERS-83439	214.93807	52.84712	4.824	-18.00	< 17			< 97			1345
JADES-131642	53.16339	-27.77278	4.818	-17.46	< 185			< 1063			3215
JADES-15385	53.13002	-27.75094	4.816	-19.10	< 864			< 3704			1180
CEERS-2000	214.85963	52.88813	4.809	-19.90	< 47			< 16			1345
JADES-10009687	53.13613	-27.80399	4.808	-18.03	< 991		< 6.78	< 3738		< 720	1286
JADES-7938	53.16268	-27.80237	4.806	-19.29	< 412		< 1.42	< 116			1210
CEERS-1565	215.05750	52.99371	4.792	-18.87	< 230			< 281			1345
JADES-10003574	53.16708	-27.76258	4.790	-16.97	999 ± 109	1232 ± 130		194 ± 39			1180
JADES-17110	53.09538	-27.75193	4.789	-20.50	< 945			< 7857			1180
JADES-42355	53.18855	-27.80353	4.789	-18.87	< 603		< 1.80	< 4619			1286
JADES-58656	53.11237	-27.75960	4.786	-18.90	< 279			< 2170		< 358	1180
JADES-41994	53.16483	-27.74984	4.785	-18.98	< 76			< 72			1180
JADES-92212	53.14947	-27.82578	4.782	-17.80	< 23			< 21			1180
JADES-9325	53.15813	-27.79880	4.778	-17.24	< 49			< 191			1180
JADES-58159	53.16742	-27.76204	4.776	-18.63	< 1000			< 451			1180
JADES-9925	53.15813	-27.78643	4.774	-19.81	< 352		< 3.38	< 2122			1180
JADES-9891	53.16719	-27.77461	4.774	-19.34	< 689			< 3889			1180
JADES-132574	53.16732	-27.77182	4.774	-17.98	< 256			< 205			3215
JADES-206035	53.15817	-27.78648	4.773	-20.23	< 111		< 0.17	< 70		< 58	1180
JADES-795	189.19179	62.24205	4.772	-18.50	< 13			< 108			1181
JADES-9377	53.13571	-27.78362	4.771	-18.08	< 80			< 281			1180
JADES-10001892	53.15830	-27.79826	4.771	-16.33	< 48			< 400			1210
JADES-53219	53.15426	-27.77500	4.768	-17.37	< 174			< 1164			1286
JADES-13648	53.17131	-27.75344	4.765	-19.49	< 799			< 628			1180
CEERS-1449	215.08000	52.95679	4.760	-20.95	270 ± 57	34 ± 254		20 ± 3			1345
JADES-9569	53.12739	-27.78524	4.752	-18.75	151 ± 42	16 ± 226		131 ± 29		< 166	1180
JADES-17504	53.09197	-27.71585	4.751	-18.64	< 12			< 23			1180
JADES-17052	53.09256	-27.77245	4.741	-18.47	< 65			< 100			1180
JADES-42299	189.26735	62.16211	4.717	-19.38	< 36			< 4			1181
JADES-15361	53.10373	-27.76326	4.717	-18.24	< 46			< 2303			1180
JADES-72370	189.24414	62.16993	4.716	-18.03	< 13			< 51			1181
JADES-208918	53.17012	-27.77744	4.713	-16.96	< 8			< 114			3215

Table A1 continued

Table A1 (continued)

ID	R.A. (deg)	Decl. (deg)	z_{sys}	M_{UV} (mag)	$F_{\text{Ly}\alpha}$ ($10^{-19} \text{ erg s}^{-1} \text{ cm}^{-2}$)	$\Delta v_{\text{Ly}\alpha}$ (km s^{-1})	$f_{\text{esc}}^{\text{Ly}\alpha}$	EW $_{\text{Ly}\alpha}$ (\AA , This work)	EW $_{\text{Ly}\alpha}$ (\AA , Tang24)	EW $_{\text{Ly}\alpha}$ (\AA , Jones24)	PID
(1)	(2)	(3)	(4)	(5)	(6)	(7)	(8)	(9)	(10)	(11)	(12)
JADES-15345	53.10044	-27.77126	4.710	-18.89	< 30			< 1099			1180
JADES-16402	53.09718	-27.76878	4.709	-18.84	< 35			< 2518			1180
CEERS-82300	214.90056	52.87161	4.707	-18.78	< 26			< 4			1345
JADES-15353	53.09452	-27.76856	4.706	-19.39	< 15			< 150			1180
JADES-17072	53.17022	-27.77739	4.702	-17.80	< 24			< 176			1210
JADES-15325	53.09642	-27.77574	4.697	-19.07	< 24			< 15			1180
JADES-2910	189.09765	62.26758	4.696	-18.50	< 17			< 182			1181
JADES-946	189.08587	62.25904	4.695	-19.60	< 9			< 3			1181
JADES-1110	189.09482	62.27899	4.691	-19.09	< 27			< 29			1181
CEERS-4144	215.17523	53.06328	4.682	-19.60	< 25			< 11			1345
JADES-20621	189.12252	62.29285	4.682	-18.44	199 \pm 52	228 \pm 268		266 \pm 47		< 1401	1181
JADES-35472	53.12490	-27.81929	4.661	-19.03	< 14			< 73			1180
CEERS-2089	214.99918	52.97330	4.653	-18.96	< 48			< 59			1345
JADES-8083	53.13284	-27.80186	4.649	-18.63	20 \pm 8	1225 \pm 395		22 \pm 5	< 286		1210
CEERS-1626	215.07109	52.99032	4.644	-19.84	< 13			< 2658			1345
CEERS-1617	215.07131	52.99229	4.643	-18.73	< 17			< 265			1345
CEERS-3584	214.98875	52.99804	4.642	-19.74	< 26			< 270			1345
CEERS-1217	215.24224	53.03244	4.637	-21.05	< 39			< 480			1345
CEERS-1605	215.07541	52.99758	4.631	-19.48	< 23			< 554			1345
CEERS-1467	215.00293	52.96950	4.631	-18.21	< 61			< 19			1345
JADES-71692	189.28955	62.16546	4.627	-19.23	< 35			< 13			1181
CEERS-1732	215.21281	53.07121	4.621	-20.25	< 57			< 8			1345
JADES-60436	189.20147	62.21276	4.617	-18.35	< 57			< 3			1181
JADES-80391	189.19422	62.21251	4.617	-19.49	< 114			< 485			1181
CEERS-1953	214.99827	52.99474	4.608	-18.38	< 47			< 60			1345
JADES-197429	53.15553	-27.81765	4.601	-16.52	< 17			< 369			3215
CEERS-1534	214.88614	52.87692	4.588	-19.71	< 85			< 52			1345
CEERS-1706	215.11956	53.01010	4.587	-18.50	< 44			< 190			1345
JADES-200679	53.11392	-27.80620	4.561	-20.21	385 \pm 65	1 \pm 5		44 \pm 1	< 39		3215
CEERS-83856	214.80302	52.72654	4.556	-18.71	< 24			< 49			1345
CEERS-83398	214.90041	52.82686	4.554	-18.30	< 45			< 350			1345
CEERS-1767	215.17276	53.03579	4.549	-19.11	< 115			< 24			1345
JADES-35963	53.17338	-27.81832	4.548	-19.58	< 55			< 147			1180
CEERS-1388	215.00011	52.89106	4.548	-19.78	< 106			< 14			1345
JADES-42355	189.28186	62.16226	4.545	-18.55	< 50			< 172			1181
JADES-3154	189.16641	62.23384	4.543		< 57			< 181			1181
JADES-3008	189.12052	62.30317	4.535	-19.60	87 \pm 26	494 \pm 316		40 \pm 5	< 77		1181
JADES-32556	189.10874	62.30203	4.534	-19.75	< 15			< 3			1181
JADES-109798	53.16264	-27.80368	4.524	-18.33	238 \pm 48	2 \pm 6		206 \pm 11	< 341		3215

Table A1 continued

Table A1 (*continued*)

ID	R.A. (deg)	Decl. (deg)	z_{sys}	M_{UV} (mag)	$F_{\text{Ly}\alpha}$ ($10^{-19} \text{ erg s}^{-1} \text{ cm}^{-2}$)	$\Delta v_{\text{Ly}\alpha}$ (km s^{-1})	$f_{\text{esc}}^{\text{Ly}\alpha}$	$\text{EW}_{\text{Ly}\alpha}$ (\AA , This work)	$\text{EW}_{\text{Ly}\alpha}$ (\AA , Tang24)	$\text{EW}_{\text{Ly}\alpha}$ (\AA , Jones24)	PID
(1)	(2)	(3)	(4)	(5)	(6)	(7)	(8)	(9)	(10)	(11)	(12)
JADES-42613	53.18485	-27.80290	4.522	-17.06	< 53			< 247			1180
JADES-42156	53.18133	-27.80400	4.515	-18.31	< 48			< 268			1180
JADES-9932	53.17257	-27.81378	4.512	-19.67	< 11			< 101			1180
JADES-10000861	53.17426	-27.80930	4.510	-16.26	< 100			< 142			1180

NOTE—(1) Galaxy ID. (2) R.A. of the object's coordinate. (3) Decl. of the object's coordinate. (4) Systemic redshift. (5) Absolute UV magnitude. (6) Ly α flux and the 1σ error. For galaxies with no Ly α detections, we show 3σ upper limits. (7) Ly α velocity offset. (8) Ly α escape fraction. (9) Rest-frame Ly α EW measured in this work. EWs of JADES-GS-z14-0, JADES-GS-z14-1, JADES-GS-z13-1-LA measured by Carniani et al. (2024a) and Witstok et al. (2024) are included in this column. (10) Rest-frame Ly α EW measured by Tang et al. (2024a). (11) Rest-frame Ly α EW measured by Jones et al. (2024). (12) JWST program ID.

The values of UV magnitude, Ly α flux, and EW are not corrected for slit loss.

a: Carniani et al. (2024b), b: Carniani et al. (2024a), c: Witstok et al. (2024), d: Harikane et al. (2024a), e: Nakajima et al. (2023)

REFERENCES

- Arrabal Haro, P., Dickinson, M., Finkelstein, S. L., et al. 2023a, *ApJL*, 951, L22, doi: [10.3847/2041-8213/acdd54](https://doi.org/10.3847/2041-8213/acdd54)
- . 2023b, *Nature*, 622, 707, doi: [10.1038/s41586-023-06521-7](https://doi.org/10.1038/s41586-023-06521-7)
- Asthana, S., Haehnelt, M. G., Kulkarni, G., et al. 2024, arXiv e-prints, arXiv:2409.15453, doi: [10.48550/arXiv.2409.15453](https://doi.org/10.48550/arXiv.2409.15453)
- Astropy Collaboration, Robitaille, T. P., Tollerud, E. J., et al. 2013, *A&A*, 558, A33, doi: [10.1051/0004-6361/201322068](https://doi.org/10.1051/0004-6361/201322068)
- Astropy Collaboration, Price-Whelan, A. M., Sipőcz, B. M., et al. 2018, *AJ*, 156, 123, doi: [10.3847/1538-3881/aabc4f](https://doi.org/10.3847/1538-3881/aabc4f)
- Astropy Collaboration, Price-Whelan, A. M., Lim, P. L., et al. 2022, *ApJ*, 935, 167, doi: [10.3847/1538-4357/ac7c74](https://doi.org/10.3847/1538-4357/ac7c74)
- Barkana, R., & Loeb, A. 2001, *PhR*, 349, 125, doi: [10.1016/S0370-1573\(01\)00019-9](https://doi.org/10.1016/S0370-1573(01)00019-9)
- Becker, G. D., D'Aloisio, A., Christenson, H. M., et al. 2021, *MNRAS*, 508, 1853, doi: [10.1093/mnras/stab2696](https://doi.org/10.1093/mnras/stab2696)
- Becker, R. H., Fan, X., White, R. L., et al. 2001, *AJ*, 122, 2850, doi: [10.1086/324231](https://doi.org/10.1086/324231)
- Bolan, P., Lemaux, B. C., Mason, C., et al. 2022, *MNRAS*, 517, 3263, doi: [10.1093/mnras/stac1963](https://doi.org/10.1093/mnras/stac1963)
- Bosman, S. E. I., Davies, F. B., Becker, G. D., et al. 2022, *MNRAS*, 514, 55, doi: [10.1093/mnras/stac1046](https://doi.org/10.1093/mnras/stac1046)
- Bouwens, R. J., Oesch, P. A., Stefanon, M., et al. 2021, *AJ*, 162, 47, doi: [10.3847/1538-3881/abf83e](https://doi.org/10.3847/1538-3881/abf83e)
- Bruton, S., Lin, Y.-H., Scarlata, C., & Hayes, M. J. 2023, *ApJL*, 949, L40, doi: [10.3847/2041-8213/acd5d0](https://doi.org/10.3847/2041-8213/acd5d0)
- Bunker, A. J., Cameron, A. J., Curtis-Lake, E., et al. 2023, arXiv e-prints, arXiv:2306.02467, doi: [10.48550/arXiv.2306.02467](https://doi.org/10.48550/arXiv.2306.02467)
- Carniani, S., Hainline, K., D'Eugenio, F., et al. 2024a, *Nature*, 633, 318, doi: [10.1038/s41586-024-07860-9](https://doi.org/10.1038/s41586-024-07860-9)
- Carniani, S., D'Eugenio, F., Ji, X., et al. 2024b, arXiv e-prints, arXiv:2409.20533, doi: [10.48550/arXiv.2409.20533](https://doi.org/10.48550/arXiv.2409.20533)
- Chisholm, J., Saldana-Lopez, A., Flury, S., et al. 2022, *MNRAS*, 517, 5104, doi: [10.1093/mnras/stac2874](https://doi.org/10.1093/mnras/stac2874)
- Clark, S. J., Dutta, B., Gao, Y., Ma, Y.-Z., & Strigari, L. E. 2018, *PhRvD*, 98, 043006, doi: [10.1103/PhysRevD.98.043006](https://doi.org/10.1103/PhysRevD.98.043006)
- Curtis-Lake, E., Carniani, S., Cameron, A., et al. 2023, *Nature Astronomy*, 7, 622, doi: [10.1038/s41550-023-01918-w](https://doi.org/10.1038/s41550-023-01918-w)
- Das, A., Mesinger, A., Pallottini, A., Ferrara, A., & Wise, J. H. 2017, *MNRAS*, 469, 1166, doi: [10.1093/mnras/stx943](https://doi.org/10.1093/mnras/stx943)
- Davies, F. B., Bosman, S. E. I., & Furlanetto, S. R. 2024a, arXiv e-prints, arXiv:2406.18186, doi: [10.48550/arXiv.2406.18186](https://doi.org/10.48550/arXiv.2406.18186)
- Davies, F. B., Hennawi, J. F., Bañados, E., et al. 2018, *ApJ*, 864, 142, doi: [10.3847/1538-4357/aad6dc](https://doi.org/10.3847/1538-4357/aad6dc)
- Davies, F. B., Bosman, S. E. I., Gaikwad, P., et al. 2024b, *ApJ*, 965, 134, doi: [10.3847/1538-4357/ad1d5d](https://doi.org/10.3847/1538-4357/ad1d5d)
- D'Eugenio, F., Cameron, A. J., Scholtz, J., et al. 2024, arXiv e-prints, arXiv:2404.06531, doi: [10.48550/arXiv.2404.06531](https://doi.org/10.48550/arXiv.2404.06531)
- Dijkstra, M., Mesinger, A., & Wyithe, J. S. B. 2011, *MNRAS*, 414, 2139, doi: [10.1111/j.1365-2966.2011.18530.x](https://doi.org/10.1111/j.1365-2966.2011.18530.x)
- Drake, A. B., Garel, T., Wisotzki, L., et al. 2017, *A&A*, 608, A6, doi: [10.1051/0004-6361/201731431](https://doi.org/10.1051/0004-6361/201731431)
- Eisenstein, D. J., Willott, C., Alberts, S., et al. 2023a, arXiv e-prints, arXiv:2306.02465, doi: [10.48550/arXiv.2306.02465](https://doi.org/10.48550/arXiv.2306.02465)
- Eisenstein, D. J., Johnson, B. D., Robertson, B., et al. 2023b, arXiv e-prints, arXiv:2310.12340, doi: [10.48550/arXiv.2310.12340](https://doi.org/10.48550/arXiv.2310.12340)
- Fakhouri, O., Ma, C.-P., & Boylan-Kolchin, M. 2010, *MNRAS*, 406, 2267, doi: [10.1111/j.1365-2966.2010.16859.x](https://doi.org/10.1111/j.1365-2966.2010.16859.x)
- Fan, X., Strauss, M. A., Becker, R. H., et al. 2006, *AJ*, 132, 117, doi: [10.1086/504836](https://doi.org/10.1086/504836)
- Fausey, H. M., Vejlggaard, S., van der Horst, A. J., et al. 2024, arXiv e-prints, arXiv:2403.13126, doi: [10.48550/arXiv.2403.13126](https://doi.org/10.48550/arXiv.2403.13126)
- Finkelstein, S. L., Bagley, M. B., Ferguson, H. C., et al. 2023, *ApJL*, 946, L13, doi: [10.3847/2041-8213/acade4](https://doi.org/10.3847/2041-8213/acade4)
- Foreman-Mackey, D. 2016, *The Journal of Open Source Software*, 1, 24, doi: [10.21105/joss.00024](https://doi.org/10.21105/joss.00024)
- Foreman-Mackey, D., Hogg, D. W., Lang, D., & Goodman, J. 2013, *PASP*, 125, 306, doi: [10.1086/670067](https://doi.org/10.1086/670067)
- Gaikwad, P., Haehnelt, M. G., Davies, F. B., et al. 2023, *MNRAS*, 525, 4093, doi: [10.1093/mnras/stad2566](https://doi.org/10.1093/mnras/stad2566)
- Garaldi, E., Kannan, R., Smith, A., et al. 2022, *MNRAS*, 512, 4909, doi: [10.1093/mnras/stac257](https://doi.org/10.1093/mnras/stac257)
- Gehrels, N. 1986, *ApJ*, 303, 336, doi: [10.1086/164079](https://doi.org/10.1086/164079)
- Goto, H., Shimasaku, K., Yamanaka, S., et al. 2021, *ApJ*, 923, 229, doi: [10.3847/1538-4357/ac308b](https://doi.org/10.3847/1538-4357/ac308b)
- Greig, B., & Mesinger, A. 2017, *MNRAS*, 472, 2651, doi: [10.1093/mnras/stx2118](https://doi.org/10.1093/mnras/stx2118)
- Greig, B., Mesinger, A., Davies, F. B., et al. 2022, *MNRAS*, 512, 5390, doi: [10.1093/mnras/stac825](https://doi.org/10.1093/mnras/stac825)
- Gunn, J. E., & Peterson, B. A. 1965, *ApJ*, 142, 1633, doi: [10.1086/148444](https://doi.org/10.1086/148444)

- Harikane, Y., Laporte, N., Ellis, R. S., & Matsuoka, Y. 2020, *ApJ*, 902, 117, doi: [10.3847/1538-4357/abb597](https://doi.org/10.3847/1538-4357/abb597)
- Harikane, Y., Nakajima, K., Ouchi, M., et al. 2024a, *ApJ*, 960, 56, doi: [10.3847/1538-4357/ad0b7e](https://doi.org/10.3847/1538-4357/ad0b7e)
- Harikane, Y., Zhang, Y., Nakajima, K., et al. 2023, *ApJ*, 959, 39, doi: [10.3847/1538-4357/ad029e](https://doi.org/10.3847/1538-4357/ad029e)
- Harikane, Y., Inoue, A. K., Ellis, R. S., et al. 2024b, *arXiv e-prints*, arXiv:2406.18352, doi: [10.48550/arXiv.2406.18352](https://doi.org/10.48550/arXiv.2406.18352)
- Harris, C. R., Millman, K. J., van der Walt, S. J., et al. 2020, *Nature*, 585, 357, doi: [10.1038/s41586-020-2649-2](https://doi.org/10.1038/s41586-020-2649-2)
- Hoag, A., Bradač, M., Huang, K., et al. 2019, *ApJ*, 878, 12, doi: [10.3847/1538-4357/ab1de7](https://doi.org/10.3847/1538-4357/ab1de7)
- Hsiao, T. Y.-Y., Abdurro'uf, Coe, D., et al. 2024, *ApJ*, 973, 8, doi: [10.3847/1538-4357/ad5da8](https://doi.org/10.3847/1538-4357/ad5da8)
- Hunter, J. D. 2007, *Computing in Science and Engineering*, 9, 90, doi: [10.1109/MCSE.2007.55](https://doi.org/10.1109/MCSE.2007.55)
- Inoue, A. K., Hasegawa, K., Ishiyama, T., et al. 2018, *PASJ*, 70, 55, doi: [10.1093/pasj/psy048](https://doi.org/10.1093/pasj/psy048)
- Ishigaki, M., Kawamata, R., Ouchi, M., et al. 2018, *ApJ*, 854, 73, doi: [10.3847/1538-4357/aaa544](https://doi.org/10.3847/1538-4357/aaa544)
- Isobe, Y., Ouchi, M., Nakajima, K., et al. 2023, *ApJ*, 956, 139, doi: [10.3847/1538-4357/acf376](https://doi.org/10.3847/1538-4357/acf376)
- Jeon, M., Pawlik, A. H., Bromm, V., & Milosavljević, M. 2014, *MNRAS*, 440, 3778, doi: [10.1093/mnras/stu444](https://doi.org/10.1093/mnras/stu444)
- Jin, X., Yang, J., Fan, X., et al. 2023, *ApJ*, 942, 59, doi: [10.3847/1538-4357/aca678](https://doi.org/10.3847/1538-4357/aca678)
- Jones, G. C., Bunker, A. J., Saxena, A., et al. 2024, *arXiv e-prints*, arXiv:2409.06405, doi: [10.48550/arXiv.2409.06405](https://doi.org/10.48550/arXiv.2409.06405)
- Jung, I., Finkelstein, S. L., Dickinson, M., et al. 2020, *ApJ*, 904, 144, doi: [10.3847/1538-4357/abbd44](https://doi.org/10.3847/1538-4357/abbd44)
- Kannan, R., Garaldi, E., Smith, A., et al. 2022, *MNRAS*, 511, 4005, doi: [10.1093/mnras/stab3710](https://doi.org/10.1093/mnras/stab3710)
- Konno, A., Ouchi, M., Ono, Y., et al. 2014, *ApJ*, 797, 16, doi: [10.1088/0004-637X/797/1/16](https://doi.org/10.1088/0004-637X/797/1/16)
- Konno, A., Ouchi, M., Shibuya, T., et al. 2018, *PASJ*, 70, S16, doi: [10.1093/pasj/psx131](https://doi.org/10.1093/pasj/psx131)
- Kuhlen, M., & Faucher-Giguère, C.-A. 2012, *MNRAS*, 423, 862, doi: [10.1111/j.1365-2966.2012.20924.x](https://doi.org/10.1111/j.1365-2966.2012.20924.x)
- Kulkarni, G., Keating, L. C., Haehnelt, M. G., et al. 2019, *MNRAS*, 485, L24, doi: [10.1093/mnrasl/slz025](https://doi.org/10.1093/mnrasl/slz025)
- Luridiana, V., Morisset, C., & Shaw, R. A. 2015, *A&A*, 573, A42, doi: [10.1051/0004-6361/201323152](https://doi.org/10.1051/0004-6361/201323152)
- Lusso, E., Worseck, G., Hennawi, J. F., et al. 2015, *MNRAS*, 449, 4204, doi: [10.1093/mnras/stv516](https://doi.org/10.1093/mnras/stv516)
- Madau, P., Giallongo, E., Grazian, A., & Haardt, F. 2024, *ApJ*, 971, 75, doi: [10.3847/1538-4357/ad5ce8](https://doi.org/10.3847/1538-4357/ad5ce8)
- Mason, C. A., Trenti, M., & Treu, T. 2015, *ApJ*, 813, 21, doi: [10.1088/0004-637X/813/1/21](https://doi.org/10.1088/0004-637X/813/1/21)
- Mason, C. A., Treu, T., Dijkstra, M., et al. 2018, *ApJ*, 856, 2, doi: [10.3847/1538-4357/aab0a7](https://doi.org/10.3847/1538-4357/aab0a7)
- Mason, C. A., Fontana, A., Treu, T., et al. 2019, *MNRAS*, 485, 3947, doi: [10.1093/mnras/stz632](https://doi.org/10.1093/mnras/stz632)
- Matsuoka, Y., Strauss, M. A., Kashikawa, N., et al. 2018, *ApJ*, 869, 150, doi: [10.3847/1538-4357/aace7a](https://doi.org/10.3847/1538-4357/aace7a)
- Matthee, J., Naidu, R. P., Pezzulli, G., et al. 2022, *MNRAS*, 512, 5960, doi: [10.1093/mnras/stac801](https://doi.org/10.1093/mnras/stac801)
- McGreer, I. D., Mesinger, A., & D'Odorico, V. 2015, *MNRAS*, 447, 499, doi: [10.1093/mnras/stu2449](https://doi.org/10.1093/mnras/stu2449)
- Mesinger, A., Furlanetto, S., & Cen, R. 2011, *MNRAS*, 411, 955, doi: [10.1111/j.1365-2966.2010.17731.x](https://doi.org/10.1111/j.1365-2966.2010.17731.x)
- Mesinger, A., Greig, B., & Sobacchi, E. 2016, *MNRAS*, 459, 2342, doi: [10.1093/mnras/stw831](https://doi.org/10.1093/mnras/stw831)
- Miralda-Escudé, J. 1998, *ApJ*, 501, 15, doi: [10.1086/305799](https://doi.org/10.1086/305799)
- Morales, A. M., Mason, C. A., Bruton, S., et al. 2021, *ApJ*, 919, 120, doi: [10.3847/1538-4357/ac1104](https://doi.org/10.3847/1538-4357/ac1104)
- Morishita, T., Roberts-Borsani, G., Treu, T., et al. 2023, *ApJL*, 947, L24, doi: [10.3847/2041-8213/acb99e](https://doi.org/10.3847/2041-8213/acb99e)
- Murray, S., Greig, B., Mesinger, A., et al. 2020, *The Journal of Open Source Software*, 5, 2582, doi: [10.21105/joss.02582](https://doi.org/10.21105/joss.02582)
- Naidu, R. P., Tacchella, S., Mason, C. A., et al. 2020, *ApJ*, 892, 109, doi: [10.3847/1538-4357/ab7cc9](https://doi.org/10.3847/1538-4357/ab7cc9)
- Naidu, R. P., Matthee, J., Oesch, P. A., et al. 2022, *MNRAS*, 510, 4582, doi: [10.1093/mnras/stab3601](https://doi.org/10.1093/mnras/stab3601)
- Nakajima, K., Ouchi, M., Isobe, Y., et al. 2023, *ApJS*, 269, 33, doi: [10.3847/1538-4365/acd556](https://doi.org/10.3847/1538-4365/acd556)
- Nakane, M., Ouchi, M., Nakajima, K., et al. 2024, *ApJ*, 967, 28, doi: [10.3847/1538-4357/ad38c2](https://doi.org/10.3847/1538-4357/ad38c2)
- Napolitano, L., Pentericci, L., Santini, P., et al. 2024, *A&A*, 688, A106, doi: [10.1051/0004-6361/202449644](https://doi.org/10.1051/0004-6361/202449644)
- Ning, Y., Jiang, L., Zheng, Z.-Y., & Wu, J. 2022, *ApJ*, 926, 230, doi: [10.3847/1538-4357/ac4268](https://doi.org/10.3847/1538-4357/ac4268)
- Oke, J. B., & Gunn, J. E. 1983, *ApJ*, 266, 713, doi: [10.1086/160817](https://doi.org/10.1086/160817)
- Ono, Y., Ouchi, M., Mobasher, B., et al. 2012, *ApJ*, 744, 83, doi: [10.1088/0004-637X/744/2/83](https://doi.org/10.1088/0004-637X/744/2/83)
- Osterbrock, D. E., & Ferland, G. J. 2006, *Astrophysics of gaseous nebulae and active galactic nuclei*
- Ota, K., Iye, M., Kashikawa, N., et al. 2017, *ApJ*, 844, 85, doi: [10.3847/1538-4357/aa7a0a](https://doi.org/10.3847/1538-4357/aa7a0a)
- Ouchi, M., Shimasaku, K., Akiyama, M., et al. 2008, *ApJS*, 176, 301, doi: [10.1086/527673](https://doi.org/10.1086/527673)
- Ouchi, M., Shimasaku, K., Furusawa, H., et al. 2010, *ApJ*, 723, 869, doi: [10.1088/0004-637X/723/1/869](https://doi.org/10.1088/0004-637X/723/1/869)
- Ouchi, M., Harikane, Y., Shibuya, T., et al. 2018, *PASJ*, 70, S13, doi: [10.1093/pasj/psx074](https://doi.org/10.1093/pasj/psx074)

- Pedregosa, F., Varoquaux, G., Gramfort, A., et al. 2011, *Journal of Machine Learning Research*, 12, 2825, doi: [10.48550/arXiv.1201.0490](https://doi.org/10.48550/arXiv.1201.0490)
- Pentericci, L., Vanzella, E., Castellano, M., et al. 2018, *A&A*, 619, A147, doi: [10.1051/0004-6361/201732465](https://doi.org/10.1051/0004-6361/201732465)
- Planck Collaboration, Aghanim, N., Akrami, Y., et al. 2020, *A&A*, 641, A6, doi: [10.1051/0004-6361/201833910](https://doi.org/10.1051/0004-6361/201833910)
- Qin, Y., & Wyithe, J. S. B. 2024, arXiv e-prints, arXiv:2409.07356, doi: [10.48550/arXiv.2409.07356](https://doi.org/10.48550/arXiv.2409.07356)
- Qin, Y., Mesinger, A., Prelogović, D., et al. 2024, arXiv e-prints, arXiv:2412.00799, doi: [10.48550/arXiv.2412.00799](https://doi.org/10.48550/arXiv.2412.00799)
- Ricotti, M. 2002, *MNRAS*, 336, L33, doi: [10.1046/j.1365-8711.2002.05990.x](https://doi.org/10.1046/j.1365-8711.2002.05990.x)
- Ricotti, M., Ostriker, J. P., & Mack, K. J. 2008, *ApJ*, 680, 829, doi: [10.1086/587831](https://doi.org/10.1086/587831)
- Satyavolu, S., Kulkarni, G., Keating, L. C., & Haehnelt, M. G. 2024, *MNRAS*, 533, 676, doi: [10.1093/mnras/stae1717](https://doi.org/10.1093/mnras/stae1717)
- Saxena, A., Cameron, A. J., Katz, H., et al. 2024, arXiv e-prints, arXiv:2411.14532, doi: [10.48550/arXiv.2411.14532](https://doi.org/10.48550/arXiv.2411.14532)
- Schenker, M. A., Stark, D. P., Ellis, R. S., et al. 2012, *ApJ*, 744, 179, doi: [10.1088/0004-637X/744/2/179](https://doi.org/10.1088/0004-637X/744/2/179)
- Scholtz, J., Maiolino, R., D'Eugenio, F., et al. 2023, arXiv e-prints, arXiv:2311.18731, doi: [10.48550/arXiv.2311.18731](https://doi.org/10.48550/arXiv.2311.18731)
- Simmonds, C., Tacchella, S., Hainline, K., et al. 2024, *MNRAS*, 535, 2998, doi: [10.1093/mnras/stae2537](https://doi.org/10.1093/mnras/stae2537)
- Smith, A., Kannan, R., Garaldi, E., et al. 2022, *MNRAS*, 512, 3243, doi: [10.1093/mnras/stac713](https://doi.org/10.1093/mnras/stac713)
- Sobacchi, E., & Mesinger, A. 2015, *MNRAS*, 453, 1843, doi: [10.1093/mnras/stv1751](https://doi.org/10.1093/mnras/stv1751)
- Spina, B., Bosman, S. E. I., Davies, F. B., Gaikwad, P., & Zhu, Y. 2024, *A&A*, 688, L26, doi: [10.1051/0004-6361/202450798](https://doi.org/10.1051/0004-6361/202450798)
- Stark, D. P., Ellis, R. S., & Ouchi, M. 2011, *ApJL*, 728, L2, doi: [10.1088/2041-8205/728/1/L2](https://doi.org/10.1088/2041-8205/728/1/L2)
- Tang, M., Stark, D. P., Topping, M. W., Mason, C., & Ellis, R. S. 2024a, *ApJ*, 975, 208, doi: [10.3847/1538-4357/ad7eb7](https://doi.org/10.3847/1538-4357/ad7eb7)
- Tang, M., Stark, D. P., Ellis, R. S., et al. 2024b, *MNRAS*, 531, 2701, doi: [10.1093/mnras/stae1338](https://doi.org/10.1093/mnras/stae1338)
- Tashiro, H., & Sugiyama, N. 2013, *MNRAS*, 435, 3001, doi: [10.1093/mnras/stt1493](https://doi.org/10.1093/mnras/stt1493)
- Thai, T. T., Tuan-Anh, P., Pello, R., et al. 2023, *A&A*, 678, A139, doi: [10.1051/0004-6361/202346716](https://doi.org/10.1051/0004-6361/202346716)
- Totani, T., Kawai, N., Kosugi, G., et al. 2006, *PASJ*, 58, 485, doi: [10.1093/pasj/58.3.485](https://doi.org/10.1093/pasj/58.3.485)
- Totani, T., Aoki, K., Hattori, T., et al. 2014, *PASJ*, 66, 63, doi: [10.1093/pasj/psu032](https://doi.org/10.1093/pasj/psu032)
- Treu, T., Roberts-Borsani, G., Bradac, M., et al. 2022, *ApJ*, 935, 110, doi: [10.3847/1538-4357/ac8158](https://doi.org/10.3847/1538-4357/ac8158)
- Umeda, H., Ouchi, M., Nakajima, K., et al. 2024a, *ApJ*, 971, 124, doi: [10.3847/1538-4357/ad554e](https://doi.org/10.3847/1538-4357/ad554e)
- Umeda, H., Ouchi, M., Kikuta, S., et al. 2024b, arXiv e-prints, arXiv:2411.15495, doi: [10.48550/arXiv.2411.15495](https://doi.org/10.48550/arXiv.2411.15495)
- Đurovčíková, D., Eilers, A.-C., Chen, H., et al. 2024, *ApJ*, 969, 162, doi: [10.3847/1538-4357/ad4888](https://doi.org/10.3847/1538-4357/ad4888)
- Virtanen, P., Gommers, R., Oliphant, T. E., et al. 2020, *Nature Methods*, 17, 261, doi: [10.1038/s41592-019-0686-2](https://doi.org/10.1038/s41592-019-0686-2)
- Wang, F., Davies, F. B., Yang, J., et al. 2020, *ApJ*, 896, 23, doi: [10.3847/1538-4357/ab8c45](https://doi.org/10.3847/1538-4357/ab8c45)
- Whitler, L. R., Mason, C. A., Ren, K., et al. 2020, *MNRAS*, 495, 3602, doi: [10.1093/mnras/staa1178](https://doi.org/10.1093/mnras/staa1178)
- Witstok, J., Jakobsen, P., Maiolino, R., et al. 2024, arXiv e-prints, arXiv:2408.16608, doi: [10.48550/arXiv.2408.16608](https://doi.org/10.48550/arXiv.2408.16608)
- Yajima, H., Li, Y., Zhu, Q., et al. 2014, *MNRAS*, 440, 776, doi: [10.1093/mnras/stu299](https://doi.org/10.1093/mnras/stu299)
- Yanagisawa, H., Ouchi, M., Nakajima, K., et al. 2024, arXiv e-prints, arXiv:2411.19893, doi: [10.48550/arXiv.2411.19893](https://doi.org/10.48550/arXiv.2411.19893)
- Yang, J., Wang, F., Fan, X., et al. 2020, *ApJL*, 897, L14, doi: [10.3847/2041-8213/ab9c26](https://doi.org/10.3847/2041-8213/ab9c26)
- Zhang, Y., Ouchi, M., Gebhardt, K., et al. 2021, *ApJ*, 922, 167, doi: [10.3847/1538-4357/ac1e97](https://doi.org/10.3847/1538-4357/ac1e97)
- Zheng, Z.-Y., Wang, J., Rhoads, J., et al. 2017, *ApJL*, 842, L22, doi: [10.3847/2041-8213/aa794f](https://doi.org/10.3847/2041-8213/aa794f)
- Zhu, Y., Becker, G. D., Bosman, S. E. I., et al. 2022, *ApJ*, 932, 76, doi: [10.3847/1538-4357/ac6e60](https://doi.org/10.3847/1538-4357/ac6e60)
- Zhu, Y., Becker, G. D., Christenson, H. M., et al. 2023, *ApJ*, 955, 115, doi: [10.3847/1538-4357/aceef4](https://doi.org/10.3847/1538-4357/aceef4)
- Zhu, Y., Becker, G. D., Bosman, S. E. I., et al. 2024, *MNRAS*, 533, L49, doi: [10.1093/mnras/slae061](https://doi.org/10.1093/mnras/slae061)